



Sustainable LiFePO_4 and $\text{LiMn}_x\text{Fe}_{1-x}\text{PO}_4$ ($x=0.1-1$) cathode materials for lithium-ion batteries: A systematic review from mine to chassis

Atiyeh Nekahi, Anil Kumar M.R., Xia, Sixu Deng, Karim Zaghib*

Department of Chemical and Materials Engineering, Concordia University, 1455 De Maisonneuve Blvd. West, Montreal, Quebec H3G 1M8, Canada

ARTICLE INFO

Keywords:

Lithium-ion batteries
Mine-to-chassis
Electric vehicles
Olivine cathode materials
Lithium iron phosphate

ABSTRACT

We conducted a comprehensive literature review of LiFePO_4 (LFP) and $\text{LiMn}_x\text{Fe}_{1-x}\text{PO}_4$ ($x=0.1-1$) (LMFP)-based lithium-ion batteries (LIBs), focusing mostly on electric vehicles (EVs) as a primary application of LIBs. Although numerous individual research studies exist, a unified and coordinated review covering the subject from mine to chassis has not yet been presented. Accordingly, our review encompasses the entire LIB development process. *I*) Initial resources, including lithium, iron, manganese, and phosphorous; their global reserves; mining procedures; and the demand for LIB production. *II*) The main Fe- and Mn-containing precursors, Fe^0 , Fe_xO_y , FePO_4 , FeSO_4 , and MnSO_4 , focusing on their preparation methods, use in LIBs, and their effect on the electrochemical performance of the final active cathode materials. *III*) Use of the precursors in the synthesis of active cathode materials and pioneering synthesis methods for olivine production lines, particularly hydrothermal liquid-state synthesis, molten-state synthesis, and solid-state synthesis. *IV*) Electrode engineering and the design and optimization of electrolytes. *V*) Production of cells, modules, and packs. *VI*) Highlights of the challenges associated with the widespread utilization of olivines in LIBs, emphasizing their safety, cost, energy efficiency, and carbon emissions. In conclusion, our review offers a comprehensive overview of the entire process involved in the fabrication of LFP/LMFP-based LIBs, from the initial elements in the mine to the assembly of the final packs that power EVs.

1. Introduction

Lithium-ion batteries (LIBs) have become enormously attractive in recent years due to the significant growth of the electric vehicle (EV) market. The International Energy Agency (IEA) predicted a global battery market valued at \$360–410 billion in the next decade, with the global electric car market growing to 35% of total car sales by 2030 [1]. The USA market is set to exceed this with a 50% electrification target, while Canada aims to have at least 60% EVs by 2030 and 100% by 2035 [2]. The US Department of Energy (DOE) anticipates a growth factor of 5–10 for the global lithium battery market in the next decade [3]. One of the reasons for such a sharp trend in vehicle electrification is the pledges that many nations took during the Paris Agreement [4] to reduce emissions to 45% by 2030 and aim for net zero emissions by 2050. Accordingly, 30% lower emissions are anticipated for the transportation sector by 2030, with the goal of 100% reduction by 2040 [1].

Batteries are a core technology for realizing energy transitions and broadening energy access worldwide. Asia is an undisputed leader in the battery industry, e.g., China hosts 80% of the cell manufacturing

capacity and material refining worldwide. The US, Japan, and South Korea play important roles in EV battery manufacturing: The European Union invested €127 billion in the battery industry in 2021 and is expected to invest €382 billion more by 2030 to fulfill a plan of building 38 battery plants that will produce batteries for 11 million EVs annually. The USA announced 10 battery plants in 2021, attracted \$20 billion in battery assets, and produced 14000 jobs [1]. The White House also reported funding above \$9 billion to leverage EV battery production. According to this report, the EV industry is divided into various critical phases based on the battery supply chain (Fig. 1). These phases begin with the first steps in EV production: supplying battery-grade elements such as Li, G, and Ni, setting up the first LiFePO_4 (LFP) cathode facility, installing a lithium hexafluorophosphate (LiPF_6) electrolyte production facility, and developing a binder facility [5]. McKinsey proposed almost the same model for LIB's supply chain, which can provide over \$400 billion revenue by 2030 [6]. Canada also built its first gigafactory in 2021, investing over \$5 billion and generating 3200 jobs. Another \$2 billion is being considered for cathode manufacturing [1].

The olivine structures of LiXPO_4 (X is Fe, Mn, Co, or Ni) have shown

* Corresponding author.

E-mail address: karim.zaghib@concordia.ca (K. Zaghib).

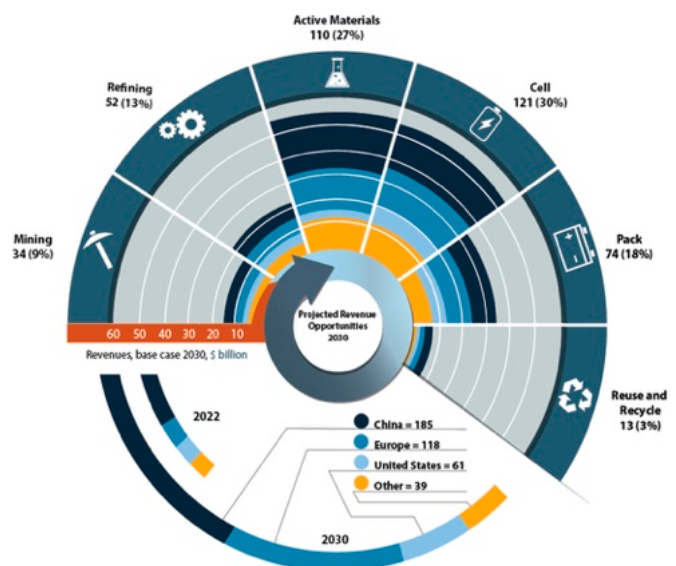


Fig. 1. Representative elements in the LIB supply and value chains taken from the literature [5,6] that were used as the focus for this review paper.

remarkable growth in the battery industry, while oxide materials such as LiCoO_2 were the first commercialized cathode materials in LIBs. These materials have attracted widespread interest after the introduction of phospho-olivines by J.B. Goodenough as a candidate for “positive-electrode materials” in rechargeable lithium batteries [7]. LFP has attracted the most attention among the olivine structures and has been commercialized, thereby promoting the advantages of LIBs and their dominance in the market, especially for EV applications. Despite having a lower energy density of 160 Wh/kg compared to lithium nickel manganese cobalt oxide (LiNiMnCoO_2 , NMC) or lithium nickel cobalt aluminum oxide (NCA) at 210–220 Wh/kg [8], LFP benefits from a lower average cost compared to that of NMC and NCA and lower risk of thermal runaway. In addition, it minimizes the use of unsustainable initial materials, and exhibits a long discharge life of 2500 cycles versus 1000 cycles for conventional cathodes [9,10]. The stability and safety arise from strong P–O bonds, which prevent explosions. Such excellent bonding strength makes LFP durable and prevents dissolution (1300 cycles at 100% depth of discharge) [11]. Moreover, LFP does not suffer from overheating or outgassing issues, eliminating the need for a battery-monitoring system [12–14]. Similarly, a cooling system for the pack is not required, which significantly reduces the system’s complexity and cost [15]. As a result, LFP has been thoroughly studied, and practical applications have already commenced. An excellent

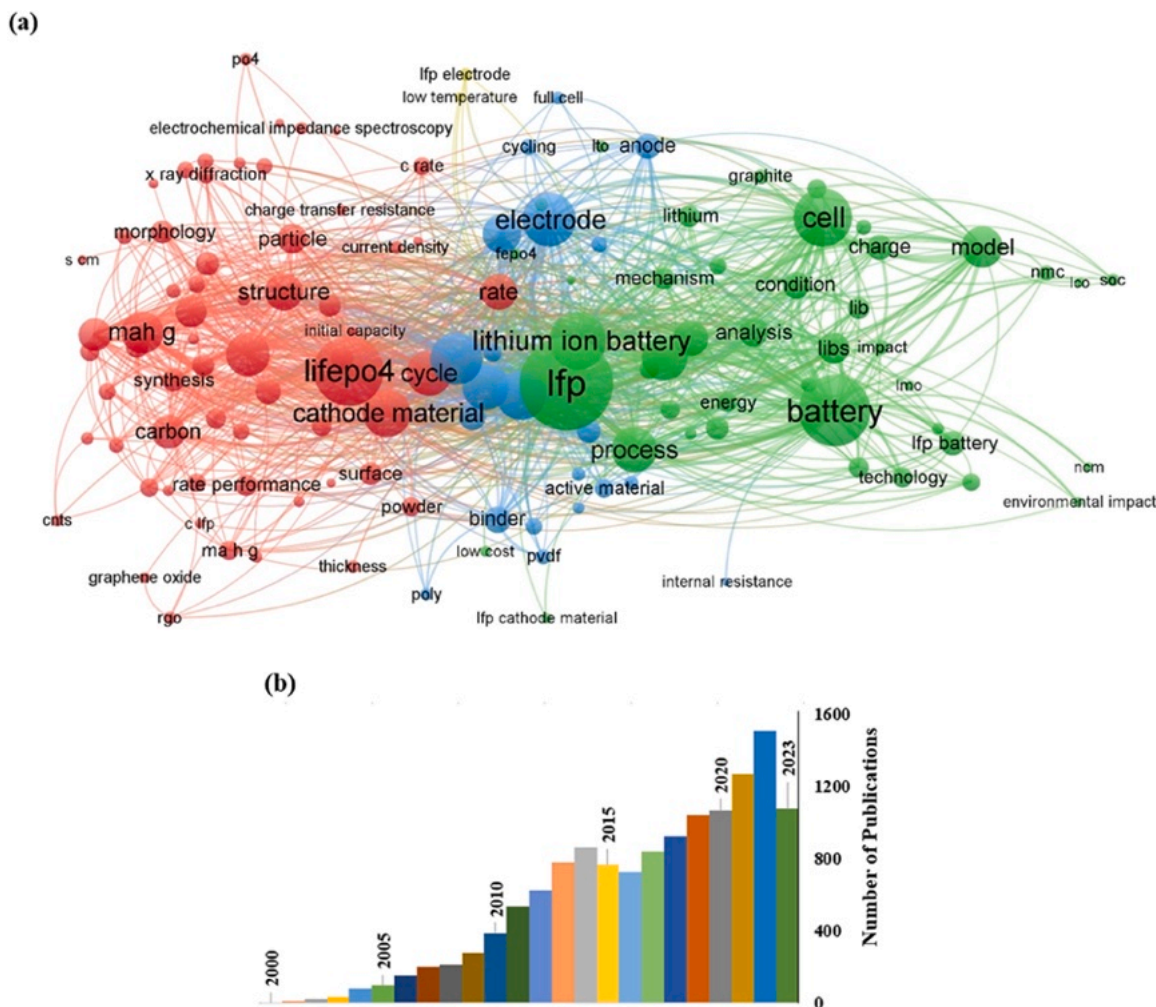


Fig. 2. (a) Importance of each subject in the LFP domain identified by analyzing the first 1000 papers (sorted by relevance) from 13500 articles indexed by the Web of Science [16] retrieved using the search term “LFP lithium-ion battery” and adding “ LiFePO_4 ” and “Lithium Iron Phosphate” as The circle sizes correspond to the frequency of the in the articles. The largest circles with 1346, 892, and 855 occurrences are for LFP, battery, and LiFePO_4 , respectively. The smallest circle indicates 33 occurrences. Some general were excluded. (b) The significant increase in the volume of publications pertaining to the LFP LIBs over the past 20 years (retrieved from Web of Science [16]) indicates the growing popularity of LFP chemistry as a research topic.

description of essential subjects in the LFP domain was presented in a previous study based on analyzing 13500 articles indexed by the Web of Science [16], as shown in Fig. 2.

The working voltage is one of the most essential factors in determining the energy density of a battery. In addition to commercial LFP with a working voltage of 3.2 V, alternative olivine structures, such as those based on Mn, Ni, and Co, have not yet been commercialized as cathodes because it is currently not possible to produce batteries that operate at their high redox potentials (vs. Li^+/Li): 4.1 V for lithium manganese phosphate (LiMnPO_4 ; LMP), 5.2 V for lithium nickel phosphate (LiNiPO_4 ; LNP), 4.8 V for lithium cobalt phosphate (LiCoPO_4 ; LCP), 4.8 V for LiCoFePO_4 (LCFP), and 4.1 V for LiCoMnFePO_4 (LCMFP) [17]. In addition, Co is expensive because of its environmental toxicity and scarcity and has poor stability owing to irreversible dissolution in the electrolyte [13,18]. LMP, LNP, and LCP have even higher electrical resistances than LFP; however, this drawback was overcome in the same way as for LFP by reducing the particle size and preparing composites with carbon. However, a comparable capacitance can only be obtained by 20–30% carbon addition, which exceeds the limits for practical EV applications. This is due to the low catalytic effect of Mn on C and its tendency to calcinate above 650 °C [12]. Nevertheless, research centers and automakers are attempting to utilize olivine structures based on Mn or Fe-doped Mn [19,20].

In conclusion, this review describes the mine-to-chassis process, mainly focusing on LFP-based materials owing to their successful transition from the laboratory to the market. We also review the literature on LMFP, the most promising olivine cathode materials for next-generation high-energy batteries. Apart from a broad introduction, other battery chemistries, such as alkali metal batteries [21–27], have not been covered because their industrialization and potential applications in EVs seem improbable at this moment. Conventional oxide cathode chemistries such as NMC, NCA, and lithium cobalt oxide (LiCoO_2 , LCO) are only mentioned for comparison. The main objective of this review was to describe the entire story of battery production, starting from the mine and ending at the chassis of an EV, to address the lack of a comprehensive paper including all of these details. Knowledge of the entire process and specific details regarding the resources, processes, markets, and challenges is expected to help researchers identify gaps in the field and focus work on the most critical parts of the process. Furthermore, researching LFP and LMFP materials would be much more valuable with a detailed knowledge of the mine-to-chassis process.

2. Mining of initial resources

2.1. Lithium

Battery applications use 70% of the mined Li and are the primary technology driving the demand for Li extraction. South America (mostly Chile with more than 9 million tons (Mt) and Argentina with approximately 2 Mt) is recognized as having the most abundant Li reserves (brine-based). Furthermore, Australia (with 4.5 Mt reserves) ranks first in Li production (0.04 Mt/year; primarily hard rock lithium) because the mature processing technique for hard rock (spodumene) follows a conventional mining process based on a manageable mine plan, stockpiles, consistent feed, and refining processes [28]. Approximately 62% of the global Li occurs in brines, while the remaining 38% is present in rock minerals [29]. Canada ranks sixth in terms of Li reserves, including both brine (western provinces) and spodumene (Québec and Ontario). These deposits are valuable, and their proximity to EV manufacturers helps localize the supply chain and avoid lengthy travel distances for heavy batteries [1]. The global resources and mine production of Li in different countries are presented in Fig. 3. Annual mine production is expected to increase 2.5–5 times by 2030 [30–32]. Fig. 3a shows the reported global lithium resources in 2021. Bolivia has the most enormous lithium resources, at 21 Mt, followed by Argentina and Chile, at 19 Mt and 9.8 Mt, respectively. Although Australia ranked fifth in resources (7.3 Mt), it

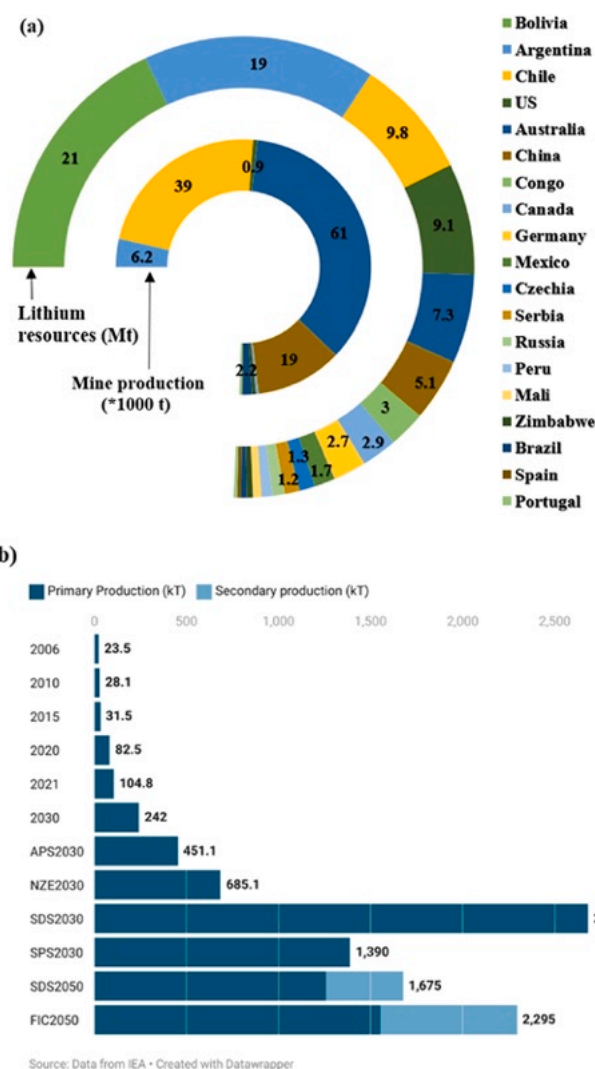


Fig. 3. (a) Global lithium resources reported in 2021 and mine production in 2021 or 2022 [28,33]. Only the highest values are shown for comparison. (b) Global annual lithium production (Kt) from 2006 to 2021 and predicted production in 2030 and 2050 based on different scenarios; APS: Announced Pledges Scenario, NZE: Net Zero Emissions, SDS: Sustainable Development Scenario, SPS: Stated Policies Scenario, FIC: Foster Innovation Case. Data is presented interactively in Datawrapper. Data was drawn from IEA [30–32].

holds the first position in Li production (61000 t) thanks to the mature processing technique for hard rock (spodumene). Chile, with 39000 t, placed second, and China took third place with 19000 t, while it only has a 5.1 Mt resource [28,33].

Fig. 3b illustrates the global annual lithium production from 2006 to 2021, showing a four times increment from 23.5 to 104.8 Kt. The forecasted production in 2030 and 2050 is also shown in this figure. Notably, the projected production in 2030 ranges from about 240–2700 Kt, a broad and versatile estimation based on different scenarios in the IEA report. In 2050, one-fourth and one-third of the production is forecasted to be of the secondary production ways of recycling [30–32].

Hard rock extraction includes comminution, high-temperature calcination, roasting, leaching, neutralization, and impurity removal. The estimated cost of this extraction method is almost twice that of brine extraction. Lithium extraction from brine involves many stages, including precipitation, ion exchange, solvent extraction, electro dialysis, and separation [28]. However, the evaporitic technology of brine mining has been questioned for its intensive water demand and long duration; it can take up to one year to obtain a large amount of final salt

waste [29]. The environmental impact and techno-economic shortcomings of current direct brine lithium extraction practices must be addressed. The main brine extraction technologies were categorized into seven groups (Fig. 4). Technological advancements have achieved Li recovery of up to 95%, significant Mg^{2+} separation, and zero waste routes [34].

High-affinity materials for Li^+ cations are shown in Fig. 4a. Even at much lower concentrations than coexisting cations, Li^+ cations are adsorbed onto tiny resin particles from brines. Li^+ cations from the resins typically use freshwater or acidic solutions, yielding a relatively pure Li^+ solution (usually $LiCl$) (Fig. 4b). A significant amount of Li^+ cations are moved from the brine into the organic or ionic liquid phase when these solvents come into contact. To release the Li^+ cations, the Li^+ loaded phase is subsequently combined with an aqueous phase. As an alternative, electrical fields (Fig. 4c) or mechanical forces (Fig. 4d) can power membrane processes for selective lithium recovery. However, Li^+ is added to an electrode material exposed to a potential gradient in electrochemical ion pumping and goes through an electrochemical reaction (Fig. 4e, left). No species are simultaneously released into the brine, and no chemicals are required. Afterward, Li^+ is extracted from the electrode material with recovery solutions that need replenishment with fresh water (Fig. 4e, right). The basis for selective precipitation (Fig. 4f) is lithium phosphate's extremely low aqueous solubility (Li_3PO_4). The goal of open-air evaporation ponds is also brine

concentration; the only difference is that water evaporates and is lost to the atmosphere in this scenario. Membrane distillation and solar evaporators are two examples of these procedures (Fig. 4g), examining the chemistry of various materials (solvents, insertion electrodes, membranes, and adsorptive materials). One of the most essential processing steps is the concentration or capture of Li^+ ions. However, for direct lithium extraction to be successful, native brine pre-processing is frequently required. Moreover, the majority of direct extraction technologies that have been suggested result in purified solutions that need to be post-processed rather than pure lithium products (Fig. 4h) [34].

Despite the economically viable reserves of Li as brine and spodumene, which account for 80% of Li production worldwide, other low-concentration, uneconomical Li-bearing minerals could become viable as the Li price increases. Furthermore, the unequal geographical distribution of Li resources makes exploiting Li-bearing clays attractive. These resources could also help provide a secure Li supply, thereby becoming key influential factors in the sustainable development of the lithium industry. Li-bearing clays are widespread in Asia and the Americas [35, 36].

In addition to land-based deposits, a massive Li reserve, which contains Li originating from beneath the rocks, has been found in the deep geothermal waters of California's Salton Sea. Geothermal Li brine has a low Li content (a few hundred parts per million (ppm)), but this content is sufficient to attract interest [37]. The Department of Energy (DOE)

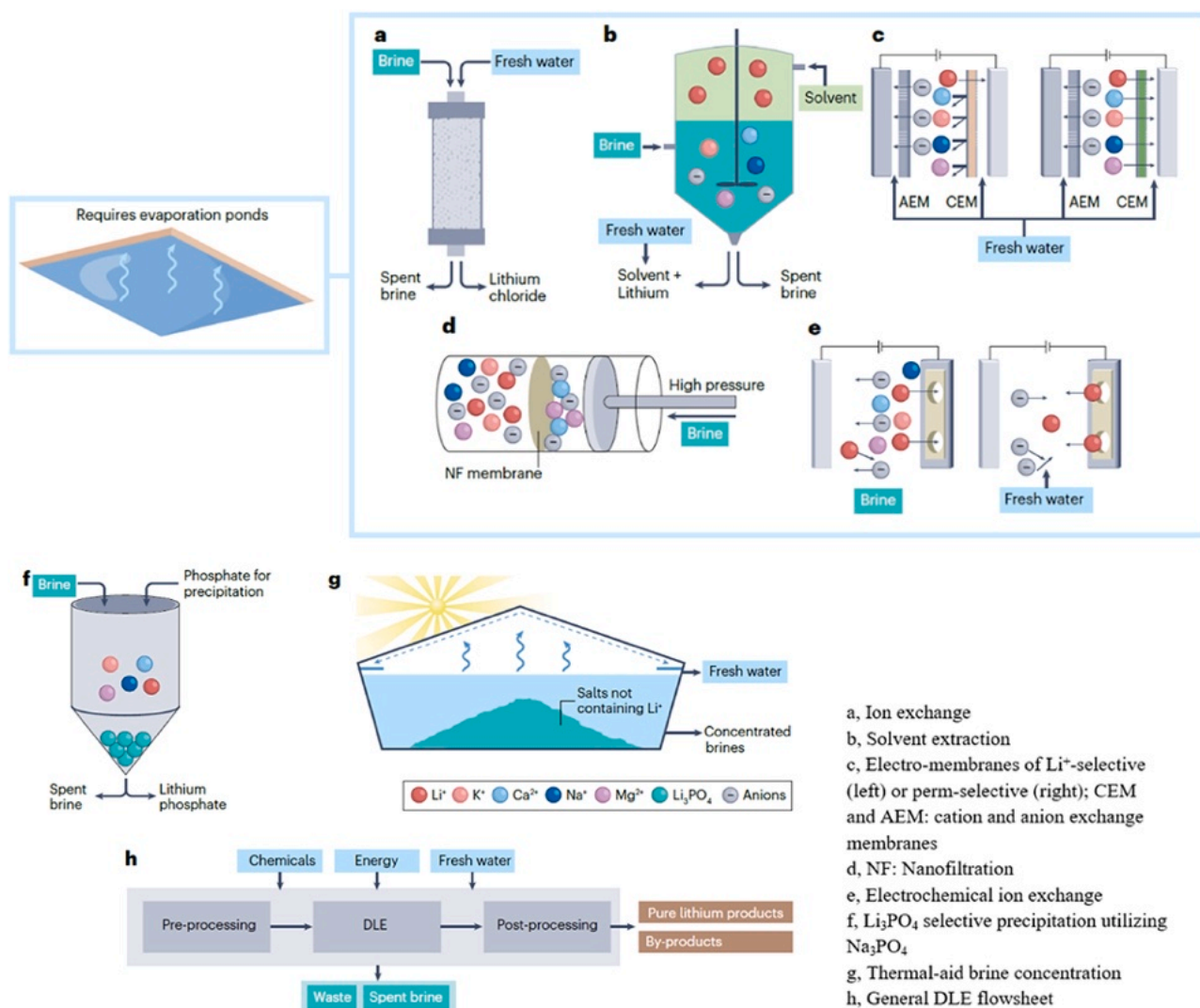


Fig. 4. Graphical summary of direct lithium extraction from brine. Reproduced with permission from [34].

expects this subsurface reserve to fulfill the domestic demand for rechargeable batteries in the USA by providing approximately 0.6 Mt/year of lithium [38]. To ensure that geothermal brine becomes a reliable reservoir of Li, the high corrosiveness of the hot brine must be managed, along with the toxicity of the accompanying arsenic and lead [39].

Unlike traditional land-based Li deposits, which are located in only a few geographic regions, seawater is recognized as a vast, evenly distributed resource containing 230 Gt of Li. However, the low Li concentration below one ppm hinders its widespread use [40]. The invention of cost-competitive practical seawater extraction technologies could result in massive global harvesting of seawater Li [41,42]. Despite the high Na concentration in seawater that complicates Li extraction, specific techniques, such as pulsed electrochemical intercalation, can reduce the intercalation overpotential while successfully boosting Li selectivity [43]. Solar-powered electrolysis using NASICON selective membranes was proposed as a faster and more controllable method for Li extraction than adsorption or dialysis [44].

LiOH and Li₂CO₃ were employed as raw materials to synthesize active cathode materials (ACMs) (Table 1) [28,45]. A single EV battery (NMC532) contains 8 kg of Li₂CO₃, 35 kg of nickel, 14 kg of cobalt, and

20 kg of manganese [46]. In the case of LFP-based EV batteries, each pack of 60 kWh requires 5.7 kg of Li, 41 kg of Fe, and 25.5 kg of P [47, 48]. Regardless of the resource type and production method, Li₂CO₃ (up to 99.9% purity in a battery grade) remains a crucial product of LiOH, thanks to market demands in the battery sector. The market standard reports are based on Li₂CO₃ equivalents. There is a growing trend towards the direct conversion of brine resources owing to the increasing demand for battery cathodes. This results from a considerable increase in operational costs, which are more than doubled by using LiOH (\$3.04/kg) instead of Li₂CO₃ (\$1.26/kg).

Based on a typical scenario, the projected LFP-based EV demand, with its 60% market share, will require 0.72 Mt of Li annually by 2050 [47]. More broadly, the cumulative Li demand is estimated between 6 and 25 Mt based on different scenarios, depending on the EV adoption rate, battery size, and amount of Li per battery. With the development of solid-state batteries, the demand for metallic Li is expected to increase. LiPF₆ electrolytes have also increased the demand by more than 12% [28,45]. Overall, DOE estimations reveal that Li demand will increase by 500% by 2050 because of the widespread adoption of high-tech systems, with LIBs playing the most crucial role [52]. Fig. 5a shows the predicted demand for LIBs in 2030 based on chemistry, sector, and region and the

Table 1

L CA results for the production of the metals or compounds required for LMFP production (data are based on one metric ton (t) of product). CO_{2eq} refers to CO₂ equivalent. PVDF: polyvinylidene fluoride; NR: not reported; LDH: lithium-aluminum-layered double hydroxide chloride; EMM: electrolytic manganese.

Ref.	Source of metal	Product	Chemicals (T)	Technology	Water (T)	Energy (kWh)	Global warming (T CO _{2eq})	Acidification (kg SO ₂ eq)	Solid waste (T)
[34]	Lithium brine, Salar de Atacama/Salar de Olaroz	Li ₂ CO ₃	NR	Evaporative technology	22.5	NR	NR	NR	115
	Lithium brine, Salar del Hombre Muerto	Li ₂ CO ₃	NR	DLE technology	50	50% Solar+50% natural gas	0.403	NR	NR
[49]	Spodumene ore (0.8–0.9% conc.), western Australia	Concentrated spodumene (6% Li ₂ O)	–	NR	3.4	1250 diesel	~0.42	NR	NR
	Concentrated spodumene (the above line) shipped to China	LiOH·H ₂ O	H ₂ SO ₄ (1.52), Na ₂ CO ₃ (0.025), NaOH (1.18), CaCO ₃ (0.6)	NR	69	3500 China grid 19817 coal	15.7	NR	NR
		Li ₂ CO ₃	H ₂ SO ₄ (1.71), Na ₂ CO ₃ (2.05), NaOH (0.05), CaCO ₃ (0.7)	NR	77	1800 China grid 37747 coal	20.4	NR	NR
	Lithium brine, Salar de Atacama (~0.17% Li)	Concentrated lithium	NR	NR	2.95–7.30	620 Electricity 1600 diesel	0.08–0.18 g	NR	NR
	Concentrated lithium (from the above line)	LiOH·H ₂ O	CaO (1.15)	Evaporative technology	31–50	1400 Electricity 833 Diesel 5830 Natural gas	6.9–7.3	NR	NR
		Li ₂ CO ₃	Na ₂ CO ₃ (2), H ₂ SO ₄ , HCl, lime, solvent, alcohol	Aggregate production process	15.5–32.8	416 Electricity 111 Diesel 778 Natural gas	2.7–3.1	NR	NR
[45]	GLB, LiCl with 194 ppm Li, Salton Sea, Southern California	Li ₂ CO ₃	Na ₂ CO ₃ (2.05) PVDF, NaCl, Sorbent	LDH sorbent and forward osmosis	NR	349–75% fossil+25% biomass & renewable	1.21258	0.00648	
	Li ₂ CO ₃ (above line)	LiOH	Ca(OH) ₂ (1.63), PVDF, NaCl, Sorbent		8.14	1985 ~50% fossil+ ~50% renewable	3.36397	0.01279	NR
[50]	MnCO ₃ ore (29.83% Mn) Ningxia Province, China	EMM (42.43% Mn)	SeO ₂ (0.011), H ₂ SO ₄ (0.81), NH ₃ (0.05)	The US Bureau of Mines	Fresh (4.24) Tap (0.25)	7385 Coal (0.5 t)-based electricity	9.59	18.9	4.31
	MnCO ₃ ore (44% Mn) South Africa	EMM (99.9% Mn)	H ₂ SO ₄ (0.25)	Selenium-free sulfur dioxide technology		2100 Hydroelectricity	2.61	17.9	1.67
[51]	MnCO ₃ ore (44% Mn) South Africa	EMM (99.9% Mn)	H ₂ SO ₄ (0.08), NH ₃ (2.1)	Selenium dioxide technology	2.2	63	NR	80	1.67
	MnCO ₃ ore (16%) China	EMM (99.7% Mn)	H ₂ SO ₄ (0.06), SeO ₂ (0.026)	The US Bureau of Mines, Sulfur Dioxide Technology)	0.18	21	NR	60	7.68

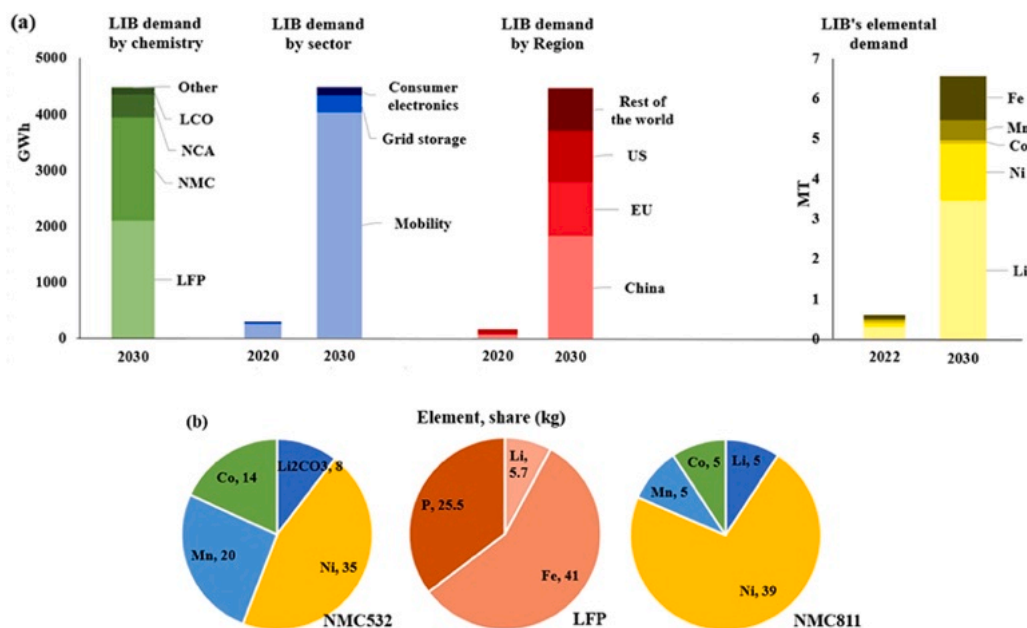


Fig. 5. (a) LIB demand by chemistry, sector, and region. Data was drawn from [53,54,57]. (b) Corresponding demand for individual elements. Data was drawn from [46,48].

demand breakdown based on strategic elements. Considering chemistry, LFP took almost half the demand, followed by NMC and LCA [53]. This figure shows the significance of considering LFP and NMC chemistries in future demand and taking proper measurements to deal with the challenge of providing enough resources. Considering the demand by analyzing the sector revealed that mobility, specifically EVs, took up the highest share of almost 90%, while grid storage and consumer electronics took the remaining share. This significant demand for the mobility sector is absolutely attributed to the enormous growth of EVs and the demand for electrified transportation. The overall sector demand surged approximately fifteenfold from 2020 to 2030 [47,53]. In 2030, it is projected that China will contribute 40% of the worldwide demand for LIBs, showcasing a significant increase from nearly 70 GWh in 2020 to surpassing 1800 GWh in 2030, which contains 40% of the global demand [53,54]. LIB's elemental demand has also enhanced sharply, from 0.6 Mt for the main LIB elements of Li, Ni, Co, Mn, and Fe in 2022–6.6 Mt in 2030. More than half of this portion comes from the need for Li [54]. The elemental demand relies on the proportion of each chemistry within the total demand for LIBs (Fig. 5a) and the distribution of each element within these chemistries. This elemental share (kg) in a single LIB pack made of NMC532, LFP, and NMC811 is shown in Fig. 5b [46,48,55]. However, the precise demand cannot be predicted because various scenarios for the growth of ACM affect the forecasts [56]. A life-cycle assessment (LCA) of the production of 1 metric ton of Li is provided in Table 1. We highlighted the Li and Mn products, which are critical for LMFP production.

2.2. Manganese

Among the 15 countries mining Mn, South Africa has 70% of the global Mn reserves and has long produced high-quality Mn from mines in the Kalahari Basin, Northern Cape [58]. Over 90% of the global high-purity Mn (electrolytic Mn metal; EMM) is produced in China. The only other producer of high-grade EMM (99.9%) is South Africa's "Manganese Metal Company", which has the world's largest Mn refinery and produces EMM using a selenium-free technique. EMM (>97% Mn), electrolytic manganese dioxide (EMD; 63% Mn), and manganese sulfate monohydrate (MSM; 32% Mn) are among the most important products. These products comprise <1% of the annual mined Mn (20 Mt) [58].

High-purity MSM (HPMSM) has been exclusively used in LIBs, and high-purity EMM (HPEMM) has found new applications in this industry. The demand for Mn is projected to increase to meet the planned annual distribution of 150 million EVs by 2030. It was predicted that we will see a surge in Mn production of over 900%, from 0.085 Mt in 2020–0.815 Mt in 2030, based on the Net Zero scenario [59]. The proportions of Mn in various NMC cathodes and the expected demand in 2030 are shown in Fig. 5. A looming shortage has been overlooked for high-purity Mn despite the abundance and availability of standard Mn ore owing to its insufficient processing capacity [60].

Almost all industrially refined Mn is produced via similar sequential steps, as shown in Fig. 6. First, the ore is mined, crushed, and ground. The ground ore is then processed by magnetic separation to increase its grade. Subsequently, the treated ore is leached with H_2SO_4 , followed by an additional step to remove other elemental impurities, such as iron and heavy metals. Leaching is the most common method of purifying manganese sulfate from manganese ores. High-purity manganese sulfate monohydrate was obtained from low-grade manganese ore (Mn_3O_4) by several sequential leaching and reduction steps using sulfuric acid, calcium hydroxide, sulfides, and sodium hydroxide to eliminate undesired components [61]. Such time-consuming, multistep reduction of manganese oxide ores has been widely patented. In another method, manganese dioxide (MnO_2) was reduced with sulfides, sulfuric acid, and hydrogen peroxide [62]. Subsequently, the reduced material was heated, filtered, crystallized, and dewatered to obtain manganese sulfate. Heavy metals, such as insoluble sulfides, were separated from the dissoluble manganese compounds in acid. It was reported that H_2SO_4 exhibits better selectivity for Ca than HCl despite having similar leaching efficiencies [63]. When manganese carbonate is used as the starting ore, MnO_2 serves as an oxidant for ferrous ions. Simultaneously, sodium dimethyl dithiocarbamate effectively precipitates heavy metals, providing superior selectivity toward Ni^{2+} , which is precipitated in the form of a chelate. It was noted that optimizing the influential factors is important to obtain $MnSO_4 \cdot H_2O$ with 98% purity. Analysis of the leaching kinetics revealed diffusion-controlled leaching based on fitting the data with a shrinking core model. Hence, increasing the lixiviant concentration or reducing the solid particle size to accelerate diffusion can enhance Mn extraction.

In the final refining step, the material is upgraded to its desired

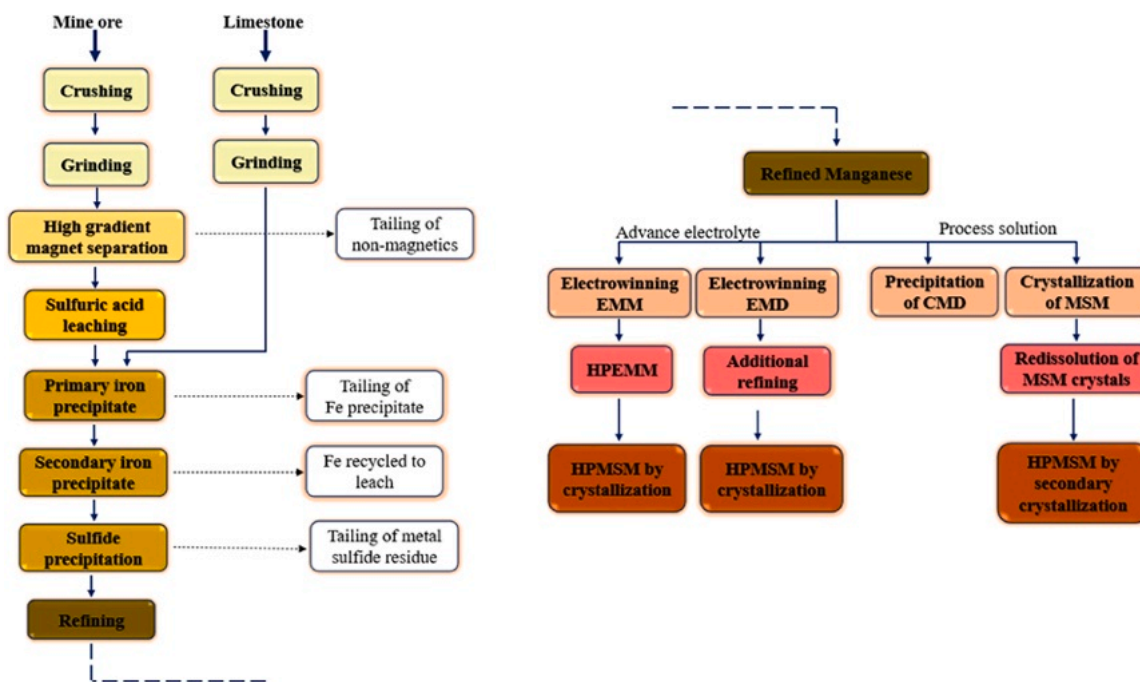


Fig. 6. Various steps in purifying and refining manganese to reach HPMSM product. Reproduced with permission from [64].

purity. The type of ore determines the associated costs based on the purification steps and their requirements, such as the H_2SO_4 content and energy and water usage. Also, it affects the final waste content [64]. The final refining step for EMM production consumes a large amount of power and resources while discharging substantial waste [65]. The LCA results of the electrolytic Mn production line are presented in Table 1. Zhang et al. reported a production approach in China that uses hydro-electricity to reduce coal-based electricity consumption [50]. However, a production line located in South Africa is considered optimal based on its lowest solid-waste generation of 1.67 t, H_2SO_4 consumption of 0.25 t, and minimal electricity consumption of 2100 kWh, resulting in 18.9 kg $\text{SO}_{2\text{eq}}$ acidification and 2.61 t $\text{CO}_{2\text{eq}}$ global warming. These data assume the production of 1 t of EMM. The South African process is far more efficient than those reported in China, with significantly higher amounts of solid waste (4.31 t), H_2SO_4 consumption (0.81 t), electricity usage (6800 kWh), greenhouse gas (GHG) emissions (7.85 t $\text{CO}_{2\text{eq}}$), and acidification level (17.9 kg $\text{SO}_{2\text{eq}}$). The residue of the Mn electrolyte can be further processed to recover the remaining valuable Mn. Recovery was achieved by precipitating soluble manganese from the electrolyte manganese residue with CO_2 -bubbled ammonia. The optimal recovery of 94.2% for MnCO_3 and Mn_3O_4 was achieved with an ammonia-to-manganese molar ratio of 3:1 and 2 L/min CO_2 bubbling rate for 2 min [66].

2.3. Iron

Iron ranks second among the most significant commodities, following oil. Iron ore, essential for crude steel production, feeds the largest trillion-dollar-a-year global metal market and is considered a global infrastructural backbone [67]. Furthermore, 98% of iron ore goes into steel making, and 2% is used in other applications, with a negligible share in LIBs [68].

Australia has the largest reservoir of crude iron ore, i.e., in 2022, 51 Gt of ore including 27 Gt of iron was reported, and half of the global iron ore was mined. Brazil ranks second, with 15 Gt of iron reserves from 34 Gt of crude ore. Brazil's production accounts for ~20% of the total exports, i.e., 410 Mt produced iron ore in 2022. The world's largest iron mine in Brazil, Vale's Carajas mine, contains almost 7.2 Gt of iron ore and produces approximately 0.3 Mt/day of iron ore material [69].

More than 99% of the Earth's Fe is found in three minerals: magnetite (Fe_3O_4), hematite (Fe_2O_3), and goethite ($\text{Fe}_2\text{O}_3 \cdot \text{H}_2\text{O}$) [70,71]. Iron-ore reserves are mainly located in the first few meters underground, so open-pit mining is used. Owing to the enormous amount of available resources, deep mining is rare but is performed in northern Sweden using automatic and remote-controlled machinery [72].

High-grade ores are processed by metallurgical lines, whereas low-grade ores are directed toward beneficiation processes, such as gravitational, magnetic, or flotation procedures, or a combination of these depending on the composition of the minerals. Providing high-quality concentrates (high Fe percentage and low impurities) from low-grade ores depends significantly on the liberation and separation potential of the mineral [73]. The ore is processed using several steps. First, the ore is crushed in stages, mainly using jaw crushers, gyratory or cone crushers, and screening stages with vibrating screens, static screens, and roller screens (grizzlies). The conventional sequential steps for magnetite deposition include three- or four-stage crushing, wet semi-autogenous milling, autogenous milling, and ball milling. Magnetic separators play a vital role in upgrading the grade of iron ore. The classification stage uses hydrocyclone separators or air classifiers. Various operational flowsheets have been provided in the literature [74,75]. However, depending on ore characteristics and impurities, beneficiation may require additional facilities and complicated technologies based on physicochemical [76] or chemical [77] routes to remove phosphorus, silica, aluminum oxide, and silicate. The concentrates are agglomerated via sintering [78] or pelletization [79]. These agglomerates (65.5–68% Fe content) are suitable for use in blast furnaces (accounting for almost 70% of annual global steel production) and direct reduction [78]. The final product contains 90–95% Fe [80].

Two difficult challenges in the overall mining and ironmaking process are reducing energy consumption and carbon emissions. The iron and steel industry contributes to approximately 6.7% of global carbon emissions [81] and consumes almost 7% of the global energy supply [82]. The GHG emissions from mining and processing in Australia were estimated as 11.9 kg $\text{CO}_{2\text{eq}}$ per ton of iron ore, corresponding to an energy usage of 153 MJ/t ore [83]. However, a significant portion of emissions comes from the blast furnaces (i.e., 70% [81] to 90% [84]). The GHG emissions mostly come from burning coal as a primary energy source, which can be reduced by relying more on green electricity to

meet the net zero scenario requirements. The direct reduction of iron also supports the goal of steel decarbonization [85].

In a typical 60 kWh LFP-based LIB, approximately 41 kg of Fe is used, along with 5.7 kg of Li and 25.5 kg of P [86,87]. LFP comprises 4% Li, 35% Fe, and 61% phosphate [87]. According to Bloomberg New Energy Finance, the demand for Fe will increase by 6.6 times from 2021 to 2030 [88]. The Fe requirements of LFP-based batteries are shown in Fig. 7. The Fe supply is not critical because of the enormous and evenly distributed reserves.

2.4. Phosphorus

In 2020, the European Commission identified phosphorus as a critical raw material with high risk in the supply chain because of its use in energy-intensive industries such as agri-food and aerospace/defense [89]. The critical conditions inspired 500 scientists and researchers to sign the “The Helsinki Declaration” to pressure global policymakers into supporting the sustainable management of phosphorus [90]. Although phosphate reserve depletion is not considered an immediate threat, because the supply is considered sufficient for more than 250 years, resource monopolization is a challenge. In 2008, the price of phosphate rock spiked by 800%, causing a dramatic increase in fertilizer prices. Therefore, significant challenges in P supply include the stable pricing of phosphate and geopolitical equilibrium [91].

The principal global reserves of phosphate rocks were discovered in the western Sahara in Morocco (50 Gt), China (3.2 Gt), Egypt (2.8 Gt), and Algeria (2.2 Gt). Notably, 85% of the global P demand is supplied by a few countries, i.e., 70% by Morocco alone. China and the USA, like other P reserve owners, tend to restrict exports to protect their domestic supplies. A 70 Gt reserve was recently uncovered in Norway (approximately matching the previously disclosed global tonnage). This deposit is large enough to fulfill the P demand from the battery sector and photovoltaics industry for the next 100 years [92]. In addition to ground mines, the marine environment is a rich source of P. However, sustainable strategies must be adopted to obtain P from marine systems [93]. Of the P mined in 2020, 85% was consumed in fertilizers, 10% in supplements for animal feed, and the remainder in other products [47].

Phosphate ores undergo various recovery steps, separation, classification, carbonate removal, and beneficiation. Effective beneficiation depends on phosphate liberation and the existing gangue. Flotation is the preferred mineral processing technique for igneous-type ores and those with silica as the main gangue. Sediments containing calcareous gangue benefit from acid leaching or calcination [94]. H_3PO_4 is a marketable product of the beneficiation of phosphate rock by phosphorus pentoxide (P_2O_5), which is obtained by treating the beneficiated phosphate ore with H_2SO_4 [95]. P is chiefly used in the form of H_3PO_4 .

However, other chemistries, such as phytic acid, have been proposed to have advantages such as binding the LFP particles as a bridge. Phytic acid reacts readily with Fe^{2+} owing to its abundant negative surface charges that are derived from reactive groups ($-OH$ and PO_4^{3-}), which results in excellent interfacial binding [96].

The projected global EV demand requires more than 3 Mt/year of P by 2050, which is equal to 5% of the current global demand. Notably, 25.5 kg of P is consumed in each LFP-type battery [47]. The cumulative phosphorous market for light EV batteries was calculated as 28–35 Mt in 2020–2050. Considering the shortage of P as a critical raw material (as identified by the European Commission [89]), it is worth noting that by 2050, 1 Mt of P could be directly recycled from commercial end-of-life EV batteries. If the recycling achieves 90% efficiency, 20% of the cumulative demand of P could be supplied, i.e., 0.9 Mt of P [97].

3. Raw materials for ACMs

3.1. Elemental Fe

The use of Fe in LIBs is highly favorable because its global reserves are estimated to be 2100 times higher than those of Co, which would dramatically reduce battery fabrication expenses [98]. Metallic Fe has been used in various synthesis methods. Pure Fe has a lower cost and a far higher tap density than ferric salts, making it an ideal iron source for LFP cathodes [99]. Metallic Fe (Fe^0) is primarily used in solid-state synthesis (SSS) [99] and sometimes in hydrothermal processes [100]. As a co-precursor, Fe^0 accelerates the reaction kinetics by reducing Fe^{3+} -containing substances, such as Fe_2O_3 in molten-state synthesis (MSS) [101] or $FePO_4$ in SSS [102], thereby enhancing the Fe^{2+} formation suitable for $LiFePO_4$. It was reported that Fe metal powder and $FePO_4$ combined with Li_3PO_4 achieved 100% atomic efficiency and avoided pore formation in SSS [98]. Hence, a superior tap density of $\sim 1.45 \text{ g}\cdot\text{cm}^{-3}$ (30% higher than that of commercial material) was obtained for the resulting carbon-LFP (C-LFP) composite. Although adopting an economical source of metallic Fe is desirable, it is time-consuming to grind metallic ingot [103]. Table 2 summarizes the raw materials for LFP/LMP/LMFP production, the choice of synthesis method, and the corresponding electrochemical performance (EP).

3.2. Fe_xO_y

Fe_2O_3 is commonly used as the Fe source in SSS. Iron oxide offers the advantages of cost-effectiveness and low environmental pollution, thus creating opportunities for mass production [99]. For example, Fe_2O_3 was used to synthesize a tap-dense C-LFP composite via solid-state carbothermal treatment [105]. Various sizes of Fe_2O_3 particles were used for the SSS of C-LFP ACM [104]. In one method, a commercial unground powder of $\alpha\text{-}Fe_2O_3$ was wet ball-milled to achieve a regular ground shape and smaller size. In another method, $\gamma\text{-}Fe_2O_3$ was synthesized via a solvothermal process followed by sintering using the initial $FeCl_3\cdot 6H_2O$ (electrochemical performance data in Table 2). Fe_2O_3 was used in an SSS process to produce C-LFP [106]. Fe_2O_3 was initially reduced to the transitional phase of $Fe_2P_2O_7$ by $NH_4H_2PO_4$, and then $Fe_2P_2O_7$ was completely reacted with Li_2CO_3 to form $LiFePO_4$. C-LFP was synthesized using inexpensive Fe_2O_3 in an SSS process at 600 °C [107]. A high discharge capacity (DC) of 156 mAh/g (0.1 C) resulted in excellent capacity retention (CR) and rate capability of 78 mAh/g at 20 C. Uniform LFP nanograins (<100 nm) were effectively prepared using nano- Fe_2O_3 with the accelerated kinetics of SSS [108]. The highest performance of 167 mAh/g (0.1 C) was measured after sintering the precursor at 740 °C for 5 h. In addition, Fe_2O_3 was used in continuous SSS to produce nanostructured C-LFP powder in air [109].

Fe_3O_4 has also been used in LFP synthesis. $LiMn_{0.8}Fe_{0.2}PO_4/C$ was synthesized using Fe_3O_4 , MnO_2 , H_3PO_4 , and Li_2CO_3 [120]. The mixture was milled for over 3 h and sintered after spray drying. Excellent cyclic performances, 159 mAh/g at 0.1 C, 129 mAh/g at 10 C, and 95% CR

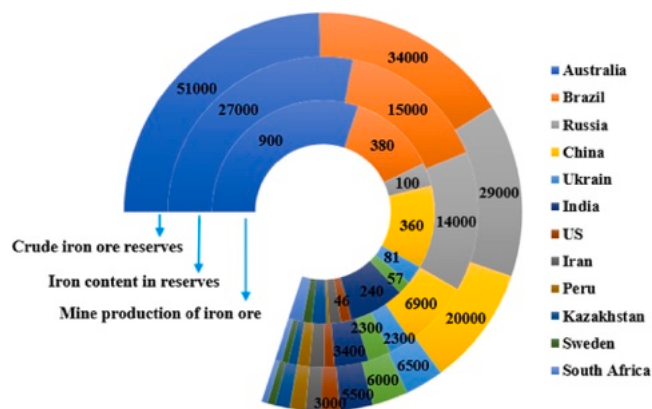


Fig. 7. Global crude iron-ore reserves, iron content in reserves, and mine production (Mt) in 2021. Only the major players are shown for comparison. Data was drawn from [68,69].

Table 2

Various raw materials in LFP/LMP/LMFP production, corresponding synthesis methods, and electrochemical properties. The data are limited to the raw materials and synthesis methods described in this paper (FeO, FePO₄, Fe_xO_y, FeSO₄, and Mn salts in hydrothermal liquid-state synthesis (LSS), SSS, and MSS). CR: capacity retention.

Ref.	RM	Li source	ACM	Synthesis of ACM	EPs
[99]	Fe ⁰	Li ₂ CO ₃	LFP	SSS: Sinter 700 °C 2 h	166 mAh/g (0.1 C) 125 mAh/g (20 C)
[98]	Fe ⁰ , FePO ₄	Li ₂ CO ₃	LFP	SSS: ball mill 12 h Sinter 700 °C 6 h	138 mAh/g (1 C)
[101]	Fe ⁰ , Fe ₂ O ₃	LiPO ₃	LFP	MSS: 1100 °C 3 h	161 mAh/g (0.25 C) 99.5% CR (100 cycles)
[102]	Fe ⁰ , FePO ₄	LiPO ₃	LFP	SSS: ball mill 3 h Sinter 450 °C 3 h 700 °C 8 h	146 mAh/g (0.5 C) 95.2% CR (50 cycles)
[104]	Fe ₂ O ₃	Li ₂ CO ₃	LFP	SSS: ball mill 3 h Sinter 350 °C 6 h 600–700 °C 10 h	150 mAh/g (0.1 C) 96 mAh/g (10 C)
[105]	Fe ₂ O ₃ , FeC ₆ H ₅ O ₇ ·5 H ₂ O	Li ₂ CO ₃	LFP	SSS: planetary ball mill 6 h Sinter 300 °C 10 h 700 °C 24 h	135 mAh/g (0.1 C) 110 mAh/g (1 C) 99% CR (30 cycles)
[106]	Fe ₂ O ₃	Li ₂ CO ₃	LFP	Ball mill 4 h Sinter 700 °C 6 h → Fe ₂ P ₂ O ₇ SSS: ball mill 4 h Sinter 670 °C	153 mAh/g (0.1 C) 94.5% CR (50 cycles)
[107]	Fe ₂ O ₃	Li ₂ CO ₃	LFP	SSS: planetary ball mill 1.5 h Sinter 350 °C 4 h 600 °C 8 h	156 mAh/g (0.1 C) 78 mAh/g (20 C)
[108]	Fe ₂ O ₃	LiH ₂ PO ₄	LFP	SSS: sinter 740 °C 5 h	166.9 mAh/g (0.1 C) 142 mAh/g (10 C)
[109]	Fe ₂ O ₃	Li ₂ CO ₃	LFP	Continuous SSS: planetary ball mill 1 h Sinter 850 °C 20–90 s	136 mAh/g 100% CR (20 cycles)
[110]	FePO ₄ ·2 H ₂ O	Li ₂ CO ₃	LFP	SSS: Ball mill 10 h Sinter 650 °C 8 h	160–107 mAh/g (0.1–10 C) 97% CR (300 cycles)
[111]	FePO ₄	Li ₂ CO ₃	LFP	SSS: Sinter 350 °C 4 h 750 °C 8 h	156 mAh/g (0.5 C) 104 mAh/g (10 C)
[112]	FePO ₄	Li ₂ CO ₃	LFP	SSS: planetary ball mill 6 h Sinter 200 °C 2 h 450 °C 5 h 700 °C 10 h	106 mAh/g (10 C) 99% CR (200 cycles, 1 C)
[113]	Fe ⁰ , FeSO ₄	Li ₂ CO ₃	LFP	LSS: Hydrothermal 50 °C 6 h Sinter 750 °C 8 h	162 mAh/g (0.1 C) 95% CR (200 cycles, 1 C)
[114]	FeSO ₄ ·7 H ₂ O	LiOH·H ₂ O	LFP	LSS: Hydrothermal 180 °C 10 h Sinter 750 °C 6 h	115 mAh/g (1 C) 96% CR (100 cycles, 1 C)
[115]	FeSO ₄ ·7 H ₂ O	LiOH·H ₂ O	LFP	LSS: Hydrothermal 90 °C 8 h Sinter 650 °C 6 h	154 mAh/g (0.5 C) 115 mAh/g (20 C) 88% CR (1000 cycles, 10 C)
[116]	MnSO ₄ ·nH ₂ O	Li ₃ PO ₄	LMP	LSS: Hydrothermal 190 °C 12 h Sinter 700 °C 1 h	135 mAh/g (0.1 C) 83 mAh/g (1 C)
[117]	MnSO ₄ ·nH ₂ O	LiOH·H ₂ O	LMP	LSS: continuous Hydrothermal process 335 °C Sinter 700 °C 3 h	52 mAh/g (0.5 C) 70% CR (200 cycles, 0.1 C)
[118]	FePO ₄ , MnCO ₃	Li ₂ CO ₃	LMFP	SSS: planetary ball mill 6 h Sinter 300 °C 5 h 700 °C 10 h	160 mAh/g (0.1 C) 80% CR (300 cycles, 1 C)
[119]	FePO ₄ , Mn(Ac) ₂ ·4 H ₂ O	LiH ₂ PO ₄ , Li ₂ CO ₃	LM _{0.5} F _{0.5} P	SSS: Ball mill Sinter 700 °C 8 h	167 mAh/g (0.1 C) 140 mAh/g (1 C) 93% CR (200 cycles, 1 C)
[120]	Fe ₃ O ₄ , MnO ₂	Li ₂ CO ₃	LM _{0.8} F _{0.2} P	SSS: various mill 3 h Sinter 700 °C 8 h	159 mAh/g (0.1 C) 129 mAh/g (10 C) 95% CR (1000 cycles, 1 C)
[121]	MnO, FePO ₄	Li ₂ CO ₃	LM _{0.6} F _{0.2} P	SSS: various mill 4 h Sinter 450 °C 4 h 650 °C 6 h	142 mAh/g (10 C) 97.8% CR (300 cycles, 1 C)

after 1000 cycles (1 C) were reported for the final LMFP cathode.

3.3. FePO₄

FePO₄ provides both Fe³⁺ and PO₄ and allows mixing at the atomic scale when used as a raw material for LFP. When Fe₂O₃ or FeSO₄ are used for LFP production, PO₄ is provided as an additional source [110]. However, critical issues must be addressed to synthesize FePO₄. For example, residual moisture must be controlled in FePO₄ to alleviate its reaction with Li⁺ during LiOH production and to prevent reduced capacity and irreversible degradation in subsequent cycles [112,122]. Furthermore, introducing uniformly distributed low-dimensional particles resulted in a high specific surface area and bulk density in the final LFP product, facilitating subsequent Li diffusion. Synthesis optimization for cost-effective scaling should also be considered during FePO₄ preparation. Various sources of Fe and P have been used in FePO₄ production. Examples of Fe sources include FeSO₄, Fe(NO₃)₃, Fe₂(SO₄)₃, and FeCl₃, whereas P sources include H₃PO₄ and (NH₄)₂HPO₄ [122]. Industrial-grade sources have also been investigated to introduce more affordable materials. For example, industrial grade Fe concentrate,

phosphate, and a neutralizing agent were used to hydrothermally synthesize FePO₄ suitable for LFP preparation [123].

There are numerous methods for synthesizing iron phosphates, including precipitation [124,125] or hydrothermal processes [126,127]. Hydrothermal LSS is a promising method because of its simple process, ability to control and regulate the product and synthesis parameters, and suitability for large-scale production [128]. The desired crystallinity and purity of FePO₄ were achieved by controlling the reaction temperature and pH [127]. However, amorphous FePO₄ was hydrothermally synthesized using Fe(NO₃)₃·9 H₂O and (NH₄)₂HPO₄, along with different dispersing agents [126]. A hydrothermal method was used to synthesize FePO₄-single-walled carbon nanotubes using (NH₄)₂Fe(SO₄)₂·6 H₂O and H₃PO as Fe and P sources, respectively [129]. A 3D porous amorphous nanostructure of FePO₄@rGO (reduced graphene oxide) was prepared using a low-temperature energy-efficient synthesis process [130]. Notably, this amorphous composite was obtained by hydrothermal synthesis at 80 °C, followed by low-temperature calcination at 250 °C for 24 h for GO reduction. This process resulted in uniformly distributed nanoparticles (10–20 nm) with limited agglomeration within the 3D interconnected conductive network of rGO. A simple

low-temperature (80 °C) hydrothermal method was applied to produce FePO₄ from iron (II) ammonium sulfate and H₃PO₄ [131], resulting in a porous structure of amorphous FePO₄ interconnected with single-walled carbon nanotubes. Li et al. compared the preparation of FePO₄ from FeSO₄·7 H₂O via the introduction of an intermediate transformation to Fe₃(PO₄)₂, with a process that shifted dominantly from Fe³⁺ to FePO₄ [110]. The latter approach is more efficient, resulting in smaller FePO₄ particles. Furthermore, a quick precipitation method was demonstrated for synthesizing FePO₄·2 H₂O nanoparticles with narrow-size distribution [132,133]. By regulating the H₃PO₄ content mixed with Fe(NO₃)₃, they obtained α-FePO₄ with high purity. Accordingly, they developed a rapid, straightforward approach for producing α-FePO₄-carbon nanotube nanocomposites through immediate precipitation with the aid of a microreactor.

3.4. FeSO₄

Numerous precursors and synthesis methods are available for producing ferrous sulfate species. This section reviews only the compounds that produce battery-grade FeSO₄ to provide LFP with sufficient electrochemical performance. FeSO₄ is significant because it can be produced from the inexpensive slags of TiO₂ as a byproduct with up to 99.7% purity. FeSO₄ obtained from slag undergoes purification through several steps, including the reduction of ferric iron to ferrous iron with the aid of a reducing agent; removal of heavy metals such as Co, Ni, Zn, Cu, Pb, and Cd using ferrous sulfide; elimination of Ca and Mg ions with fluoride; crystallization; and vacuum drying. Using slags to produce FeSO₄ and LFP is an economical and environmentally friendly strategy [134].

Using impure FeSO₄·7 H₂O, pure crystalline FePO₄·xH₂O was successfully prepared and used for LFP production, which achieved a DC of 149 mAh/g (0.1 C) that was maintained above 120 mAh/g over 100 cycles (2 C) [135]. Polyacrylamide was used as a flocculant to purify FeSO₄·7 H₂O waste slag [115]. The purification process involved the reduction of Fe³⁺ to Fe²⁺ using Fe, polyacrylamide induction, acid reduction using H₂SO₄, and subsequent filtration. The resulting FeSO₄ was used to synthesize battery-grade LFP with and without transformation into a transitional crystalline Fe₃(PO₄)₂·8 H₂O structure. The capacity of LFP was measured to be 130 mAh/g (10 C) and reached 112 mAh/g after 1000 cycles. The initial impurities in these cost-effective precursors must be reduced sufficiently for battery-grade LFP production. This issue was addressed by Al/Ti precipitation purification and a subsequent selective synthesis to produce battery-grade FePO₄·2 H₂O while using the iron recovered from FeSO₄ [136].

3.5. MnSO₄

Battery-grade Mn precursors have been used to synthesize LMFP using various methods, including sol-gel [137], hydrothermal LSS [116], SSS [138], and MSS [139]. Various raw materials, such as MnSO₄, MnPO₄, MnCO₃, MnCl₂, and Mn₂O₄ [140] have been used for LMP/LMFP synthesis. Various Mn precursors were used in solvothermal LMP synthesis [141]. The LMP derived from MnSO₄, MnCl₂, and Mn(Ac)₂ delivered DC values of 145, 129, and 81 mAh/g (0.01 C), respectively. MnCl₂-based LMP maintained 91% capacity (200 cycles at 2 C) owing to its high purity and specific crystal orientation along the ac planes. MnCO₃ and FePO₄ were utilized as the Mn and Fe sources, respectively, along with Li₂CO₃ and NH₄H₂PO₄ as the Li and P sources, respectively, for the synthesis of LiMn_{0.5}Fe_{0.5}PO₄ by an SSS method [118]. Manganese acetate (C₄H₆MnO₄), lithium acetate (C₂H₃LiO₂), and H₃PO₄ were used as initial raw materials for hydrothermal LMP synthesis [142].

MnSO₄ has shown promise as an initial raw material in manganese chemistry. For example, MnSO₄ was used in the hydrothermal synthesis of LMP [116], while MnSO₄·H₂O was used in combination with Li₂SO₄·H₂O and Na₃PO₄·12 H₂O as Li and P sources for the synthesis of

LMP via SSS methods at 700 °C for 2 h [143]. MnSO₄·H₂O and Li₃PO₄ were used in the solvothermal synthesis of LMP at 180 °C for 4 h, followed by sintering at 600 °C for 3 h [144]. A continuous hydrothermal process was proposed for LMP synthesis using MnSO₄·nH₂O and LiOH·H₂O [117]. Furthermore, LMP was prepared via a solvothermal synthesis using LiOH·H₂O, H₃PO₄, and MnSO₄·H₂O [145,146]. Finally, N-doped LiMn_{0.8}Fe_{0.2}PO₄ nanocrystals were synthesized using MnSO₄·H₂O, FeSO₄·7 H₂O, LiOH·H₂O, and H₃PO₄ via a solvothermal reaction [147].

4. Synthesis of ACMs

Reviews of a wide range of cathode materials for LIBs have been published in recent years [148–154]. Herein, we focus on olivine materials, specifically LFP, LMP, and LMFP, along with their synthesis procedures. In recent years, efforts have been made to overcome the low conductivity of LiXPO₄ and enhance its Li-ion diffusion coefficient (D_{Li}). These goals can be attained by focusing on the following aspects:

(I) Enhanced electronic conductivity: Various carbon sources, such as surface carbon layers or conductive carbon additives, can improve charge transfer [155].

(II) Increased Li-ion conductivity: This can be achieved by cationic doping or by reducing the particle size. Kinetically, the diffusion of Li⁺ controls charge/discharge rather than electron transfer. This phenomenon was due to the lower ionic conductivity of Li⁺ (10⁻¹¹–10⁻¹⁰ S/cm at room temperature for LFP) compared to the electronic conductivity (>10⁻⁹ S/cm at room temperature). Hence, shortening the Li-ion diffusion path is crucial to facilitate Li⁺ transfer. This can be achieved primarily by controlling the size of LFP crystals, particularly along the b-axis [19,156,157]. It is noteworthy that nanosizing may negatively impact the energy and tap densities. Porous materials and extended nanoarchitectures have been proposed as potential solutions [14].

(III) Reducing the defect density: The main difficulty in the synthesis of orthophosphate LFP comes from the presence of two different iron oxidation states (Fe(II) and Fe(III)). Fe³⁺ impurities can hinder the preparation of LFP with nonreproducible electrochemical performance [158]. Depending on the employed synthesis method, the produced impurities can poison LFP by occupying the M1 sites within the olivine structure, thereby blocking the Li-ion pathway [159].

These issues have been addressed in three primary synthesis methods: liquid, solid, and molten states, which are reviewed in detail in this study. The synthesis parameters were obtained from the literature to provide a comprehensive overview of the effective parameters for further experimentation.

4.1. Liquid-state hydrothermal process

Hydrothermal LSS is considered a viable commercial route for olivine production [158]. Although solvothermal processes are of broad interest [160–162], we omit this method here because of its detrimental effects and the goal of the battery industry to develop green techniques. The hydrothermal method is one of the cheapest methods for olivine production. However, the widespread use of olivine materials in batteries requires further investigation to develop the desired products for real applications. Hydrothermal processes are generally conducted in polytetrafluoroethylene-lined autoclaves fired in a tube furnace in an inert medium to prevent Fe²⁺ from oxidizing Fe³⁺. A summary of the various approaches drawn from the literature is presented in Table 3.

The precursor composition affects the final LFP structure and purity, which are directly related to Fe oxidation during the hydrothermal step [165]. A comparison of three Li sources, including LiOH·H₂O, LiCl, and Li(CH₃COO), showed that the Li source (or solution pH) significantly influences the morphology and crystal orientation [165]. LiOH (basic pH of 9) resulted in the smallest particles with a size of less than 1 μm with random crystal textures. Using LiCl (acidic pH of 3.4), the largest particles were formed as thin flakes primarily oriented along the (200)

Table 3

Comparison of raw materials and hydrothermal synthesis parameters for LFP, LMP, and LMFP and the corresponding electrochemical properties. A: autoclave condition; D: drying condition; B: burning condition; DEC: diethyl carbonate; EC: ethylene carbonate; DMC: dimethyl carbonate; LP30: 1 M LiPF₆ in 1:1 EC:DMC electrolyte, t: thickness; W: width; L: length; NMP: N-methyl-2-pyrrolidone; PTFE: polytetrafluoroethylene; PVDFHFP: polyvinylidene fluoride-co-hexafluoropropylene; VGCF: vapor grown carbon fiber.

Ref.	Raw Materials	Synthesis	Product	Battery test	Battery characteristics	Highlights
[163]	LiOH, FeSO ₄ , H ₃ PO ₄ , C ₆ H ₈ O ₇ , NH ₃ , polysaccharides/lactose	A: 200 °C 2 h D: Not mentioned B: 700 °C 3–5 h	LMP: 6 μm	Laminate batteries, carbon black (CB)+ fibrous carbon, PVDF in NMP, LiPF ₆ in 3EC:7DEC	500 mAh 90% CR (1000 cycles)	Improved EP by different shaped carbon sources
[164]	LiOH·H ₂ O, MnSO ₄ ·H ₂ O, FeSO ₄ ·7 H ₂ O, (NH ₄) ₂ HPO ₄ , H ₃ PO ₄ , C ₆ H ₈ O ₆ , lactose	A: 220 °C 7 h D: 90 °C 12 h N ₂ B: 400 °C 1 h–600 °C 3 h	LMP core (66%)– C-LFP shell (33%) particles or LiMn _{0.66} Fe _{0.33} PO ₄ flakes 10–100 nm t	Coins, super C65 carbon, Denka black, PVDF in NMP, LP30	Core-shell: 65 mAh/g (10 C) Blended structure: 23 mAh/g (10 C)	Better performance in core-shell versus the blended structure
[165]	Li sources (LiCl, Li(CH ₃ COO), LiOH·H ₂ O), FeSO ₄ ·7 H ₂ O, (NH ₄) ₂ HPO ₄	A: 170 °C 12 h D: 100 °C 1 h N ₂ B: not mentioned	(200) crystals using LiCl 1–2 μm (020) flakes using Li(CH ₃ COO) random crystals using LiOH·H ₂ O	2016 coins, Ketjen black, PTFE, LiClO ₄ in EC:DEC	Li(CH ₃ COO): 147 mAh/g (0.1 C) 32 mAh/g (2 C)	Li(CH ₃ COO): The lowest particle size, the highest EP
[159]	LiOH·H ₂ O, FeSO ₄ ·7 H ₂ O, CaSO ₄ ·2 H ₂ O, H ₃ PO ₄ , C ₆ H ₈ O ₆ , lactose, NH ₄ OH	A: 180 °C 5 h LFP A: 180 °C 30 min Ca-LFP D: 95 °C overnight B: 700 °C 3–5 h N ₂	NPs in Ca-LFP, 4% Fe defects in LFP, 1% in Ca-LFP	2032 coins, Denka black and VGCF, PVDF in NMP, LP30	Ca-LFP 150 mAh/g (0.08 C), 75 mAh/g (10 C),	30 min synthesis time for Ca-LFP (5 h for LFP), less Fe anti-site defects, smaller particle size
[156]	LiOH·H ₂ O, FeSO ₄ ·7 H ₂ O, H ₃ PO ₄ , SDBS, C ₆ H ₈ O ₆ , sucrose	A: 170 °C 24 h D: 60 °C 12 h B: 350 °C 4 h, 650 °C 9 h	NPs (200 nm) NRs (90 nm D, 200 nm–1 μm L) NPLs (20 nm t, 50 nm W) upon SDBS	2032 coins, acetylene black, PVDF in NMP, LP30	NPs:NRs:NPLs 145:149:163 mAh/g (0.1 C) 34:61:108 mAh/g (10 C)	Better DC and D _{Li} by lower dimension in the b-axis
[166]	LiOH, FeSO ₄ ·7 H ₂ O, Mn(NO ₃) ₂ , H ₃ PO ₄ , C ₆ H ₈ O ₇ ·H ₂ O, Ammonia	A: 180 °C 12 h D: 95 °C 24 h B: no burning	–	2032 coins, carbon black, PVDF in NMP LiPF ₆ in 2EC:1DMC	157 mAh/g (0.1 C) 100% CR (50 cycles)	No calcination Doped olivine with high stability
[167]	LiOH·H ₂ O, Fe(NO ₃) ₃ ·9 H ₂ O, Mn(CH ₃ COO) ₂ ·4 H ₂ O, H ₃ PO ₄ , C ₆ H ₈ O ₆ , HNO ₃ , C ₃ H ₇ NO	A: 180 °C 12 s D: 60 °C overnight B: 700 °C 3 h	100–200 nm NPs	Coins, graphite, acetylene black, PVDFHFP in NMP, LiPF ₆ in 2EC:1DMC	LiMn _{0.1} Fe _{0.9} PO ₄ 158 mAh/g, 98% CR (30 cycles), LiMn _{0.2} Fe _{0.8} PO ₄ 160 mAh/g (0.1 C)	D _{Li} improvement by Mn doping, high stability

plane. In contrast, thick flakes of 1–2 μm (020) were produced by introducing Li(CH₃COO) (pH of 5.11). The yield as a ratio of Fe²⁺ present in the starting material to LiFePO₄ was dependent on the initial conditions, i.e., a high yield greater than 90% was obtained for a pH above 5 and a low yield of 55% was achieved under acidic conditions using LiCl due to the higher solubility of LiFePO₄ in acidic media. The DC was maximized (147 mAh/g) using Li(CH₃COO) because of the (020) crystal orientation, which is the preferred orientation for Li⁺ ion diffusion along the b-axis inside the LFP crystals. The crystal texture was the major factor affecting the electrochemical performance of the LFP. Furthermore, the effect of the C–LFP morphology on the electrochemical response was investigated [156]. A significant decrease in the b-axis diameter was observed as the morphology changed from nanoparticles (200 nm) to nanorods (90 nm diameter along the b-axis and 0.2–1 μm length) to nanoplates (20 nm thickness along the b-axis and 50 nm width) (Fig. 8) with the addition of sodium dodecyl benzene sulfonate (C₁₈H₂₉SO₃Na) as an anionic surfactant. The reduced particle size enhanced the DC values, namely 145, 149, and 163 mAh/g at 0.1 C and 34, 61, and 108 mAh/g at 10 C, respectively, along with D_{Li} values of 1.66 × 10⁻¹², 2.99 × 10⁻¹² and 16.4 × 10⁻¹² cm²/s, respectively. Smaller crystallite sizes along the b-axis and the higher specific surface area of the (010) plane resulted in shorter Li-ion diffusion paths and better

electrochemical performance of the corresponding LFP. Smaller particles directly provide a considerable drop in ohmic resistance by facilitating faster Li⁺ diffusion, thereby enhancing the charge–discharge behavior [165]. Carbon nanotubes were applied as heterogeneous nucleation sites for fine non-aggregated particles, along with phytic acid as a green P source for LMP synthesis [168]. The rate capability reached 134 mAh/g (1 C) with 95% CR over 100 cycles and 100 mAh/g at 5 C. The fabricated composite benefited from the shorter diffusion path of Li ions because the nanoparticles reduced the intercalation time of the Li ions in the LMP lattices. Electron transport was also accelerated because of the continuous and barrier-free transfer route attributed to the carbon nanotubes in the three-dimensional networks. The aggregated particles may create new active surfaces for the reaction of LMP with the electrolyte owing to introduced cracks. Accordingly, the Li consumed by side reactions at the electrolyte/electrode interface leads to a slight degradation of the active material and fading capacity.

It should be noted that the production of a small number of Fe antisite defects during hydrothermal synthesis deteriorates the performance of olivine. The Li ions in LFP transported through one-dimensional channels are easily blocked by defects or impurities. To ensure a crystalline structure and eliminate contaminants such as Fe-antisite defects and stacking faults, an increase in the reaction

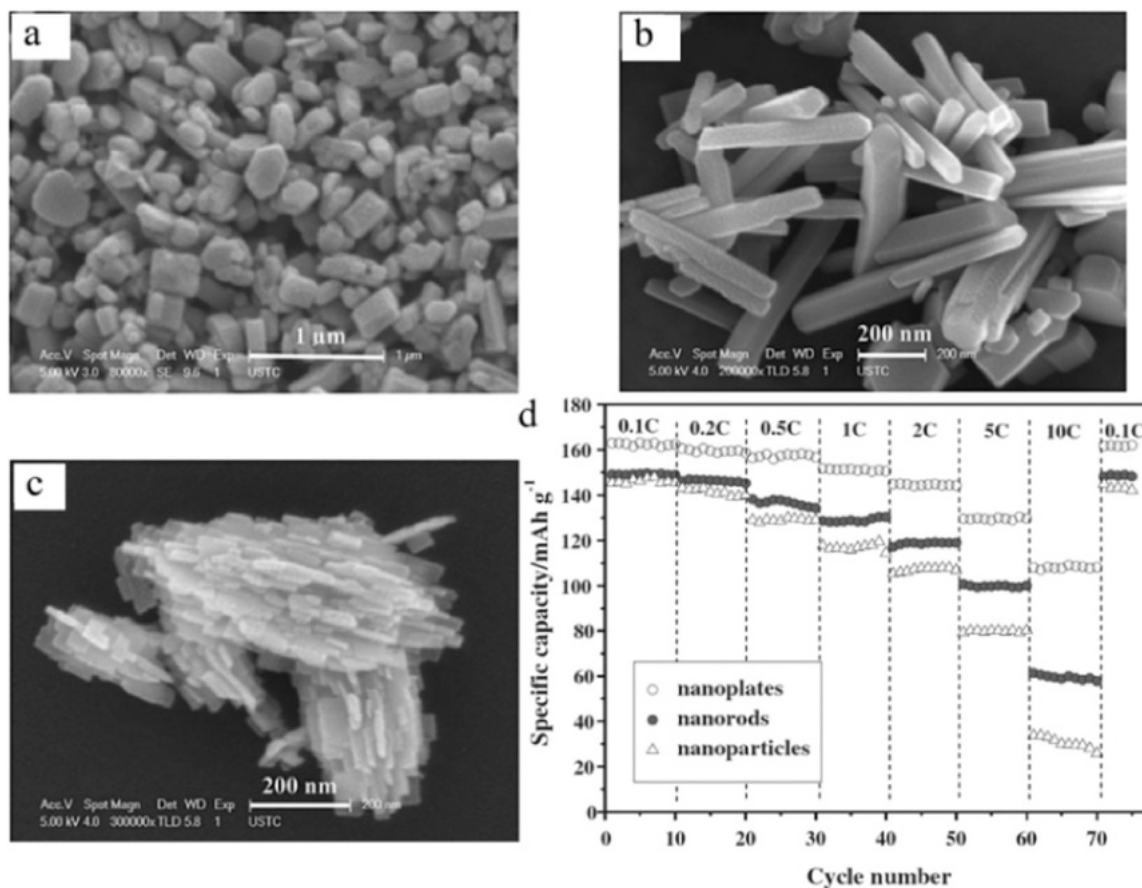


Fig. 8. Field-emission scanning electron microscopy images of C-LFP (a) nanoparticles, (b) nanorods, and (c) nanoplates. (d) C-LFP cycling performance (0.2 C charge rate to ensure the exact discharge condition). Reproduced with permission from [156].

temperature and the use of high-pressure reactors have been suggested [169]. It was shown that metal disorder could be significantly improved by increasing the synthesis temperature, i.e., from 8% at 120 °C to 0% at >175 °C [170]. They also analyzed the effects of chemical agents on minimizing the oxidation of ferrous ions to ferric ions. Accordingly, aqueous ascorbic acid prevents this formation more effectively than hydrazine or sugar. A study focusing on defects revealed that adding calcium cations to the initial mixture (via calcium sulfate) can efficiently facilitate the removal of these defects in two ways: 1) by enhanced nucleation and limited growth of the LFP particles at the nanoscale and 2) by the aggregation of Fe defects at the surface, but not in the bulk, which accelerates their removal during calcination [159]. The Ca ions prevented the placement of Fe ions at the M1 sites of the olivine structure, which blocked the pathway for Li⁺ diffusion. This explanation was confirmed by collecting the intermediates of LFP and Ca-LFP at different times and by high-angle annular dark-field imaging in scanning transmission electron microscopy. The effect of temperature (120–175 °C) on the properties of LFP produced from LiOH, FeSO₄, and H₃PO₄ was investigated in the hydrothermal synthesis [171]. They found that a threshold temperature of 135 °C is critical for the rapid nucleation of LFP. Increasing the temperature resulted in a sharp decrease in the flake thickness, i.e., from 130–150 nm at 120 °C to 80–90 nm at 175 °C. The optimal reaction temperature above 160 °C resulted in LFP with DC of 161 and 122 mAh/g at 25 and –20 °C, respectively. Furthermore, the production of battery-grade low-defect LFP platelets via a low-temperature hydrothermal route was achieved by varying the precursor concentration [172], resulting in a DC of 150 mAh/g with 30% less energy consumption than the product obtained in SSS. This study presented an excellent graph of the relationship between energy consumption, reaction temperature, and precursor concentration, as

reproduced in Fig. 9.

The firing/combustion process is crucial for forming C-LFP, and adding an organic carbon source to the initial LFP precursors facilitates the formation of desirable C-LFP compounds for batteries. The formation of a carbon coating via the decomposition of the organic material accelerates the kinetics of Fe³⁺ reduction by reducing hydrogenous gas at 500–700 °C and alleviating the formation of Fe₂O₃ nanoparticles [173]. Transmission electron microscopy observations demonstrated that the optimal calcination temperature of 650 °C resulted in a sharp

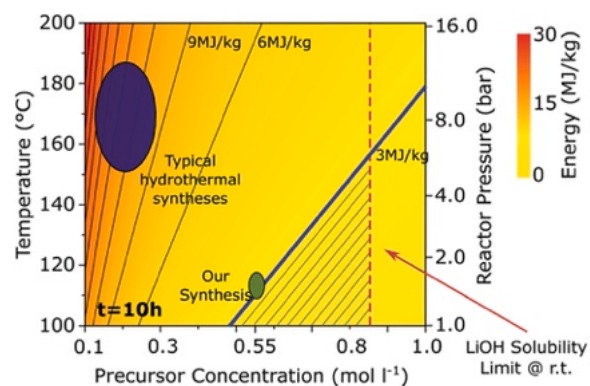


Fig. 9. Energy consumption of the hydrothermal step of LFP synthesis versus temperature, precursor concentration, and reactor pressure. The line at 3 MJ/kg line represents the energy consumption of the solid-state route. The shaded region under this line corresponds to hydrothermal synthesis with specific temperatures and related precursor concentrations with less energy consumption than the solid-state method. Reproduced with permission [172].

interface between LFP and the carbon coating [12]. A firing temperature range of 500–800 °C with a preferential range of 650–750 °C was proposed [163]. Above 800 °C, a more significant fraction of Fe₂P nanoparticles are produced, driving the superferromagnetism. Although Fe₂P increases the electronic conductivity owing to its metallic properties, the ionic conductivity decreases accordingly, resulting in lower capacity. The quick dissolution of nanoparticles inside the electrolyte significantly reduces battery life [173]. An excellent summary related to the effect of temperature on the appearance of Fe-containing species was published by Zaghbi et al. [15] (Fig. 10). This contradictory effect on the conductivity was also observed in the presence of a carbon coating layer. While enhanced electron conductivity is achieved by reducing the particle size and eliminating growth and aggregation, Li-ion conductivity decreases when a thick carbon layer is used. Thin and uniform 0.5–2 wt % carbon coatings were achieved [17]. Further discussion of the carbon compositions is beyond the scope of this work, and the reader is referred to other studies [17,174,175].

In LiXPO₄ research, working on LFP, LMP, and LFP-LMP seems to be more realistic. Implementing LCP and LNP in LIBs in laboratory-scale experiments is difficult despite their high working voltages [17,19]. To reach a realistic application performance, surface modification via carbon coatings [169], the use of a sacrificial intermediate LiCoPO₄ tetra phase in the hydrothermal step [176], or heating by microwaves [169, 177–181] have been proposed. However, a blended structure with LFP is promising despite the mutual and synergistic effects owing to the high potentials of Mn, Co, and Ni compared to that of Fe and the high stability of LFP. LiMn_xFe_{1-x}PO₄ (x=0.1 and 0.2) was developed using Mn (CH₃COO)₂·4 H₂O and Fe(NO₃)₃·9 H₂O as the initial transition-metal precursors and LiOH·H₂O, H₃PO₄, C₆H₈O₆, HNO₃, and a small quantity of C₃H₇NO reducing agent [167]. Mn doping increased *D*_{Li} by two orders of magnitude compared to LFP and demonstrated a stable cycling response after 50 cycles. Similarly, the addition of Mn(NO₃)₂ to the initial mixture of LiOH, H₃PO₄, FeSO₄·7 H₂O, and C₆H₈O₇ resulted in

Mn-doped LFP as LiMn_xFe_{1-x}PO₄ (x = 0, 0.1, 0.2, and 0.3) [166]. The enhancement of Mn substitution promotes electron transfer and Li transport by reducing the particle dimensions and extending the lattice parameter. Increasing x from 0 to 0.3, the LMFP exhibited excellent cycling stability, showing 100% CR (157 mAh/g at 0.1 C) over 50 cycles. An exciting aspect of their investigation was the omission of a calcination step, whereas the coating of hydrothermally synthesized olivine with carbon was achieved through pyrolysis.

A three-step process for fabricating an LMP-LFP composite was presented based on the hydrothermal synthesis of LiMnPO₄, its addition to the LFP precursor solution followed by hydrothermal synthesis, and carbon-coating via the combustion of lactose (600 °C-3 h) [164]. This process results in LMP being encapsulated in C-LFP via the Fe-C catalytic reaction (Fig. 11). They showed that a layered blended LFP-LMP (66:33) material performed better in terms of the discharge rate than LiMn_xFe_{1-x}PO₄ with the same Fe content (x = 0.33). However, minimizing the synthesis time should be considered as a vital cost-reducing factor in the large-scale synthesis of olivines, and a three-step process would not be attractive.

A two-step green synthesis route for C-LFP was developed [182]. First, FePO₄·2 H₂O was synthesized using Fe₂O₃ NPs and H₃PO₄. At this stage, the waste contained water and excess H₃PO₄. Second, C-LFP was obtained by annealing a mixture of FePO₄·2 H₂O from the previous step, Li₂CO₃, and glucose at elevated temperatures. The glucose introduces CO₂ and water vapor. The C-LFP prepared this environmentally friendly process with 2.2 mg/cm² loading showed acceptable DC values of 161 and 119 mAh/g at 0.1 C and 10 C, respectively, with an impressive CR of 95% at 5 C after 200 cycles. Most processes for producing olivine materials produce wastewaters containing anion impurities such as SO₄²⁻, Cl⁻, and NO₃⁻, as well as exhaust gases such as N_xO_y, CO, and NH₃ [182]. Considering that these gaseous pollutants must be removed because of global warming issues, concepts such as battery passports [6,183] need to be discussed in their field. However, dealing with such contaminants

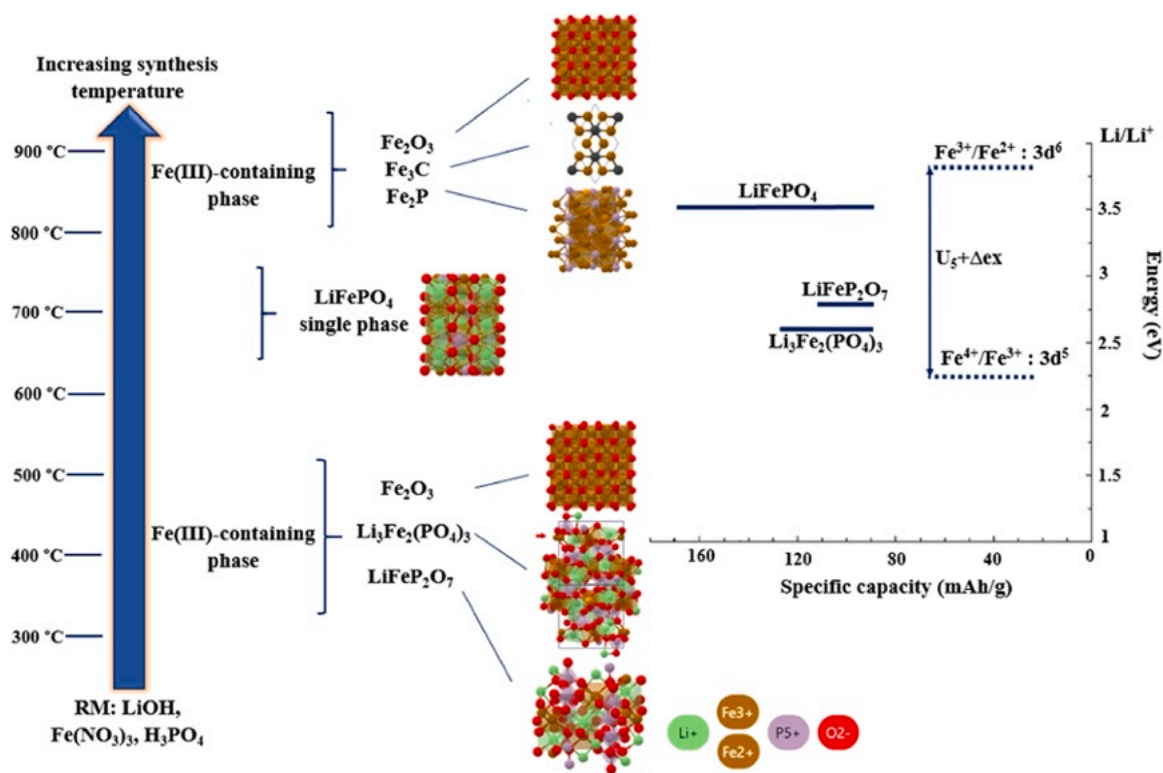


Fig. 10. Representative formation of various Fe-containing compounds during LFP synthesis. The energy of Li-Fe redox couples vs. theoretical specific capacity (mAh/g) in phosphate frameworks.

(a) Reproduced with permission from [15]. (b) Crystal structures are adapted from The Materials Project.

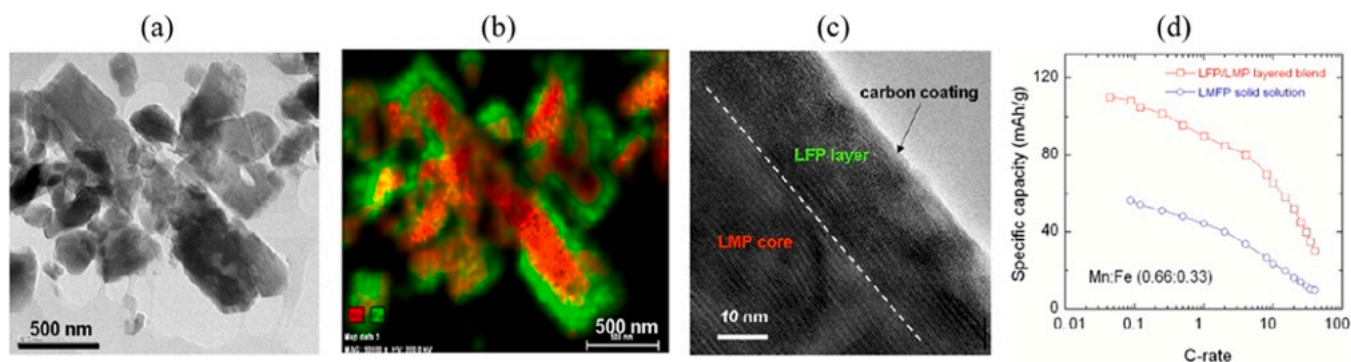


Fig. 11. (a) Transmission electron microscopy (TEM) micrograph of the LMP-LFP blend; (b) elemental map showing the presence of LMP in red and LFP in green; (c) high-resolution TEM image of the interfaces of LMP, LFP, and carbon; (d) specific capacity of LMP-LFP composite with an LMFP solid solution. With permission from [164].

on an industrial scale requires specialized equipment, which increases costs. Therefore, finding methods to create zero-waste olivine structures is interesting.

In conclusion, combining all/some of the suggested solutions could be beneficial for obtaining better electrochemical performance from LSS LFP, LMP, and LMFP. Smaller particles, optimized hydrothermal and calcination processes, metal doping in blended structures to take advantage of the synergistic effect of dopants, and green synthesis methods must be considered to achieve the desired products and promote their broader application in LIBs.

4.2. Solid-state synthesis

The hydrothermal method yields small high-purity particles with a uniform size distribution. In contrast, SSS is a conventional LFP production method that benefits from the simple, efficient, and large-scale preparation of highly ordered crystals. However, the major drawbacks are the lack of suitable control, high temperatures, and long processing times, which lead to aggregation and particle growth [17,103,158].

SSS is a two-step process. First, the mixed and ground/milled precursors are heated to 300–400 °C for decomposition and removing volatile gases. Second, the mixture is ground again, composited with carbon, and calcined at 600–800 °C for 10–36 h. The type of precursor and calcination parameters define the morphology of the final material (Fig. 12) and its resulting electrochemical performance. Repeated grinding and calcination is a long complex process and the elevated temperatures lead to unwanted growth and agglomeration of the particles. The carbon/carbonate anions can prevent undesirable growth and reach the nanoparticles [169]. Super P carbon black or acetylene black was mixed with an initial mixture of Li_2CO_3 , MnCO_3 , and $(\text{NH}_4)_2\text{HPO}_4$ to prepare a C-LMP (20 wt% carbon) [184]. Mixing carbon in the ball mill seemed less effective when using acetylene black than Super-P because of the graphene-like nature of the outer shell of acetylene black, leading to larger C-LMP crystals. In addition, 4–5% Li:Mn cation mixing was observed, which could block the Li-diffusion channels along the b-axis and deteriorate the electrochemical performance. The carbon coating also assists in overcoming the stability challenges faced by high-capacity/high-voltage LiXPO_4 cathodes [185]. It should be noted

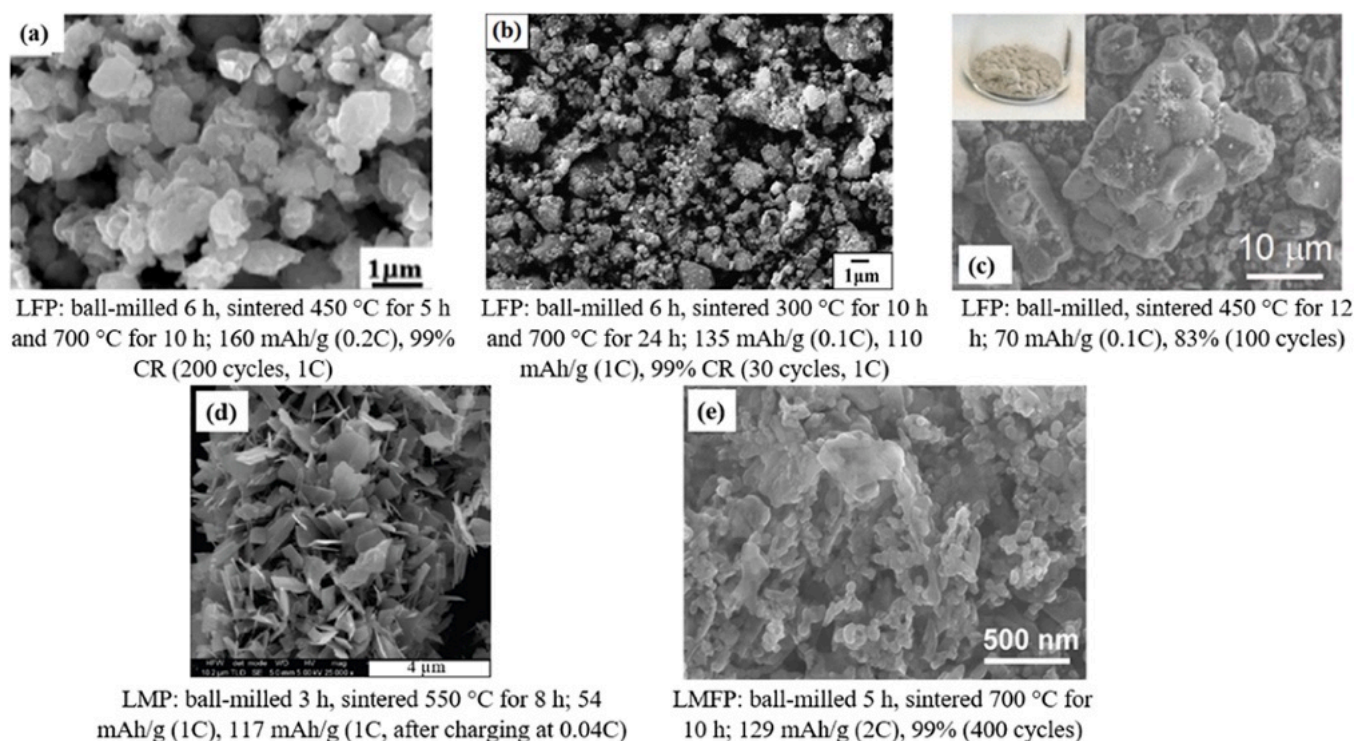


Fig. 12. SSS products and their corresponding electrochemical performance. With permission from (a) [112], (b) [105], (c) [187], (d) [188], and (e) [138].

that while reducing the particle size to the nanoscale with the aid of carbon additives can enhance D_{Li} and improve the electrochemical performance, the size must be optimized for each synthesis method. It was shown that decreasing the reaction temperature from 750 to 550 °C resulted in a decrease in particle size of $LiXPO_4$ from 1000 to 150 nm, respectively, which enhanced D_{Li} but decreased the electron conductivity by quantum confinement effects [186].

A study of hydrous and anhydrous $FePO_4$ raw materials showed that the gases produced by $FePO_4 \cdot 2 H_2O$ decomposition resulted in a non-uniform carbon coating and a broad particle size range [112]. A lower average C-LFP particle size of 63 nm was obtained using anhydrous $FePO_4$ compared to 77 nm for that produced using hydrous $FePO_4$. The optimal performance of 160–147 mAh/g DC (0.2–1 C) and 99% CR (200 cycles, 1 C) was measured for C-LFP utilizing anhydrous $FePO_4$ and 0.4 molar ratio carbon, sintered at 700 °C. Another study compared the use of a Fe: $FePO_4$ mixture (1:2 ratio) as the Fe source [102]. They also worked on various secondary sources of Li rather than the Li_3PO_4 primary source (0.05–0.15 molar ratio of secondary to primary sources). They showed that among the different Li compounds of Li_2CO_3 , LiOH, CH_3COOLi , $C_6H_5Li_3O_7$, and Li_3PO_4 , Li_2CO_3 -derived C-LFP exhibited the best performance, i.e., 146 mAh/g DC and 95% CR (0.5 C after 50 cycles). The excellent performance could be due to the elimination of impurities and modification of the SSS path by the introduction of excessive Li_2CO_3 . Furthermore, natural as-mined siderite mineral (Paleozoic $FeCO_3$) was used to synthesize inexpensive LFP for the first time [187]. However, the mineral's low purity (~92 wt%) resulted in LFP with a low capacity of 80–110 mAh/g (0.1 C). The impurities possibly deteriorated the electrochemical performance by substituting key lattice sites and blocking the Li-diffusion path. In addition, LMFP (0.8 Mn and 0.2 Fe) was synthesized using alternative sources of Fe, including $Fe(NO_3)_3$, FeC_2O_4 , and Fe_2O_3 [138]. The substitution of Fe in the $LiMnPO_4/C$ structure occurs during the SSS. The LMFP prepared using $FeNO_3$ exhibited a 129 mAh/g (2 C) DC and excellent cyclability, i.e., 99% after 400 cycles. The cell volumes of LMFP from different precursors lying between the compositions of LMP and LFP suggested that Fe enters the LMP lattice. The larger cell parameters obtained when using $Fe(NO_3)_3$ revealed that, in addition to substitution, soluble Fe (NO_3)₃ on the MnO surface limits the growth of LMP particles and forms the LFP phase on the LMP surface.

Additives also have a substantial effect on the final products. Oleic acid was used as the surfactant along with molten paraffin hydrocarbons to assist in the SSS of LMP by facilitating the thermodynamically preferred growth of LMP nanoplates without agglomeration [188]. A redox potential of approximately 4.1 V vs. Li/Li⁺ was obtained, with DC values of 54 mAh/g (1 C) and 117 mAh/g (1 C, after charging at 0.04 C). Slight capacity fading after 50 cycles was reported.

4.3. Molten-state synthesis

MSS is advantageous for melting raw materials near their eutectic temperatures. The eutectic mixture lowers the melting point and reduces energy consumption. MSS benefits from its versatility, fast reactions, and utilization of low-cost raw materials, while the obtained product is of high homogeneity and crystallinity [103]. Iron-ore concentrates are among the cheapest raw materials. Metallic iron is also used to elevate the Fe^{2+} content and enhance the reaction kinetics via the following reaction: $Fe_2^{3+}O_3 + Fe^0 \rightarrow 3Fe^{2+}O$ [101]. Unfortunately, a premixing step is required to prevent powder agglomeration and make the eutectic possible in the $LiPO_3$ -Fe- Fe_2O_3 ternary system [189]. Metallic Fe consists of impurities that are inserted into the LFP structure during MSS. Impurity cations in an Fe-rich melt are inserted into the LFP lattice based on the formula $(Li_{1-z}A_z)(Fe_{1-y}M_y)(P_{1-x}Si_x)O_4$ (where A and M refer to cations in the iron precursors). The electrochemical performance, mainly the capacity and cycle life, was strongly affected by this insertion, whereas it had no significant impact on the electron conductivity or power performance. Addressing this issue was challenging and required

the proper adjustment of the melt to obtain purer LFP with a performance approaching that of pure LFP made from the Fe_2O_3 precursor [101]. The presence of other impurities, such as $Li_3Fe_2(PO_4)_3$ (a common contaminant that poisons LFP), can be prevented by working under an N_2 atmosphere because the low hydrogen content in the inert gas is sufficient to act as a reductant for iron and to eliminate such impurities [190]. The injection of CO has also been suggested as a reducing agent to boost the Fe^{2+} content via melt protection [189]. However, this also has an environmental impact.

Despite the advantages of MSS, it suffers from high energy consumption and requires a long grinding process of the prepared ingot [103]. Although producing LFP nanoparticles approaching 25 nm by MSS ingots is possible, the grinding and subsequent milling steps result in a long processing time. Such energy-depleted particles usually agglomerate as secondary particles with sizes of up to 100 nm [190].

In addition to the energy-consuming MSS process, MSS-fabricated LFP requires carbonization at elevated temperatures (as in hydrothermal synthesis and SSS). It was shown that heat treatment at 700 °C is essential after MSS [191]. This calcination step enhances the electron conductivity by adding a carbon coating that improves the electrochemical performance owing to the enhanced recrystallization and omission of structural disorder at the surface. Impurity-free C-LFP (2 wt % C) was prepared with DC values of 157 mAh/g (0.1 C) and 120 mAh/g (10 C) and no capacity fading for 60 cycles. MSS was also utilized for the dry preparation of $LiMn_xFe_{1-x}PO_4$ ($0 \leq x < 1$) [139]. The MSS-derived LMFP with $x < 0.25$ and no impurities demonstrated comparable electron conductivity and crystallinity (100–175 nm) compared to LFP or LMFP (79% Mn) prepared by SSS. The Fe/Mn ratio in Li spots was below 1.5%. Table 4 summarizes some literature on the LFP/LMFP melt synthesis case.

Table 4
MSS-prepared LFP/LMFP and the corresponding electrochemical properties.

Ref.	Olivine	RMs	MSS	Battery characteristics
[101]	LFP	$LiPO_3$, Fe_2O_3 , Fe^0 , carbon black, lactose	Melting 1100 °C 3 h Ball mill 3 h Carbonization 700 °C 2 h	158 mAh/g (0.1 C) 105 mAh/g (10 C) High CR (100 cycles)
[191]	LFP	Li_2CO_3 , $FePO_4 \cdot 2 H_2O$	Melting 1050 °C 5 min Jaw-crusher, roll crusher, and milling	157 mAh/g (0.1 C) High CR (60 cycles)
[192]	LFP	$LiPO_3$, Fe_2O_3 , Fe^0 , carbon black	Melting 1000–1150 °C 3 h grinding, wet milling	156 mAh/g (0.1 C)
[193]	LFP	Li_2CO_3 , $FePO_4 \cdot 2 H_2O$, graphite	Melting 1000 °C 1 h Ball mill, up to 4 h	151 mAh/g (0.1 C) High CR (40 cycles)
[139]	LMFP	LiH_2PO_4 , Fe^0 , Fe_2O_3 , $MnCO_3$, methanol, glucose	Melting 1100 °C 10 min Ball mill 18 h Carbonization 700 °C 2 h	LFP: 158 mAh/g (0.05 C) High CR (50 cycles) $LM_{0.25}F_{0.75}P$: 145 mAh/g (0.05 C) 130 mAh/g (0.2 C) ~20 mAh/g fading (50 cycles)
[194]	LMFP	$LiPO_3$, Fe^0 , Fe_2O_3 , $MnCO_3$, carbon black	Melting 1000–1100 °C 1 h Manual grinding 3 h	$LM_{0.75}F_{0.25}P$: 142 mAh/g (0.1 C) $LM_{0.5}F_{0.5}P$: 146 mAh/g $LM_{0.25}F_{0.75}P$: 153 mAh/g High CR (70 cycles)

4.4. Comparison

Considering the best practices for synthesizing olivines, each process has advantages and disadvantages. SSS is inexpensive and simple, whereas hydrothermal LSS enables the tailoring of specific reaction conditions to optimize the synthesis parameters. The final LSS products have smaller dimensions than SSS products owing to the more precise control of the morphology and particle growth, resulting in enhanced D_{Li} and desirable electrochemical performance for batteries. The waste produced by hydrothermal processes affects the environment but can be addressed by applying zero-waste or green synthesis methods. Both SSS and LSS are time-consuming because they require two steps. Thus, one-step approaches are favorable. Hydrothermal LSS is interesting because of the opportunity to coat the product with carbon in a single step [169].

Similar to SSS, MSS benefits from low-cost precursors such as Li_2CO_3 , Fe^0 , and iron ore concentrate (such as Fe_2O_3) and can produce large batches via melt casting. In addition to its simplicity, MSS requires only several minutes to melt precursors at 1000 °C. Since all the initial materials are melted, MSS has no solid or liquid waste. However, grinding the prepared ingot into submicron or nanoscale powders is challenging [139]. In SSS or hydrothermal LSS, micro- or nanosized reactants increase the costs. In MSS, inexpensive, coarse Fe_2O_3 is used in an induction furnace [189]. MSS also benefits from a homogeneous molten composition with scale-up possibilities [195]. However, MSS must overcome challenges such as the use of high temperatures, achieving nanopowders, and alleviating a time-consuming carbonization step. Indeed, in all of the aforementioned processes, separate carbonization requires time and energy. Although this step is necessary to achieve a carbon coating and enhance the electronic conductivity, synthesis processes that can achieve in situ carbonization are highly desired.

5. Electrode engineering

In this section, we focus only on the binders and loading of the LFP

cathode materials in LIBs. As shown in Table 5 and summarized by Huang et al. [196], PVDF is widely used as a binder in NMP-based organic solvents. Other favorable binders include polyacrylic acid and PVDFHFP. PVDF is electrochemically stable in the 0–5 V range and is suitable for both anodes and cathodes. In addition, PVDF exhibits excellent cyclability in most active materials and acceptable adhesion to current collectors (Al and Cu). The high molecular weight of PVDF renders it suitable for viscosity-related processes. However, as a mature and widely used binder, PVDF has some drawbacks, including environmental toxicity, poor recyclability, and high price. PVDF, as a fluorinated polymer, reacts with lithium to form LiF, which eventually contributes to cell degradation and supplies additional heat (exothermic) to the reactions that may cause harmful thermal runaway. Because PVDF combines with the toxic and expensive NMP solvent in electrode fabrication, it is essential to develop cheaper green binders [197,198]. Solvent-free PTFE-based LFP cathodes exhibited an interesting DC of 142 mAh/g with 80% CR after 40 cycles, comparable to the values of 138 mAh/g and 87% of the cathode with PVDF in NMP. However, the solvent-free cathode exhibited a sharp decrease in capacity after 40 cycles [199].

Waterborne processes have been extensively developed recently. Waterborne binders include various compounds, such as carboxymethyl cellulose (CMC) [202,207], N-cyanoethyl polyethyleneimine (CN-PEI) [204], poly(3,4-ethylenedioxythiophene):polystyrene sulfonate/CMC (PEDOT:PSS/CMC) [205], sodium alginate (SA) [197], polytetrafluoroethylene (PTFE) [203], poly aspartic acid (PASP) [200], and fluorine/acrylate hybrid polymer (FAHP) [208]. Such materials are popular because of their safety, eco-friendliness, and low cost. Their composites have also attracted attention because of their multifunctionality, for example, CMC/PTFE [197]. Moreover, decorated functional groups in the polymer chains enhance the chemical bonding and adhesion of LFP particles via chemical modification [209]. Introducing or grafting functional groups on polymeric binders results in stronger adhesion and decreases the ACM volume [210].

Table 5

Summary of the various separators, electrolytes, conductive agents, binders, and solvents used in LFP-based cells. The best-reported results are presented here for each reference. * Fluoroethylene carbonate.

Ref.	Cell type	Separator	Electrolyte	Conductive agent	Binder	Solvent	DC mAh/g (rate)	CR% (cycles) (rate)
[197]	CR2016 coin	Celgard 2400	1 M LiPF ₆ in EC:DEC:DMC	AB (5%)	SA (10%)	Water	165 (0.1 C)	100 (50) (0.1 C)
					CMC:PTFE (10%)	Water	166 (0.1 C)	100 (50) (0.1 C)
					PVDF	NMP	156 (0.1 C)	100 (50) (0.1 C)
[200]	CR2025 coin	Celgard 2400	LP30 + 1% VC	Carbon grains (10%)	PASP (5%)	Water	152 (1 C) 122 (5 C)	100 (40) (1 C)
					PVDF	NMP	137 (1 C)	97 (40) (1 C)
[201]	Half-pouch	Celgard 2400	LP30	C65	SBR		134.7 (0.2 C)	96 (35) (0.2 C)
					4SBR:1CMC	Water	143.0 (0.2 C)	92 (35) (0.2 C)
[202]	CR2025 coin	NA	LP30	AB (10%)	CMC-Li (10%)	Water	183	97.6 (200)
					PVDF	NMP	148	87.8 (200)
[203]	CR2025 coin	Celgard 2400	LP30	AB (5%)	PTFE (5%)	Ethyl alcohol	161 (0.1 C) 124 (1 C)	97.5 (100) (0.1 C)
					PVDF (5%)	NMP	151(0.1 C) 118 (1 C)	95 (100) (0.1 C)
[204]	CR2025 coin	Celgard 2300	1 M LiPF ₆ in EC:DEC:DMC	AB (13%)	CN-PEI (7%)	Water	149 (0.1 C)	99.6 (100) (0.5 C)
					PVDF (7%)	NMP	148.7 (0.1 C)	97.3 (100) (0.5 C)
					PEI (7%)	Water	139 (0.1 C)	94.5 (100) (0.5 C)
[205]	CR2032 coin	Celgard 2325	LP30	Carbon black (4%)	PEDOT:PSS/CMC (4%)	Water	162 (0.2 C)	100 (100) (0.2 C)
				Carbon black (4%)	CMC (4%)	Water	158 (0.2 C)	100 (100) (0.2 C)
				Carbon black (8%)	PVDF (8%)	NMP	156 (0.2 C)	100 (100) (0.2 C)
[206]	CR2032 Coin	Whatman, GF/D	LP30	MWCNTs (3%)	Binder free	NMP (3%)	161 (0.5 C) 156 (1 C) 130 (5 C)	71.3 (500) (5 C)
[199]	CR2032 Coin	Celgard	1.2 M LiPF ₆ in 3EC:7EMC + 10 wt% FEC*	CNTs (5%)	PTFE	Solvent-free	142	80 (40) (0.1 C)
					PVDF	NMP	138 (0.1 C)	87.1 (40) (0.1 C)

The LFP electrodes with SA and CMC/PTFE exhibited outstanding electrochemical performance compared to that with PVDF and retained 100% capacity after 50 cycles with DC values of 165, 166, and 156 mAh/g, respectively (0.1 C) [197]. The PASP-assisted LFP electrode demonstrated excellent performance (152 mAh/g DC (1 C) with no capacity loss after 40 cycles). These electrodes showed more desirable electrochemical kinetics than the PVDF-assisted ones, with lower polarization. PASP fills the spaces between the LFP particles and provides full coverage, resulting in integral network conductivity and a short Li diffusion path. Moreover, the carboxyl/imide functional groups in the PASP chain assist with Li^+ transfer [200]. LFP water-based slurries were prepared using a combined binder of styrene-butadiene rubber and CMC as a thickener (4:1). Half-pouch cell exhibited 143 mAh/g DC (0.2 C) and 92% CR (35 cycles), whereas full-pouch cell showed 98% CR (55 cycles) [201]. Another study using CMC-Li also confirmed its usefulness as a waterborne binder in an LFP-based cathode with 176 mAh/g DC and 98% CR (200 cycles) compared to PVDF with 148 mAh/g DC and 88% CR (200 cycles) [202]. The PTFE-based LFP cathode showed a DC of 161 mAh/g versus 151 mAh/g for a PVDF-based cathode, with enhanced electronic conductivity and reduced charge-transfer resistance [203]. The DC of a CN-PEI-based LFP cathode was similar to those of a PVDF-based counterpart, 149 and 148.7 mAh/g, respectively, while the CR after 100 cycles was ~2% higher for the former, 99.6% versus 97.3%, respectively. The use of PEI resulted in poorer performance: 139 mAh/g DC and 94% CR per 100 cycles [204]. Additional comparisons are presented in Table 5. Notably, conductive binders facilitate the fabrication of electrodes without conductive additives, enabling a higher percentage of active material and higher energy density [210]. In contrast, binder-free cathodes are highly favored because a higher active-material content results in a higher energy density. A binder-free LFP cathode prepared using multiwalled carbon nanotubes dispersed in NMP showed acceptable DC values of 161 (0.5 C), 156 (1 C), and 130 (5 C) mAh/g with 71% CR after 500 cycles (5 C) [206].

The particle size and mass loading of LFP are highly significant in the design of high-power and high-energy electrodes for LIBs. The effect of these parameters on the LFP characteristics was investigated using two different particle sizes (0.88 and 0.26 μm) and three loadings (1.59, 3.17, and 6.35 mg/cm^2) [211]. Specific capacities increased with LFP loading. When the positive electrode loading was 5.74–6.23 mg/cm^2 , the areal specific capacities and capacity for positive electrodes were 0.98–1.06 mAh/cm^2 and 1.38–1.50 mAh, respectively. These ranges are attributed to the coin cells and three-electrode cells (3E), denoted as CRNP09, CRNP10, CRNP12, 3ENP09, 3ENP10, and 3ENP12 based on the cell types [212].

6. Design and optimization of electrolytes

As a critical component, electrolytes affect the electrochemical performance, safety, and stability of a battery. The polarity of an LIB electrolyte must be sufficiently high to cause salt dissociation while remaining electrochemically inert over a broad potential range of 0–5 V vs. Li/Li^+ . A few aprotic organic chemistry classifications satisfy these requirements [213]. Lithium salts, organic solvents, and functional additives are the main ingredients in the liquid electrolytes of LIBs. Meeting these requirements facilitates the formation of a stable passive layer with limited expansion, high ionic conductivity, and low flammability. None of the current electrolytes satisfy all of these requirements [214]. Amorphous $\text{LiFePO}_4(\text{OH})$ is formed on the LFP cathode surface owing to corrosion and the formation of Fe (III). The abundant hydroxyl groups on the surface react further with LiPF_6 , resulting in iron dissolution and electrolyte decomposition [215].

The electrolytes employed in LIBs consist of diverse types, ranging from organic liquid electrolytes such as ethylene carbonate (EC) to ionic liquid electrolytes, aqueous liquid electrolytes (where water serves as the solvent), inorganic solid electrolytes (ceramic materials), polymer solid electrolytes, and composite electrolytes (comprising ionic liquid

and liquid organic components)[216]. The electrolyte of commercial LIBs exclusively contains 1 M LiPF_6 in different solvent ratios of linear carbonates such as EC, DMC, DEC, methyl ethyl carbonate (MEC), and propylene carbonate (PC) [217,218]. Furthermore, 1 M LiPF_6 in EC:DMC or EC:DEC, mostly 1:1 EC:DMC (LP30), has prevailed as the predominant electrolyte in LIBs based on a 3–4 V cathode and graphite anode (Table 5). This salt provides satisfactory high passivation and ionic conductivity and works in a broad temperature range. However, LiPF_6 is thermally and chemically unstable and deteriorates the anode performance. Moreover, trace amounts of water or alcohol in carbonate solvents react with LiPF_6 to yield HF, which may enhance the corrosion of the cathode [217]. LiBF_4 and its blended salts, such as lithium difluoro (oxalate)borate (LiDFOB), have been introduced as promising alternatives for high-voltage LIBs [219,220].

LiODFB , lithium bis(oxalate)borate (LIBOB), and tris(2,2,2-trifluoroethyl)phosphate added to LiPF_6 resulted in a high CR and promoted solid electrolyte interphase formation [221,222]. Adding LiF to the electrolyte accelerated ion surface diffusion and led to smooth electrodeposition. Additionally, forming a protective layer prevents side reactions and electrolyte degradation. Consequently, LiF effectively improves the capacity and lifetime of a LIB [223], but it does not exhibit excellent solubility in organic electrolytes. Hence, the formation of a homogeneous layer is challenging. In addition, handling HF for LiF formation poses safety issues [224]. Generally, additives oxidize more than solvents during cycling, forming a passivation layer on the cathode surface, stabilizing the electrode/electrolyte interface, and inhibiting electrolyte oxidation [225]. Furthermore, an analysis was conducted on the electrochemical performance concerning the current rate, fluoroethylene carbonate (FEC), and vinylene carbonate (VC) concentrations in the electrolyte. Therefore, a notably higher amount of additives, up to 20 vol%, was required to maintain good performance. Impedance spectroscopy revealed that adding large amounts of FEC/VC did not significantly affect the electrolyte's ion conductivity. Based on silicon mass, the capacity was computed to be 3000 mAh/g. Consequently, the specific capacity rapidly decreased to 20% of its initial value or 244 mAh/g electrode. Crucially, within the range of 10 vol% and 20 vol%, the reversibility was independent of the FEC concentration. The reversibility was further enhanced and surpassed both FEC concentrations in the electrolyte with the addition of VC. However, high current rates significantly reduced the capacity in the case of VC addition, in contrast to the additive-free electrolyte containing FEC [226].

Commercial LIBs use liquid organic electrolytes despite their safety issues related to their extreme flammability. Solid polymer, gel polymer, and quasi-solid electrolytes have been proposed as promising alternatives. PVDF-based gel polymer electrolytes have been used in LIBs. The weak adhesion of solid electrolytes to electrodes must be addressed. Hybrid electrolytes have also been proposed as feasible approaches [227]. Efforts have been made to replace the separator/electrolyte combination with a polymer/liquid with advanced liquid and semi-solid components by 2030, followed by further drying to achieve fully solid-state structures [6].

7. Cells, modules, packs, and chassis

Coin cells are the most common structure used in battery studies because of their easy preparation, simple configuration, and low cost owing to using small quantities of materials. However, single- and multilayer (few layers; <3 Ah) pouch cells have also been studied in advanced LIB research and development because they are closer to the commercial cell format [228]. The battery-making chain comprises four significant steps: cell preparation, module fabrication, packing, and chassis assembly (Fig. 13). The cells are composed of sheet-like anode and cathode electrodes that are physically divided by separators in curled (cylindrical) or sandwich (pouch or prismatic) geometries. Lithium ions are shuttled internally from one layer to another using a filling electrolyte [46]. The modules are clusters of cells with attached



Fig. 13. EV battery production steps: (1) conventional cell, module, pack, and chassis route for NMC and NCA chemistries versus (2) cell-to-chassis design for large format LFP cells. Reproduced with permission from [231].

terminals arranged in each case. The cell number per module depends on the cell type and manufacturer; the Automotive Energy Supply Corporation clusters four cells on a module for the packs used in the Nissan Leaf EV. The Samsung Digital Interface uses twelve cells per module. Each pack consists of modules, cooling equipment, and electrical connections. The chassis assembly is the final step of battery production [229,230].

As previously mentioned, standard modular packs are designed in a box-in-a-box arrangement, with the cells in modules and modules in packs (path 1 in Fig. 13). This typical arrangement requires pack spacers, connections, and wiring. In comparison, cell-to-pack (CTP) design enhances the battery pack's volume utilization rate by 15–20% [232]. Tesla's CTP design maximizes space for the active materials [233]. Eliminating the module and pack by introducing a cell-to-chassis design creates an opportunity to integrate cells into the chassis directly (path 2 in Fig. 13). This design significantly increases the energy density of the battery [234,235]. Tesla announced the adoption of the cell-to-chassis design in 2020, with a plan to commence series production at the beginning of 2025 using Panasonic cylindrical-shaped cells in the chassis. This design was later adopted by VW and GM [236,237]. The cell-to-chassis design could enable EVs to extend their range to over 800 km. Integrating the cells into the EV chassis could reduce the volume by up to 40% compared to current commercial designs [237].

BYD patented a cell-to-chassis design in 2019 as large-format blade-shape cells [238]. BYD switched to LFP in all passenger EVs with the aid of blade technology to address the concerns over the cost and supply chain. Although this chemistry induced other issues with its low energy density, innovative designs improved it while benefiting from its low cost [239]. This design focuses on maximum durability, extended range, and lifespan and features an ultra-strong structure. The longer and flatter design not only enhances safety but also optimizes space utilization within the battery pack. LFP chemistry was employed in this typical design. It provides superior safety to traditional counterparts, thanks to its inherent excellent thermal stability. The blade battery has surpassed the Nail Penetration Test, the most rigorous assessment for battery thermal runaway in simulated severe traffic accidents. Withstanding extreme conditions, including crushing, bending, and overheating, it demonstrated exceptional safety by avoiding fires or explosions, positioning it as a safety leader in the growing electric vehicle market [240]. The impressive thermal stability of LFP is evident as it exhibits excellent performance without exothermic reactions up to 400 °C [241]. However, this large format design (path 2 in Fig. 13) is not suggested for NMC/NCA chemistries. Analyzing these chemistries' heat generation and thermal behavior in large-format batteries revealed that larger cells accompanied by higher charge/discharge currents undesirably increase cell temperatures. The primary description of this heat

generation can be defined by the voltage difference attributed to the charge and discharge during operation due to overpotentials and hysteresis of open-circuit voltage. As a consequence, energy inefficiency causes strong waste heat generation. The calorimetric measurements revealed that this heat measured more than double for Li- and Mn-rich NMC than NCA cathodes, even four times more during discharge [242].

Cells are appealing for worldwide trade because they are more easily transported and have lower shipping costs than battery packs [229]. Cell manufacturing is ranked second in terms of the possible economic impact on the supply chain after EV assembly [1]. Module and pack assembly costs are 11% and 14% of the total expenses of a finished LIB pack, respectively. Subsequently, because transportation of small cells is more accessible, module manufacturing and pack assembly are usually conducted at the same site as EV production. The Nissan Leaf cells, modules, and packs were prepared in Sunderland, England. Tesla's modules and packs are produced in a Gigafactory in Nevada or its assembly unit in Fremont, California. Tesla Model 3 uses gigafactory cells, and models S and X use Panasonic cells [229].

According to Argonne National Laboratory, the cells account for 75% of the cost of a battery pack on average. Cell producers list different specifications and components for their battery cell assemblies; however, their general requirements are similar. Tesla uses cylindrical small-format Panasonic 18650, 2170, and 4680 NMC cells (similar to laptop batteries) to reduce cost, while other vehicle manufacturers have worked with suppliers to create giant prismatic automotive-grade battery cells to reduce complexity and increase reliability [229].

Table 6 summarizes the EV models that currently use or will use LFP-based batteries. Tesla championed the use of LFP battery technology, which is dominated by Chinese suppliers. LFP-chemistry cells are produced in prismatic or cylindrical formats. The cells are arranged in four modules, similar to the 2170 cylindrical cells in Tesla Model 3 and Model Y. LFP are used chiefly in standard-range cars because they offer a lower energy density than NCA or NCM [243]. However, Tesla plans to expand LFP use in its "Semi Light" electric trucks. Therefore, most short-range semi-heavy lifting trucks for electrification employ iron-based batteries [244]. In the long-range versions, energy-dense counterparts in cylindrical form are used [243].

Ford announced it will introduce LFP batteries with prismatic shapes for the Mustang Mach-E this year and the F-150 Lightning in 2024. The reported energy capacity of 78 kWh is quite interesting, considering that LFP has 65% of the energy density of NCM. The Mach-E pack will contain 108 of China's Contemporary Amperex Technology Co. (CATL)-produced cells (225 Ah size) in series, similar to the current packs. Ford aims to have its own automaker-backed LFP plant with a \$3.5 billion investment in BlueOval Battery Park, Michigan, USA opening in 2026 [249,255].

Table 6
Current and upcoming EV models using LFP-based batteries and the corresponding characteristics (limited to those appearing in the automaker's reports).

Ref.	EVs	Brand/Model	Status	Battery type	Range (km)	Energy consumption (kWh/km)	Battery size (kWh)	Fast charging	LFP battery plant	EV assembly location
[240,245]		BYD/ ATTO 3	Current model	Blade-LFP	420	0.16	60.4	40 mins (SOC=10–80%) 29 mins (SOC=30–80%)	CATL* China	China
[240,245]		BYD/ TANG	Current model	Blade-LFP	400	0.18	86.4	30 mins (SOC=30–80%)	CATL China	China
[240,245]		BYD/ HAN	Current model	Blade-LFP	521	–	85.4	48 mins (SOC=10–80%) 30 mins (SOC=30–80%)	CATL China	China
[243, 246–248]		Tesla/ Semi Light	Upcoming model in 2023	Prismatic-LFP	500	–	500	30 mins (SOC=10–80%)	Tesla's Gigafactory in Nevada	Tesla's Gigafactory in Nevada
[246]		Tesla/ Model 3	Current model	Cylindrical-LFP	507	0.14	75	–	CATL China	Tesla's Gigafactories in the US and China
[246]		Tesla/ Model Y	Upcoming model	Cylindrical-LFP	–	–	75	–	CATL China	Tesla's Gigafactories in the US and China
[249,250]		Ford/ Mustang Mach-E	Upcoming model in 2023	Prismatic-LFP	up to 600	–	78	–	CATL, in 2026: BlueOval Battery Park Michigan, US	Cuautitlán Stamping and Assembly Plant, Mexico
[249,250]		Ford/ F-150	Current model	Prismatic-LFP	up to 515	0.28–0.36	98–131	–	CATL, in 2026: BlueOval Battery Park Michigan, US	Dearborn Truck Plant, Michigan, US
[251]		Toyota/ Aqua and Crown	Upcoming in 2026	Prismatic/New structure-LFP	1000	–	–	20 mins (SOC=10–80%)	CATL China	Japan
[252,253]		Hyundai/ Kia- Gen. 2 Ray minivan	Upcoming in 2023	LFP	205–233	–	35.2	40 mins (SOC=10–80%)	CATL China	Seosan Plant, South Korea
[254]		Mercedes-Benz/CLA	Upcoming in 2025	LFP	750	0.12	–	–	CATL China	Germany

While all EV manufacturers work on conventional cylindrical, prismatic, or pouch cells, BYD announced a revolutionary blade type. BYD claims that the blade battery achieves superior performance owing to the enhanced space utilization of the module-free pack with a longer and flatter design. The battery also exhibits impressive safety and durability using LFP as the ACM, with superior thermal stability [240]. Tesla also tested BYD blade-shaped LFP batteries in its Model Y RWD in Giga-factory Berlin, and the results showed an exceptional charging speed compared to the CATL version. The BYD variant maintained fast charging at 172 kWh to reach 50% charge, and then the rate dropped until the battery reached 90% charge. The CATL pack failed to maintain a fast-charging speed of 172 kWh, and the speed dropped immediately. Nevertheless, Tesla continues to use batteries from its previous provider [256]. Tesla is currently aiming for a battery pack of ~110 kWh with a range of 400 miles (644 km) [257].

Toyota announced that next-generation LFP-based batteries will be employed in Aqua and Crown hybrid vehicles, which are expected to be released in 2026–2027. The cells will have a new structure for the standard version aiming to increase the cruising range by 20%, reduce costs by 40%, and achieve a 30-min quick recharge (state of charge =10–80%) compared to the current bZ4X technology [251].

Interestingly, up to September 2022, over 85% of the utilized LFP (in any cell format) in newly-sold passenger EVs was fabricated in China. Notably, 68% of this was used by two large EV manufacturers, Tesla and BYD, while the rest was used by other EV manufacturers (SGMW, MG, GAC, and Geely). LFP share of the total alternative chemistries used in EV batteries increased from 17% in January 2021–26% in January 2022–31% in September 2022 and is expected to hover between 25–35%. However, the portion will sharply increase if Chinese automakers (that currently sell their products only in China) export their LFP-deployed EVs to Europe and/or their European counterparts such as VW and Stellantis and North American manufacturers like Ford and Rivian practically use LFP [258].

A direct relation between the driving range and the battery size of EVs is reported [259]. So, various groups of mini cars, medium cars, large cars, and luxury cars with battery capacities of 17.7, 24.4, 42.1, and 59.9 have related driving ranges of 133, 171, 249, and 317 km with energy consumption of 0.146, 0.17, 0.185, and 0.207 kWh/km, respectively. These numbers are much higher in electric buses, mainly depending on the bus service type, with battery size of 320–680 kWh and energy consumption of 2–4.6 kWh/km [260]. Nevertheless, comparing alternative EV models from various manufacturers or even one single manufacturer, no specific relation can be seen between battery capacity and driving range (Table 6). Models and data provided in this table are obtained from the manufacturer's websites.

8. Major challenges for LIBs

8.1. Safety

The safety of LIBs is one of the main challenges in the large-scale development of EVs. Fire, smoke, and explosions often occur in battery systems because of thermal runaway due to flammable materials, resulting in safety hazards [261]. However, LFP-based LIBs are the most safe, followed by those using NMC, NCA, and LCO (the most volatile chemistry) [262,263]. From 2011–2021, 32 explosions in NMC battery cells were reported, leading manufacturers to adopt LFP batteries as safer alternatives in terms of thermal runaway. Nevertheless, an explosion occurred in LFP cells in 2021 in Beijing, causing the death of firefighters [264]. The CTIF International Association of Fire Services investigated this accident and attributed it to thermal failure of the battery under extreme conditions caused by internal/external sources [265]. The primary appearance of LFP thermal runaway is the gas release from the safety valve. Although individual LFP cells passed the thermal runaway tests, battery packs in actual applications may not. Differences in testing conditions must be considered. In practice, many

battery cells are packed tightly. Hence, the vented gases accumulate inside the pack and cannot escape in a timely manner. A high content of combustible gases exceeding the lower flammability or explosive limits can result in explosion [264]. Battery safety tests can estimate potential threats and minimize them. There are three main categories of abuse: electrical, mechanical, and thermal. The latter corresponds to the most challenging issues due to thermal runaway. Electrical abuse tests included overcharging, forced discharge, and external short circuits. Mechanical abuse tests included nail penetration, collision, and crushing. Finally, thermal abuse tests include thermal and local heating tests. Internal short circuits are considered a fourth category of safety tests [266].

8.2. Cost

LIB pack prices have continuously decreased since 2010, and Bloomberg New Energy Finance began monitoring the trend from \$732/kWh in 2013 (\$502/kWh for cells and \$230/kWh for pack) to \$151/kWh in 2022 (\$120/kWh for cell and \$31/kWh for packs) [267]. The DOE estimated an 89% decline in the battery pack cost over 2008–2022 (\$1355/kWh in 2008). This price drop is attributed to technological improvements, new chemistries, and higher manufacturing volumes [268]. Only one rise in cost was observed in 2022, with a 7% increase compared to the previous year because of inflation and the rising prices of raw materials and battery components [54]. The market anticipates a price drop below \$100/kWh for the whole pack in 2024 because of additional extraction and refining capacities coming online [269]. Furthermore, the pack cost is estimated to reach ~70 \$/kWh by 2050 [270]. China outperforms the rest of the world with the cheapest LIB pack (\$127/kWh), while the prices in the USA and Europe are 24% and 33% higher, respectively, owing to higher manufacturing expenses, a broad range of applications, and battery imports [267].

The cost of LFP cells was ~20% less than NMC cells in 2022. Nevertheless, LFP packs were 27% higher in 2022 than in 2021, primarily based on the unstable price of Li resources [267]. The increasing demand for Li and its supply deficit starting from May 2021 resulted in a 600% increase in LiOH and 570% increase in Li₂CO₃ prices. These additional costs sharply increased ACM-related costs [271]. A steep surge in the price of other raw materials has amplified the difference in the total cost of Ni-based ACMs and their LFP-based counterparts, driving interest in the latter. Cobalt accounted for almost a quarter of the battery cost [272], increasing to \$88/kg in 2018 and returning to \$55/kg in 2021. Nickel, the next most expensive ingredient, was only \$19.8/kg in 2021 [273], reaching \$27.06/kg in 2023, and it is expected to remain stable in 2024 [274]. Because of the high price and volatility of Co, a shift toward low-Co or Co-free chemistry is desired. LG Energy Solution supplies 90%Ni-containing cathodes for Tesla batteries [275]. Nevertheless, owing to the high price and increasing demand for Ni, LFP as a replacement has been increasingly considered.

In startups and research centers, sodium-ion batteries have been developed using sodium chloride to overcome resource shortages and reduce battery costs. The costs are much lower without expensive Li, Co, or Ni ingredients [276]. Future pricing projections may change owing to further technical developments in mining and refining, EV production, and battery chemistry [277]. As the EV industry is rapidly expanding, accurate forecasting is impossible.

8.3. Energy efficiency

Despite the long lifespan and superior safety of LFP materials, the challenge of their low gravimetric energy density remained unsolved. The downside of the lower power and energy densities of LFP compared to other chemistries in LIBs is a notably lower voltage plateau, which requires more LFP-based cells per pack to provide the same energy density as other LIB counterparts. State-of-the-art LFP-based cells have shown a specific energy of approximately 180 Wh/kg compared with

250 Wh/kg for NMC- or NCA-based cells [278,279]. Since the popularity of LFP is increasing, this issue must be addressed. When Tesla announced the utilization of LFP in its Model 3 EV for the first time in April 2020, CTP was proposed as a new design concept to compensate for the energy-density limitations [233]. The CTP design narrows the energy-density gap with the aid of pack-level design. For instance, in BYD's blade-shaped battery, single cells are aligned in the pack (600–2500 mm length), leading to an integration efficiency that is 40% higher than that of custom cell-module-pack designs. Notably, in most EVs, the gravimetric cell-to-pack ratio (GCTP), which refers to the specific energy ratio of the pack to the cell, is measured as 0.55–0.65. This ratio means that 35–45% of the pack weight is involved by inactive elements like thermal and battery management systems, cases, cables, and so on. Furthermore, the typical volumetric cell-to-pack ratio (VCTP) is approximately 0.4. Innovation in CTP technology included removing module-related parts and utilizing the blade battery (such as the BYD Han EV), achieving outstanding ratios of 0.85 for GCTP and 0.62 for VCTP [278]. In general, the VCTP and GCTP metrics are increasing. The volumetric energy density of LIB packs has increased eight-fold from 55 Wh/L in 2008–450 Wh/L in 2020 [280].

Although LFP materials have been significantly used in the LIB industry over the past few years, specifically in the automobile sector (Table 6), EVs require batteries with higher energy densities to satisfy the demands for longer driving ranges and standby times. The goal is to increase the gravimetric energy density to 500 Wh/kg and volumetric energy density to 800 Wh/L by 2030 for LIBs, corresponding to a 60% increase compared to current LIB cells [281,282]. Governments globally actively support the advancement of battery technologies for improved performance, affordability, and safety. Initiatives such as the US DOE's "Battery 500" consortium and the "New Energy and Industrial Technology Development Organization" (NEDO) of Japan based on "Research and Development Initiative for Scientific Innovation of New Generation Battery" (RISING II) project aimed for energy densities of 500 Wh/kg by 2021 and 2030, respectively. In China, the CAS and government projects like "Made in China 2025" target gradual increases in energy density, reaching 400 Wh/kg by 2025. Mass production of Li-ion cells with an energy density of 240 Wh/kg has been achieved, while those aiming for 300 Wh/kg or even 400 Wh/kg are currently in the developmental stage. As a result, additional research is required to meet the targets for driving range (>500 km), charging time (<20 min), and cycle life (>3000 cycles) for electric vehicles powered by lithium-ion batteries [283].

A theoretical investigation of the effect of the design parameters on the optimization of the energy density of LIBs was performed [284]. An LFP half-cell model analysis revealed that the electrode thickness, cross-sectional area, and LFP particle size are the most significant parameters. To reach 250 Wh/kg energy density, an LFP electrode with the following parameters is needed: 310 μm thickness, 2×10^{-4} m² cross-sectional area, and 10 nm LFP particle size. A 61 Wh/kg increase in the energy density was estimated for the proposed design. In another study [285], the optimization of the LIB design factors to achieve maximum energy density was performed using a quadratic response surface model and experimental design. A 56.8% increase in the energy density was calculated, and the electrode thickness ratio, the active material ratio, and porosity were revealed as significant factors in this increment.

Instead of optimizing the design, applying alternative chemistries, such as LMP, is more promising for addressing energy-efficiency issues. LMP offers an almost 0.4 V higher potential than LFP and a higher specific energy. Compared with LMP, LMFP overcomes both the low conductivity of LMP and the low voltage and energy density of LFP [272]. At the cell level, a 15% higher energy density was calculated for LMFP, i.e., 210 Wh/kg for LMFP compared to 175 Wh/kg for LFP (2022 data) [286]. The high energy density of LMFP (210 Wh/kg) in M3P batteries enables EVs (e.g., Tesla Model 3) to reach a range of up to 700 km with a size similar to that of the existing LFP battery pack

currently supplied by CATL for Tesla [287]. LCP, LNCP, and LMFCP have also been developed for battery applications. Despite these promising results, further practical improvements are required to overcome the formation of an unstable cathode–electrolyte interphase layer during battery operation [288].

Despite these improved energy density results, enormous practical efforts based on experimental trial-and-error, mainly by industrial partners, must be performed to optimize the battery design of LFP-based LIBs. In addition to these efforts to increase the energy density of the cathodes, improving other components of LIBs has been considerably effective [281]. Examples include the anode chemistry, particle size, thickness, and porosity, as well as the separator thickness and porosity [285]. Utilizing safer, low-cost, and low-density LFP and LMFP materials with these modifications is promising.

Overall, the attractiveness of LFP batteries in terms of cost, safety, and lifetime overcomes the disadvantages of low energy density and peak power (Fig. 14). As shown in Fig. 14, some modifications in the battery system can enhance the application characteristics compared to the traditional NMC chemistry and make those closer to the targets. A thermally modulated LFP designed for operating at elevated temperatures of about 60 °C can overcome the energy density challenge. Operating at 60 °C not only addresses the challenges related to low temperatures in LFP chemistry but also significantly enhances kinetic and transport properties. This results in rapid 10-minute charging and impressive power performance in diverse climates [278]. Therefore, LFP batteries are quickly replacing other alternatives in the EV market. With new designs, chemistry, and thermal and chemical stability modifications, LFPs are dominating the global battery market.

8.4. Carbon emissions

Another issue with EVs is their environmental impact. Despite the availability of clean electricity from zero-emission EVs, battery production is a massive, carbon-intensive process. Because the large LIBs required to power EVs account for approximately 40% of the emissions of the total EV production [291], manufacturers are moving quickly to address this issue. In particular, there is growing pressure for global

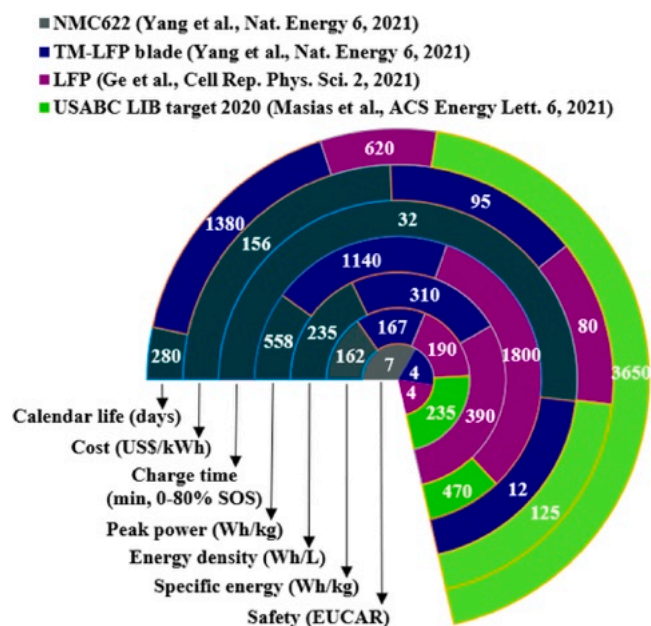


Fig. 14. LIB characteristics for NMC622 [278] and newly reported LFPs [289], including a thermally modulated one (TM-LFP) [278], based on the LIB targets adopted by the United States Advanced Battery Consortium (USABC) and European Council for Automotive R&D (EUCAR) [290]. Data was drawn with permission from the mentioned literature in the caption.

decarbonization, and brands are racing to address the emissions challenge. This issue is highlighted by the fact that the GHG emission in EV production is estimated to be 30% [292] to 50% [293] higher than that of an internal combustion engine vehicle. The production of a battery pack alone for a typical EV (75 kWh) emits more than seven tons of CO_{2eq} [293]. Another report estimated that the GHG emissions for producing three commonly used LIBs (28 kWh size) utilizing LFP, NMC, and LMO in China are 3061, 2912, and 2705 kgCO_{2eq}, respectively

[292]. In comparison, another study mentioned that LFP batteries have a lower environmental impact in production than NMC batteries, while they show a higher environmental burden in use and transportation. Specifically, LFP batteries emit about 42–44.5% less carbon than NMC batteries, with lower water and ecological footprints [294].

Nevertheless, because one-third of the CO₂ emissions in the world are caused by transportation (based on the 2019 IEA report [295]), it is important to move toward the electrification of transportation. Based on

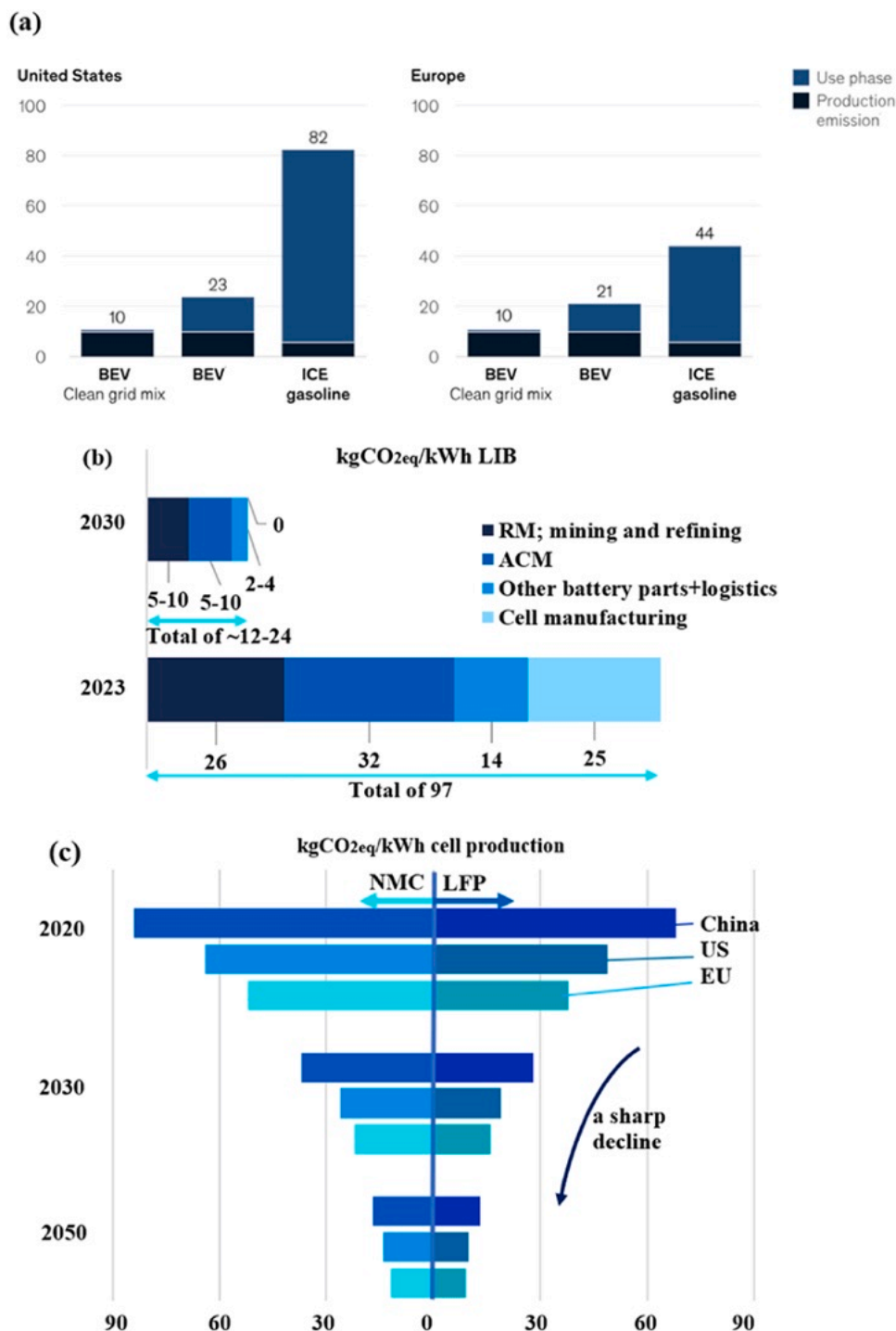


Fig. 15. (a) Emission by vehicle type (metric ton CO_{2eq}). Use phase: estimated as 243,000 km; production emission: refers to average vehicle c-segment; BEV: battery electric vehicle. (b) GHG emissions (kg CO_{2eq}/kWh) from LIB production steps. (c) GHG emissions (kg CO_{2eq}/kWh) from cell production with different chemistries in various regions. Emissions for NMC chemistries, i.e., NMC111, NMC523, NMC622, NMC811, and NMC955, as well as LFP, are reported in the same range with slight differences, with a documented average ± 3 kg CO_{2eq}/kWh.

(a) With permission from [301]. (b) Data was drawn with permission from [293,299]. (c) Data was drawn with permission from [299].

the 2023 IEA report for the emissions from the transportation sector in 2000–2030 [296], compared to the 8 Gt of CO₂ released in 2021, emissions increased by over 250 Mt CO₂ (3%) in 2022. To achieve the net zero scenario, transportation emissions must drop by almost 25%, reaching 6 Gt by 2030. This decrease depends significantly on a quick-return solution, such as the rapid electrification of road vehicles with high energy efficiency. Although this transformation has commenced in light vehicles, it must continue in heavy-duty vehicles because the electrification progress of this segment is slow. Such vehicles, including trucks and buses, are responsible for almost 46% of GHG emissions in the transportation sector [297].

As shown in Fig. 15(a), much of the carbon originates from the mining and refining raw materials. The production of active materials (anode and cathode) is also considered a significant source of emissions. For a precise LCA, the entire cycle, including raw material extraction, manufacturing and operation, distribution, use, recycling, and disposal, determines the cost and embedded carbon emissions. The entire chain depends on the battery chemistry, production technology, and suppliers [298]. A significant share of renewable energy can reduce carbon emissions [299]. McKinsey [293] compared the carbon emissions in the production and use phase of EVs and internal combustion engines (ICEs) (Fig. 15a). The differences arise from the power source and emissions during an ICE's life. It is clear that although the production emission for EVs is almost double that of an ICE vehicle, the emissions during use for ICEs are far beyond those of EVs. The difference is much larger when clean grid electricity is used, with almost zero emissions in the use phase of EVs [6]. Fig. 15(b) shows the emissions per LIB's production step. It is forecasted that the reported 97 kg CO_{2eq}/kWh for all production steps will reduce to 12–24 kg CO_{2eq}/kWh by 2030 due to improvements in cell manufacturing [293]. In another research using a prospective LCA model, it was predicted that GHG emissions per kWh of LIB cell production could be reduced from 41–89 kg CO_{2eq} in 2020–10–45 kg CO_{2eq} in 2050, with the main contribution being low-carbon green electricity (Fig. 15c) [300]. Such mismatches in the emissions predicted by different LCAs might be due to the inherent characteristics of long-lived products, such as batteries. This effect was discussed previously in terms of future scenarios, such as recycling or electricity supply, and the authors highlighted the necessity of integrated assessment [300]. Currently, energy, mainly electricity, plays a significant role in LCA because 40% of the emissions are associated with energy use, affecting the equations used in the analysis. For instance, China produces more than twice the GHG than the USA because of non-renewable resources, mainly no available hydroelectricity [292] and only 5% renewables. Canada is ranked first in renewable resource utilization (65% renewables), corresponding to the lowest CO₂ emissions (132 gCO₂/kWh). LFP overtaking other conventional chemistries also affects forecasts [291].

9. Summary

To address the gap in the knowledge of a review of the manufacturing process from mining to chassis, we attempted to cover all of the aspects necessary for LFP/LMFP-based LIB production for EVs, including the mining, raw materials, ACM, and cell-to-chassis strategy. This review of the entire process provides an overall perspective for readers working in fields where knowledge of the resources and potential reserves for each battery element and the related mining processes is vital. It is also essential to understand the applicable raw materials for LFP and their synthesis routes for low-cost battery-grade LFP. In addition to academic concepts, we also discussed the industrial aspects of LFP-based LIBs, such as the market, commercialization progress, and existing challenges. This article provides an overview of LFP and LIBs worldwide. As the most promising chemistry, LMFP is expected to fit within the future direction of batteries, such as novel solid-state battery systems. This chemistry will open new applications by cell to chassis design in heavy trucks and Semi-trailers. To overcome current challenges, researchers in this field could introduce new

developments, such as optimized raw materials and green synthesis approaches.

CRedit authorship contribution statement

Anil Kumar Madikere Raghunatha Reddy: Writing – review & editing. **Xia Li:** Writing – review & editing, Conceptualization. **Atiyeh Nekahi:** Writing – review & editing, Writing – original draft, Visualization, Software, Formal analysis, Data curation, Conceptualization. **Karim Zaghib:** Writing – review & editing, Validation, Supervision, Investigation, Conceptualization. **Sixu Deng:** Writing – review & editing.

Declaration of Competing Interest

The authors declare the following financial interests/personal relationships which may be considered as potential competing interests: Professor Karim Zaghib reports financial support was provided by Concordia University. If there are other authors, they declare that they have no known competing financial interests or personal relationships that could have appeared to influence the work reported in this paper.

Data Availability

Data will be made available on request.

Acknowledgments

We extend our deepest gratitude to AI-Mogul and Innove for their generous support, which was instrumental in realizing this work. We would also like to express our special thanks to Madam Sarah Sajedi, whose significant contributions to the graphic design elements of the project were invaluable and greatly enhanced the quality of our presentation.

Appendix A. Supporting information

Supplementary data associated with this article can be found in the online version at doi:10.1016/j.msar.2024.100797.

References

- [1] Canada's New Economic Engine, Modelling Canada's Ev Battery Supply Chain Potential—and How Best to Seize It, Clean Energy Canada and Trillium, 2022. (https://cleanenergycanada.org/wp-content/uploads/2022/09/Canada-sNewEconomicEngine_Web.pdf).
- [2] Canada's energy future 2023: Energy Supply and Demand Projections To 2050, Canada Energy Regulator, 2023. (<https://www.cer-rec.gc.ca/en/data-analysis/canada-energy-future/2023/canada-energy-futures-2023.pdf>).
- [3] National blueprint for lithium batteries 2021–2030, Federal Consortium for Advanced Batteries, The US Department of Energy (DOE), 2021. (https://www.energy.gov/sites/default/files/2021-06/FCAB%20National%20Blueprint%20Lithium%20Batteries%200621_0.pdf).
- [4] The Paris Agreement, Climate Action, United Nations, 2015. (<https://www.un.org/en/climatechange/paris-agreement>).
- [5] Fact sheet: Biden-Harris Administration Driving U.S. Battery Manufacturing and Good-paying Jobs, The White House, 2022. (<https://www.whitehouse.gov/briefing-room/statements-releases/2022/10/19/fact-sheet-biden-harris-administration-driving-u-s-battery-manufacturing-and-good-paying-jobs/>).
- [6] D.I. Mikael Hanicke, Sören Jautelat, Martin Linder, Patrick Schaufuss, Lukas Torscht, Alexandre van de Rijt. Battery 2030: Resilient, Sustainable, and Circular, McKinsey, 2019.
- [7] A.K. Padhi, K.S. Nanjundaswamy, J.B. Goodenough, Phospho-olivines as positive-electrode materials for rechargeable lithium batteries, *J. Electrochem. Soc.* 144 (1997) 1188, <https://doi.org/10.1149/1.1837571>.
- [8] S. Link, C. Neef, T. Wicke, Trends in automotive battery cell design: a statistical analysis of empirical data, *Batteries* 9 (2023), <https://doi.org/10.3390/batteries9050261>.
- [9] N. Fallah, C. Fitzpatrick, Is shifting from Li-ion NMC to LFP in EVs beneficial for second-life storages in electricity markets? *J. Energy Storage* 68 (2023) 107740 <https://doi.org/10.1016/j.est.2023.107740>.
- [10] C.S. Ioakimidis, A. Murillo-Marrodán, A. Bagheri, D. Thomas, K.N. Genikomsakis, Life cycle Assessment of a lithium iron phosphate (LFP) electric vehicle battery in

- second life application scenarios, *Sustainability* 11 (2019), <https://doi.org/10.3390/su11092527>.
- [11] P. Hovington, M. Lagacé, A. Guerfi, P. Bouchard, A. Mauger, C.M. Julien, M. Armand, K. Zaghib, New lithium metal polymer solid state battery for an ultrahigh energy: nano C-LiFePO₄ versus nano Li_{1.2}V₃O₈, *Nano Lett.* 15 (2015) 2671–2678, <https://doi.org/10.1021/acs.nanolett.5b00326>.
- [12] K. Zaghib, A. Guerfi, P. Hovington, A. Vijh, M. Trudeau, A. Mauger, J. B. Goodenough, C.M. Julien, Review and analysis of nanostructured olivine-based lithium rechargeable batteries: status and trends, *J. Power Sources* 232 (2013) 357–369, <https://doi.org/10.1016/j.jpowsour.2012.12.095>.
- [13] Y. Maeyoshi, S. Miyamoto, Y. Noda, H. Munakata, K. Kanamura, Effect of organic additives on characteristics of carbon-coated LiCoPO₄ synthesized by hydrothermal method, *J. Power Sources* 337 (2017) 92–99, <https://doi.org/10.1016/j.jpowsour.2016.10.106>.
- [14] H. El-Shinawi, E.J. Cussen, S.A. Corr, Morphology-directed synthesis of LiFePO₄ and LiCoPO₄ from nanostructured Li_{1+x}PO_{3+x}, *Inorg. Chem.* 58 (2019) 6946–6949, <https://doi.org/10.1021/acs.inorgchem.9b00517>.
- [15] K. Zaghib, M.V. Reddy, A. Mauger, F. Gendron, C.M. Julien, J.B. Goodenough, Secondary batteries – lithium rechargeable systems – lithium-ion | positive electrode: lithium iron phosphate. in: *Ref. Module Chem. Mol. Sci. Chem. Eng.*, Elsevier, 2023, <https://doi.org/10.1016/B978-0-323-96022-9.00060-8>.
- [16] Clarivate Analytics, Web Science and Core Collection2023(<https://www.webofscience.com/wos/>).
- [17] N. Tolganbek, Y. Yerkinbekova, S. Kalybekkyzy, Z. Bakenov, A. Mentbayeva, Current state of high voltage olivine structured LiMPO₄ cathode materials for energy storage applications: a review, *J. Alloy. Compd.* 882 (2021) 160774, <https://doi.org/10.1016/j.jallcom.2021.160774>.
- [18] Y. Zhang, H. Xie, H. Jin, Q. Zhang, Y. Li, X. Li, K. Li, C. Bao, Research status of spinel LiMn₂O₄ cathode materials for lithium ion batteries, *IOP Conf. Ser. Earth Environ. Sci.* 603 (2020) 012051, <https://doi.org/10.1088/1755-1315/603/1/012051>.
- [19] K.T. Lee, J. Cho, Roles of nanosize in lithium reactive nanomaterials for lithium ion batteries, *Nano today* 6 (2011) 28–41, <https://doi.org/10.1016/j.nantod.2010.11.002>.
- [20] T.A. Wani, G. Suresh, A comprehensive review of LiMnPO₄ based cathode materials for lithium-ion batteries: current strategies to improve its performance, *J. Energy Storage* 44 (2021) 103307, <https://doi.org/10.1016/j.est.2021.103307>.
- [21] L. Wang, H. Zhang, Q. Liu, J. Wang, Y. Ren, X. Zhang, G. Yin, J. Wang, P. Zuo, Modifying high-voltage olivine-type LiMnPO₄ cathode via Mg substitution in high-orientation crystal, *ACS Appl. Energy Mater.* 1 (2018) 5928–5935, <https://doi.org/10.1021/acsaem.8b00923>.
- [22] G. Li, B. Huang, Z. Pan, X. Su, Z. Shao, L. An, Advances in three-dimensional graphene-based materials: configurations, preparation and application in secondary metal (Li, Na, K, Mg, Al)-ion batteries, *Energy Environ. Sci.* 12 (2019) 2030–2053, <https://doi.org/10.1039/C8EE03014F>.
- [23] T. Boyadzhieva, V. Koleva, R. Stoyanova, Crystal chemistry of Mg substitution in NaMnPO₄ olivine: concentration limit and cation distribution, *Phys. Chem. Chem. Phys.* 19 (2017) 12730–12739, <https://doi.org/10.1039/C7CP01947E>.
- [24] J. Xiao, X. Li, K. Tang, D. Wang, M. Long, H. Gao, W. Chen, C. Liu, H. Liu, G. Wang, Recent progress of emerging cathode materials for sodium ion batteries, *Mater. Chem. Front.* 5 (2021) 3735–3764, <https://doi.org/10.1039/D1QM00179E>.
- [25] J.-Y. Hwang, S.-T. Myung, Y.-K. Sun, Sodium-ion batteries: present and future, *Chem. Soc. Rev.* 46 (2017) 3529–3614, <https://doi.org/10.1039/C6CS00776G>.
- [26] X. Min, J. Xiao, M. Fang, W. (Alex) Wang, Y. Zhao, Y. Liu, AmrM. Abdelkader, K. Xi, R.V. Kumar, Z. Huang, Potassium-ion batteries: outlook on present and future technologies, *Energy Environ. Sci.* 14 (2021) 2186–2243, <https://doi.org/10.1039/D0EE02917C>.
- [27] C. You, X. Wu, X. Yuan, Y. Chen, L. Liu, Y. Zhu, L. Fu, Y. Wu, Y.-G. Guo, T. van Ree, Advances in rechargeable Mg batteries, *J. Mater. Chem. A* 8 (2020) 25601–25625, <https://doi.org/10.1039/D0TA09330K>.
- [28] Battery Critical Materials Supply Chain Challenges and Opportunities: Results of the 2020 Request for Information (RFI) and Workshop, Office of Energy Efficiency & Renewable Energy, the US Department of Energy (DOE), 2022. (<https://www.energy.gov/sites/default/files/2022-01/Battery%20Critical%20Materials%20Workshop%20Report%20-%20FINAL.pdf>).
- [29] A.-L. Toba, R.T. Nguyen, C. Cole, G. Neupane, M.P. Paranthaman, U.S. lithium resources from geothermal and extraction feasibility, *Resour. Conserv. Recycl.* 169 (2021) 105514, <https://doi.org/10.1016/j.resconrec.2021.105514>.
- [30] Lithium Production, 2021, and Projected Demand in Climate-driven Scenarios, 2030, (2022). (<https://www.iea.org/data-and-statistics/charts/lithium-production-2021-and-projected-demand-in-climate-driven-scenarios-2030>).
- [31] Committed Mine Production and Primary Demand for Lithium, 2020–2030, (2021). (<https://www.iea.org/data-and-statistics/charts/committed-mine-production-and-primary-demand-for-lithium-2020-2030>).
- [32] Global Production of Lithium by Route, 2019 and 2050, (2020). (<https://www.iea.org/data-and-statistics/charts/global-production-of-lithium-by-route-2019-and-2050>).
- [33] M. Garside, 2023, (<https://www.statista.com/statistics/268789/countries-with-the-largest-production-output-of-lithium/>), Major Ctries. Worldw. Lithium mine Prod. 2022..
- [34] M.L. Vera, W.R. Torres, C.I. Galli, A. Chagnes, V. Flexer, Environmental impact of direct lithium extraction from brines, *Nat. Rev. Earth Environ.* 4 (2023) 149–165, <https://doi.org/10.1038/s43017-022-00387-5>.
- [35] H. Zhao, Y. Wang, H. Cheng, Recent advances in lithium extraction from lithium-bearing clay minerals, *Hydrometallurgy* 217 (2023) 106025, <https://doi.org/10.1016/j.hydromet.2023.106025>.
- [36] L. Zhu, H. Gu, H. Wen, Y. Yang, Lithium extraction from clay-type lithium resource using ferric sulfate solutions via an ion-exchange leaching process, *Hydrometallurgy* 206 (2021) 105759, <https://doi.org/10.1016/j.hydromet.2021.105759>.
- [37] S. Ventura, S. Bhamidi, M. Hornbostel, A. Nagar, Selective Recovery of Lithium from Geothermal Brines, California Energy Commission, 2020. (<https://www.energy.ca.gov/sites/default/files/2021-05/CEC-500-2020-020.pdf>).
- [38] Lithium valley: Powering our Clean Energy Transition, Geothermal Technologies Office, Office of Energy Efficiency & Renewable Energy, the US Department of Energy (DOE), 2022. (<https://www.energy.gov/eere/geothermal/articles/lithium-valley-powering-our-clean-energy-transition>).
- [39] C.B. Tabejin, J. Dallas, S. Casanova, T. Pelech, G. Bournival, S. Saydam, I. Canbulat, Towards a low-carbon society: a review of lithium resource availability, challenges and innovations in mining, extraction and recycling, and future perspectives, *Miner. Eng.* 163 (2021) 106743, <https://doi.org/10.1016/j.mineng.2020.106743>.
- [40] X. He, S. Kaur, R. Kostecki, Mining lithium from seawater, *Joule* 4 (2020) 1357–1358, <https://doi.org/10.1016/j.joule.2020.06.015>.
- [41] Z. Li, C. Li, X. Liu, L. Cao, P. Li, R. Wei, X. Li, D. Guo, K.-W. Huang, Z. Lai, Continuous electrical pumping membrane process for seawater lithium mining, *Energy Environ. Sci.* 14 (2021) 3152–3159, <https://doi.org/10.1039/D1EE00354B>.
- [42] C. Dang, A.S. Helal, L. Zhu, G. Xu, M. Zhu, Industrial pathways to lithium extraction from seawater: challenges and perspectives, *Nano Res. Energy* 2 (2023) e9120059, <https://doi.org/10.26599/NRE.2023.9120059>.
- [43] C. Liu, Y. Li, D. Lin, P.-C. Hsu, B. Liu, G. Yan, T. Wu, Y. Cui, S. Chu, Lithium extraction from seawater through pulsed electrochemical intercalation, *Joule* 4 (2020) 1459–1469, <https://doi.org/10.1016/j.joule.2020.05.017>.
- [44] S. Yang, F. Zhang, H. Ding, P. He, H. Zhou, Lithium metal extraction from seawater, *Joule* 2 (2018) 1648–1651, <https://doi.org/10.1016/j.joule.2018.07.006>.
- [45] T.-Y. Huang, J.R. Pérez-Cardona, F. Zhao, J.W. Sutherland, M.P. Paranthaman, Life cycle assessment and techno-economic assessment of lithium recovery from geothermal brine, *ACS Sustain. Chem. Eng.* 9 (2021) 6551–6560, <https://doi.org/10.1021/acsschemeng.0c08733>.
- [46] D. Castelvaggi, Electric cars and batteries: how will the world produce enough? *Nature* 596 (2021) 336–339, <https://doi.org/10.1038/d41586-021-02222-1>.
- [47] B.M. Spears, W.J. Brownlie, D. Cordell, L. Hermann, J.M. Mogollón, Concerns about global phosphorus demand for lithium-iron-phosphate batteries in the light electric vehicle sector, *Commun. Mater.* 3 (2022) 14, <https://doi.org/10.1038/s43246-022-00236-4>.
- [48] L. Mathieu, C. MatteaFrom dirty oil to clean batteries, European Federation for Transport & Environment2021, (https://www.transportenvironment.org/wp-content/uploads/2021/07/2021_02_Battery_raw_materials_report_final.pdf), From dirty oil to clean batteries, European Federation for Transport & Environment..
- [49] J.C. Kelly, M. Wang, Q. Dai, O. Winjobi, Energy, greenhouse gas, and water life cycle analysis of lithium carbonate and lithium hydroxide monohydrate from brine and ore resources and their use in lithium ion battery cathodes and lithium ion batteries, *Resour. Conserv. Recycl.* 174 (2021) 105762, <https://doi.org/10.1016/j.resconrec.2021.105762>.
- [50] R. Zhang, X. Ma, X. Shen, Y. Zhai, T. Zhang, C. Ji, J. Hong, Life cycle assessment of electrolytic manganese metal production, *J. Clean. Prod.* 253 (2020) 119951, <https://doi.org/10.1016/j.jclepro.2019.119951>.
- [51] K. Hagelstein, Globally sustainable manganese metal production and use, *Sustain. Ind. Environ. Syst.* 9 (2009) 3736–3740, <https://doi.org/10.1016/j.jenvman.2008.05.025>.
- [52] Can Geothermal Energy Solve the Lithium Shortfall?, Geothermal Technologies Office, Office of Energy Efficiency & Renewable Energy, The US Department of Energy (DOE), 2021. (<https://www.energy.gov/eere/geothermal/articles/can-geothermal-energy-solve-lithium-shortfall#:~:text=Hot%20salty%20water%2C%20or%20geothermal,from%20thousands%20of%20feet%20underground>).
- [53] A. Breiter, E. Horetsky, M. Linder, R. Rettig, Power spike: how battery makers can respond to surging demand from EVs, McKinsey Co, 2022. (<https://www.mckinsey.com/capabilities/operations/our-insights/power-spike-how-battery-makers-can-respond-to-surging-demand-from-evs>).
- [54] Trends in Batteries, Battery Demand For EVs continues to Rise, (2023). (<https://www.iea.org/reports/global-ev-outlook-2023/trends-in-batteries>).
- [55] D. Guven, M. Ozgur Kayalica, Life-cycle assessment and life-cycle cost assessment of lithium-ion batteries for passenger ferry, *Transp. Res. Part Transp. Environ.* 115 (2023) 103586, <https://doi.org/10.1016/j.trd.2022.103586>.
- [56] C. Xu, Q. Dai, L. Gaines, M. Hu, A. Tukker, B. Steubing, Future material demand for automotive lithium-based batteries, *Commun. Mater.* 1 (2020) 99, <https://doi.org/10.1038/s43246-020-00095-x>.
- [57] Race to Net Zero: the Pressures of the Battery Boom in Five Charts, (2022). (<https://about.bnef.com/about/?bbgsum-page=DG-WS-BNEF-blog-post-189484&mpam-page=MPAM-blog-post&tactic-page=596500>).
- [58] M. Creamer, 2022, (<https://www.miningweekly.com/article/high-purity-manganese-facing-phenomenal-growth-pdac-hears-2022-06-24>), High-purity manganese facing phenomenal demand growth, PDAC hears, Miningweekly.
- [59] Global HPMSM market, Can. Manganese (n.d.). (<https://canadianmanganese.com/hpmsm/global-hpmsm-market/>).

- [60] Mineral requirements for clean energy transitions, (n.d.). (<https://www.iea.org/reports/the-role-of-critical-minerals-in-clean-energy-transitions/mineral-requirements-for-clean-energy-transitions>).
- [61] M.J. Kim, T. Tran, Method for Producing High-purity Manganese Sulfate Monohydrate and High-purity Manganese Sulfate Monohydrate Produced by the Method, US20150110692A1, 2015. (<https://patents.google.com/patent/US20150110692A1/en>).
- [62] Zh. Jiang, D. Hua, Method for Preparing Manganese Sulfate, EP10799405A1, 2012.
- [63] Q. Lin, G. Gu, H. Wang, R. Zhu, Y. Liu, J. Fu, Preparation of manganese sulfate from low-grade manganese carbonate ores by sulfuric acid leaching, *Int. J. Miner. Metall. Mater.* 23 (2016) 491–500, <https://doi.org/10.1007/s12613-016-1260-x>.
- [64] HPMSM processing 101, Process Routes for High Purity Manganese Production, Can. Manganese (n.d.). (<https://canadianmanganese.com/hpmsm/hpmsm-processing-101/>).
- [65] S. He, D. Jiang, M. Hong, Z. Liu, Hazard-free treatment and resource utilisation of electrolytic manganese residue: a review, *J. Clean. Prod.* 306 (2021) 127224, <https://doi.org/10.1016/j.jclepro.2021.127224>.
- [66] N. Wang, Z. Fang, S. Peng, D. Cheng, B. Du, C. Zhou, Recovery of soluble manganese from electrolyte manganese residue using a combination of ammonia and CO₂, *Hydrometallurgy* 164 (2016) 288–294, <https://doi.org/10.1016/j.hydromet.2016.06.019>.
- [67] R.J. Holmes, Y. Lu, L. Lu, Chapter 1- introduction: overview of the global iron ore industry, in: L. Lu (Ed.), *Iron Ore Second Ed.*, Woodhead Publishing, 2022, pp. 1–56, <https://doi.org/10.1016/B978-0-12-820226-5.00023-9>.
- [68] Iron ore facts, Canada.ca, 2023. (<https://natural-resources.canada.ca/our-natural-resources/minerals-mining/minerals-metals-facts/iron-ore-facts/20517>).
- [69] Reserves of iron ore worldwide in 2022, by country, (2023). (<https://www.statista.com/statistics/267381/world-reserves-of-iron-ore-by-country/>).
- [70] J.M.F. Clout, J.R. Manuel, Chapter 2- Mineralogical, chemical, and physical metallurgical characteristics of iron ore, in: L. Lu (Ed.), *Iron Ore Second Ed.*, Woodhead Publishing, 2022, pp. 59–108, <https://doi.org/10.1016/B978-0-12-820226-5.00012-4>.
- [71] I.T.P. Mining, Energy and environmental profile of the U.S. mining industry: chapter 4: iron, The US Department of Energy (DOE), 2013. (<https://www.energy.gov/sites/prod/files/2013/11/f4/iron.pdf>).
- [72] R. Stace, Chapter 7- Iron ore extraction techniques, in: L. Lu (Ed.), *Iron Ore Second Ed.*, Woodhead Publishing, 2022, pp. 249–268, <https://doi.org/10.1016/B978-0-12-820226-5.00025-2>.
- [73] N.V. Nikolaeva, T.N. Aleksandrova, E.L. Chanturiya, A. Afanasova, Mineral and technological features of magnetite–hematite ores and their influence on the choice of processing technology, *ACS Omega* 6 (2021) 9077–9085, <https://doi.org/10.1021/acsomega.1c00129>.
- [74] A. Jankovic, Chapter 8- Comminution and classification technologies of iron ore, in: L. Lu (Ed.), *Iron Ore Second Ed.*, Woodhead Publishing, 2022, pp. 269–308, <https://doi.org/10.1016/B978-0-12-820226-5.00013-6>.
- [75] D. Xiong, L. Lu, R.J. Holmes, Chapter 9- physical separation of iron ore: magnetic separation, in: L. Lu (Ed.), *Iron Ore Second Ed.*, Woodhead Publishing, 2022, pp. 309–332, <https://doi.org/10.1016/B978-0-12-820226-5.00010-0>.
- [76] W.J. Bruckard, L.K. Smith, G.W. Heyes, G.J. Sparrow, Chapter 11- physicochemical separation of iron ore, in: L. Lu (Ed.), *Iron Ore Second Ed.*, Woodhead Publishing, 2022, pp. 375–396, <https://doi.org/10.1016/B978-0-12-820226-5.00017-3>.
- [77] G.J. Sparrow, L. Lu, R.R. Lovel, M.J. Fisher-White, Chapter 12- chemical separation of iron ore, in: L. Lu (Ed.), *Iron Ore Second Ed.*, Woodhead Publishing, 2022, pp. 397–420, <https://doi.org/10.1016/B978-0-12-820226-5.00005-7>.
- [78] L. Lu, O. Ishiyama, T. Higuchi, M. Matsumura, K. Higuchi, Chapter 15- iron ore sintering, in: L. Lu (Ed.), *Iron Ore Second Ed.*, Woodhead Publishing, 2022, pp. 489–538, <https://doi.org/10.1016/B978-0-12-820226-5.00006-9>.
- [79] D. Zhu, J. Pan, L. Lu, R.J. Holmes, Chapter 16 - Iron ore pelletization, in: L. Lu (Ed.), *Iron Ore Second Ed.*, Woodhead Publishing, 2022, pp. 539–578, <https://doi.org/10.1016/B978-0-12-820226-5.00014-8>.
- [80] M. Ruth, *Steel Production and Energy*, in: C.J. Cleveland (Ed.), *Encycl. Energy*, Elsevier, New York, 2004, pp. 695–706, <https://doi.org/10.1016/B0-12-176480-X/00371-5>.
- [81] P. Jin, Z. Jiang, C. Bao, S. Hao, X. Zhang, The energy consumption and carbon emission of the integrated steel mill with oxygen blast furnace, *Resour. Effic. Chin. Ind.* 117 (2017) 58–65, <https://doi.org/10.1016/j.resconrec.2015.07.008>.
- [82] J. Kim, B.K. Sovacool, M. Bazilian, S. Griffiths, J. Lee, M. Yang, J. Lee, Decarbonizing the iron and steel industry: a systematic review of sociotechnical systems, technological innovations, and policy options, *Energy Res. Soc. Sci.* 89 (2022) 102565, <https://doi.org/10.1016/j.erss.2022.102565>.
- [83] N. Haque, Chapter 20- Life cycle assessment of iron ore mining and processing, in: L. Lu (Ed.), *Iron Ore Second Ed.*, Woodhead Publishing, 2022, pp. 691–710, <https://doi.org/10.1016/B978-0-12-820226-5.00007-0>.
- [84] H.Y. Sohn, Energy consumption and CO₂ emissions in ironmaking and development of a novel flash technology, *Metals* 10 (2020), <https://doi.org/10.3390/met10010054>.
- [85] Tracking Steel in Tracking Clean Energy Progress 2023, (2023). (<https://www.iea.org/energy-system/industry/steel>).
- [86] G. Bhutata, The key minerals in an EV battery, *Vis. Capital*, 2022. (<https://elements.visualcapitalist.com/the-key-minerals-in-an-ev-battery/>).
- [87] T.D. Grandi, 4 Benefits of LFP batteries for EVs, *Vis. Capital*. (n.d.). (<https://www.visualcapitalist.com/sp/4-benefits-of-lfp-batteries/>).
- [88] BloombergNEF: Battery Metals Rebounding; by 2030, Annual Li-ion Battery Demand to Pass 2TWh, *Green Car Congr.* (2021). (<https://www.greencarcongress.com/2021/07/20210701-bnef.html>).
- [89] European Commission, *European Commission*, 2020.
- [90] W.J. Brownlie, M.A. Sutton, K.V. Heal, D.S. Reay, B.M. Spears (eds.), *Our Phosphorus Future*, UK Centre for Ecology and Hydrology, Edinburgh, 2022. (https://static1.squarespace.com/static/60ab7d2902207048adc8c540/t/62fa5a370393cf7604a50879/1660574297780/2022_The+OPF+Report_images+compressed.pdf).
- [91] W.J. Brownlie, M.A. Sutton, D.S. Reay, K.V. Heal, L. Hermann, C. Kabbe, B. M. Spears, Global actions for a sustainable phosphorus future, *Nat. Food* 2 (2021) 71–74, <https://doi.org/10.1038/s43016-021-00232-w>.
- [92] F. Jones, Norway to develop massive phosphate deposit, *Min. Technol.* (2023). (<https://www.mining-technology.com/news/norway-giant-phosphate-deposit/>).
- [93] E.K. Cakmak, M. Hartl, J. Kisser, Z. Cetecioglu, Phosphorus mining from eutrophic marine environment towards a blue economy: the role of bio-based applications, *Water Res.* 219 (2022) 118505, <https://doi.org/10.1016/j.watres.2022.118505>.
- [94] Petr Ptáček, Mining and beneficiation of phosphate ore, in: Petr Ptáček (Ed.), *Apatites Their Synth. Analog*, IntechOpen, Rijeka, 2016, p. Ch. 8, <https://doi.org/10.5772/62215>.
- [95] S.M. Jasinski, Mineral commodity summaries 2022 - Phosphate, United States Geological Survey, 2022. (<https://pubs.usgs.gov/periodicals/mcs2022/mcs2022-phosphate.pdf>).
- [96] Y. Li, L. Wang, H. Zhang, F. Liang, Y. Yao, K. Zhang, Freeze drying under vacuum assisted synthesis of LiFePO₄@MWNTs composite with phytic acid as phosphorus source for advanced Li-storage, *Vacuum* 193 (2021) 110541, <https://doi.org/10.1016/j.vacuum.2021.110541>.
- [97] C. Xu, Q. Dai, L. Gaines, M. Hu, A. Tukker, B. Steubing, Reply to: concerns about global phosphorus demand for lithium-iron-phosphate batteries in the light electric vehicle sector, *Commun. Mater.* 3 (2022) 15, <https://doi.org/10.1038/s43246-022-00237-3>.
- [98] C. Shen, G. Li, L. Liu, P. Li, H. Xu, H. Hu, L. Wang, Facile fabrication of compact LiFePO₄/C composite with excellent atomically-efficient for high-energy-density Li-ion batteries, *J. Power Sources* 496 (2021) 229759, <https://doi.org/10.1016/j.jpowsour.2021.229759>.
- [99] X. Pan, Y. Sun, S. Zhuang, G. Sun, S. Jiang, Y. Ren, Y. Wen, X. Li, F. Tu, An inexpensive preparation of unique nano-micro porous LiFePO₄ cathode with excellent rate capability for lithium-ion batteries, *Vacuum* 212 (2023) 112258, <https://doi.org/10.1016/j.vacuum.2023.112258>.
- [100] S. Bolloju, R. Rohan, S.-T. Wu, H.-X. Yen, G.D. Dwivedi, Y.A. Lin, J.-T. Lee, A green and facile approach for hydrothermal synthesis of LiFePO₄ using iron metal directly, *Electrochim. Acta* 220 (2016) 164–168, <https://doi.org/10.1016/j.electacta.2016.10.066>.
- [101] M. Talebi-Esfandarani, S. Rousselot, M. Gauthier, P. Sauriol, G. Liang, M. Dollé, LiFePO₄ synthesized via melt synthesis using low-cost iron precursors, *J. Solid State Electrochem.* 20 (2016) 1821–1829, <https://doi.org/10.1007/s10008-015-3049-7>.
- [102] J. Yao, X. Wang, P. Zhang, J. Wang, J. Xie, K.-F. Aguey-Zinsou, C. Ma, L. Wang, High purity lithium iron phosphate/carbon composites prepared by using secondary lithium source, *Powder Technol.* 237 (2013) 160–164, <https://doi.org/10.1016/j.powtec.2013.01.041>.
- [103] K. Pardikar, J. Entwistle, R. Ge, D. Cumming, R. Smith, Status and outlook for lithium-ion battery cathode material synthesis and the application of mechanistic modeling, *J. Phys. Energy* 5 (2023) 022002, <https://doi.org/10.1088/2515-7655/acc139>.
- [104] W.-C. Chien, K.-N. Liu, S.-C. Chang, C.-C. Yang, Effects of α-Fe₂O₃ size and morphology on performance of LiFePO₄/C cathodes for Li-ion batteries, *Thin Solid Films* 660 (2018) 931–937, <https://doi.org/10.1016/j.tsf.2018.02.017>.
- [105] M.E. Zhong, Z.T. Zhou, Preparation of high tap-density LiFePO₄/C composite cathode materials by carbothermal reduction method using two kinds of Fe₃+ precursors, *Mater. Chem. Phys.* 119 (2010) 428–431, <https://doi.org/10.1016/j.matchemphys.2009.09.017>.
- [106] Z. Xiao, G. Hu, A novel synthesis of LiFePO₄/C from Fe₂O₃ without extra carbon or carbon-containing reductant, *J. Cent. South Univ.* 21 (2014) 2143–2149, <https://doi.org/10.1007/s11771-014-2164-4>.
- [107] Y. Wang, H. Li, M. Chen, X. Yang, D. Jiang, Synthesis and electrochemical performance of LiFePO₄/C cathode materials from Fe₂O₃ for high-power lithium-ion batteries, *Ionics* 23 (2017) 377–384, <https://doi.org/10.1007/s11581-016-1910-z>.
- [108] B. Rong, Y. Lu, X. Liu, Q. Chen, K. Tang, H. Yang, X. Wu, F. Shen, Y. Chen, Y. Tang, Y. Chen, Fabrication and characteristics of nano LiFePO₄/C composites with high capacity and high rate using nano Fe₂O₃ as raw materials, *Nano Energy* 6 (2014) 173–179, <https://doi.org/10.1016/j.nanoen.2014.03.017>.
- [109] B.M. Kerbel, L.M. Katsnelson, Yu.V. Falkovich, Continuous solid-phase synthesis of nanostructured lithium iron phosphate powders in air, *Ceram. Int.* 44 (2018) 8397–8402, <https://doi.org/10.1016/j.ceramint.2018.02.032>.
- [110] M. Li, L. Sun, K. Sun, R. Wang, H. Xie, An optimum route to prepare FePO₄·2H₂O and its use as an iron source to synthesize LiFePO₄, *Sci. China Chem.* 56 (2013) 576–582, <https://doi.org/10.1007/s11426-012-4818-0>.
- [111] J. Guo, C. Liang, J. Cao, S. Jia, Synthesis and electrochemical performance of lithium iron phosphate/carbon composites based on controlling the secondary morphology of precursors, *Int. J. Hydrog. Energy* 45 (2020) 33016–33027, <https://doi.org/10.1016/j.ijhydene.2020.09.049>.
- [112] D. Zhou, X. Qiu, F. Liang, S. Cao, Y. Yao, X. Huang, W. Ma, B. Yang, Y. Dai, Comparison of the effects of FePO₄ and FePO₄·2H₂O as precursors on the

- electrochemical performances of LiFePO₄/C, *Ceram. Int.* 43 (2017) 13254–13263, <https://doi.org/10.1016/j.ceramint.2017.07.023>.
- [113] J. Guo, Y. Peng, X. Mo, G. Liao, Preparation of LiFePO₄ using iron(II) sulfate as product from titanium dioxide slag purification process and its electrochemical properties, *Int. J. Electrochem. Sci.* 16 (2021) 211141, <https://doi.org/10.20964/2021.11.09>.
- [114] D. Yi, X. Cui, N. Li, L. Zhang, D. Yang, Enhancement of electrochemical performance of LiFePO₄@C by Ga coating, *ACS Omega* 5 (2020) 9752–9758, <https://doi.org/10.1021/acsomega.9b04165>.
- [115] J. Li, J. Wu, Y. Li, H. Zhao, T. Zhao, S. Ma, H. Liu, Facile strategies to utilize FeSO₄·7H₂O waste slag for LiFePO₄/C cathode with high performances, *J. Taiwan Inst. Chem. Eng.* 99 (2019) 74–81, <https://doi.org/10.1016/j.jtice.2019.03.002>.
- [116] K. Dokko, T. Hachida, M. Watanabe, LiMnPO₄ nanoparticles prepared through the reaction between Li₃PO₄ and molten aqua-complex of MnSO₄, *J. Electrochem. Soc.* 158 (2011) A1275, <https://doi.org/10.1149/2.015112jes>.
- [117] I.D. Johnson, M. Loveridge, R. Bhagat, J.A. Darr, Mapping structure-composition-property relationships in V- and Fe-doped LiMnPO₄ cathodes for lithium-ion batteries, *ACS Comb. Sci.* 18 (2016) 665–672, <https://doi.org/10.1021/acscombsci.6b00035>.
- [118] J. Zheng, J. Yang, J. Wu, S. Li, M. Wang, B. Huang, Y. Li, S. Xiao, Q. Zhu, Y₃+ doping and electrochemical properties of LiFe_{0.5}Mn_{0.5}PO₄@C cathode material for lithium-ion batteries, *J. Alloy. Compd.* 960 (2023) 170610, <https://doi.org/10.1016/j.jallcom.2023.170610>.
- [119] Z. Yi, J. Fu, Z. Mu, X. yang, Y. Sang, Rheological phase reaction synthesis and electrochemical performance of LiFe₂/3Mn₁/3PO₄/C cathode for lithium-ion batteries, *J. Mater. Sci. Mater. Electron.* 33 (2022) 18364–18373, <https://doi.org/10.1007/s10854-022-08691-y>.
- [120] B. Zhang, X. Xie, Z. Peng, G. Hu, K. Du, B. Makuza, Y. Gong, X. Ji, Y. Cao, Synthesis of flexible LiMn_{0.8}Fe_{0.2}PO₄/C microsphere and its synergetic effects with blended LiNi_{0.85}Co_{0.10}Al_{0.05}O₂ electrodes, *J. Power Sources* 541 (2022) 231671, <https://doi.org/10.1016/j.jpowsour.2022.231671>.
- [121] B. Zhang, W. Meng, Y. Gong, G. Hu, Z. Peng, K. Du, B. Makuza, J. Wu, X. Xie, Y. Cao, 001]-oriented LiMn_{0.6}Fe_{0.4}PO₄/C nanorod microspheres contributing high-rate performance to olivine-structured cathode for lithium-ion battery, *Mater. Today Energy* 30 (2022) 101162, <https://doi.org/10.1016/j.mtener.2022.101162>.
- [122] Y. Zhu, Z. Ruan, S. Tang, V. Thangadurai, Research status in preparation of FePO₄: a review, *Ionics* 20 (2014) 1501–1510, <https://doi.org/10.1007/s11581-014-1241-x>.
- [123] W. Yu, FePO₄ synthesis method, CN103754855A, 2014. (<https://patents.google.com/patent/CN103754855A/en>).
- [124] X. Ming, R. Wang, T. Li, X. Wu, L. Yuan, Y. Zhao, Preparation of micro-nano-structured FePO₄·2H₂O for LiFePO₄ cathode materials by the turbulent flow cycle method, *ACS Omega* 6 (2021) 18957–18963, <https://doi.org/10.1021/acsomega.1c02216>.
- [125] L. Yongjia, L. Yin, Z. Keyu, X. Ruhui, Y. Meimei, Y. Yaochun, Influence of synthesis parameters on the properties of FePO₄·2H₂O used for the precursor of LiFePO₄ cathode material, *Ionics* 27 (2021) 983–991, <https://doi.org/10.1007/s11581-020-03864-3>.
- [126] B. Mandal, I. Basumallick, S. Ghosh, Synthesis of highly dispersed FePO₄ cathode material for rechargeable lithium battery, *Adv. Mater. Proc.* 2 (2017) 218–222, <https://doi.org/10.5185/amp.2017/403>.
- [127] L.W. Beck, M. Soltani, L. Wang, Ferric Phosphate and Methods of Preparation Thereof, US9174846B2, 2015. (<https://patents.google.com/patent/US9174846B2/en>).
- [128] Z. Youxiang, W. Meng, Z. Keli, Preparation Method of Nano-flaky FePO₄·2H₂O, CN102009968A, 2011. (<https://patents.google.com/patent/CN102009968A/en>).
- [129] Y. Fang, L. Xiao, J. Qian, X. Ai, H. Yang, Y. Cao, Mesoporous amorphous FePO₄ nanospheres as high-performance cathode material for sodium-ion batteries, *Nano Lett.* 14 (2014) 3539–3543, <https://doi.org/10.1021/nl501152f>.
- [130] X. Zhao, M. Luo, K. Peng, Z. Zhang, B. Cheng, B. Wang, C. Zhu, X. Yan, K. Shi, Low-temperature synthesis of amorphous FePO₄@rGO composites for cost-effective sodium-ion batteries, *ACS Appl. Mater. Interfaces* 13 (2021) 57442–57450, <https://doi.org/10.1021/acsaami.1c18800>.
- [131] Y. Liu, Y. Xu, X. Han, C. Pellegrinelli, Y. Zhu, H. Zhu, J. Wan, A.C. Chung, O. Vaaland, C. Wang, L. Hu, Porous amorphous FePO₄ nanoparticles connected by single-wall carbon nanotubes for sodium ion battery cathodes, *Nano Lett.* 12 (2012) 5664–5668, <https://doi.org/10.1021/nl302819f>.
- [132] Z. Wang, Y. Lu, Amorphous FePO₄/carbon nanotube cathode preparation via in Situ nanoprecipitation and coagulation in a microreactor, *ACS Omega* 4 (2019) 14790–14799, <https://doi.org/10.1021/acsomega.9b01343>.
- [133] Z. Wang, Y. Lu, Facile construction of high-performance amorphous FePO₄/carbon nanomaterials as cathodes of lithium-ion batteries, *ACS Appl. Mater. Interfaces* 11 (2019) 13225–13233, <https://doi.org/10.1021/acsaami.8b22720>.
- [134] Sh Liu, A Kind of Preparation Method of Battery Grade Ferrous Sulfate Heptahydrate Crystal, CN105293588B, 2015. (<https://patents.google.com/patent/CN105293588B>).
- [135] Z. Peng, Y. Cao, Y. Zhou, G. Hu, Synthesis of LiFePO₄ using FeSO₄·7H₂O byproduct from TiO₂ production as raw material, *Rare Met.* 28 (2009) 612–617, <https://doi.org/10.1007/s12598-009-0117-0>.
- [136] Y. Jiang, C. Peng, K. Zhou, Z. Hu, G. Zhang, Y. Wu, J. Zhang, W. Chen, Recovery of iron from titanium white waste for the preparation of LiFePO₄ battery, *J. Clean. Prod.* 415 (2023) 137817, <https://doi.org/10.1016/j.jclepro.2023.137817>.
- [137] S. Zhong, Y. Wang, J. Liu, J. Wang, Synthesis of LiMnPO₄/C composite material for lithium ion batteries by sol-gel method, *Trans. Nonferrous Met. Soc. China* 22 (2012) 2535–2540, [https://doi.org/10.1016/S1003-6326\(11\)61497-0](https://doi.org/10.1016/S1003-6326(11)61497-0).
- [138] Y. Li, B. Xing, H. Zhang, M. Wang, L. Yang, G. Xu, S. Yang, Simple synthesis of a hierarchical LiMn_{0.8}Fe_{0.2}PO₄/C cathode by investigation of iron sources for lithium-ion batteries, *RSC Adv.* 12 (2022) 26070–26077, <https://doi.org/10.1039/D2RA04427G>.
- [139] E. Lyle, R. Vaeli, A. Dutta, M. Metzger, Melt synthesis of lithium manganese iron phosphate: part I. Composition, physical properties, structural analysis, and charge/discharge cycling, *J. Electrochem. Soc.* 169 (2022) 060526, <https://doi.org/10.1149/1945-7111/ac76e4>.
- [140] J. Herrera, H. Camacho-Montes, L. Fuentes, L. Álvarez-Contreras, LiMnPO₄: review on synthesis and electrochemical properties, *J. Chem. Eng. Mater. Sci.* 3 (2015) 54–64, <https://doi.org/10.4236/msce.2015.35007>.
- [141] F. Zhou, P. Zhu, X. Fu, R. Chen, R. Sun, C. Wong, Comparative study of LiMnPO₄ cathode materials synthesized by solvothermal methods using different manganese salts, *CrystEngComm* 16 (2014) 766–774, <https://doi.org/10.1039/C3CE41567H>.
- [142] V. Sharmila, M. Parthibavarman, Lithium manganese phosphate associated with MWNT: enhanced positive electrode for lithium hybrid batteries, *J. Alloy. Compd.* 858 (2021) 157715, <https://doi.org/10.1016/j.jallcom.2020.157715>.
- [143] C. Liu, X. Wu, W. Wu, J. Cai, S. Liao, Preparation of nanocrystalline LiMnPO₄ via a simple and novel method and its isothermal kinetics of crystallization, *J. Mater. Sci.* 46 (2011) 2474–2478, <https://doi.org/10.1007/s10853-010-5094-z>.
- [144] S.-L. Yang, R.-G. Ma, M.-J. Hu, L.-J. Xi, Z.-G. Lu, C.Y. Chung, Solvothermal synthesis of nano-LiMnPO₄ from Li₃PO₄ rod-like precursor: reaction mechanism and electrochemical properties, *J. Mater. Chem.* 22 (2012) 25402–25408, <https://doi.org/10.1039/C2JM34193J>.
- [145] H. Guo, C. Wu, J. Xie, S. Zhang, G. Cao, X. Zhao, Controllable synthesis of high-performance LiMnPO₄ nanocrystals by a facile one-spot solvothermal process, *J. Mater. Chem. A* 2 (2014) 10581–10588, <https://doi.org/10.1039/C4TA01365D>.
- [146] H. Guo, C. Wu, L. Liao, J. Xie, S. Zhang, P. Zhu, G. Cao, X. Zhao, Performance improvement of lithium manganese phosphate by controllable morphology tailoring with acid-engaged nano engineering, *Inorg. Chem.* 54 (2015) 667–674, <https://doi.org/10.1021/ic5026075>.
- [147] R. Fan, C. Fan, Z. Hu, T. Zeng, W. Zhang, S. Han, J. Liu, Construction of high performance N-doped carbon coated LiMn_{0.8}Fe_{0.2}PO₄ nanocrystal cathode for lithium-ion batteries, *J. Alloy. Compd.* 876 (2021) 160090, <https://doi.org/10.1016/j.jallcom.2021.160090>.
- [148] J.C. Barbosa, R. Gonçalves, C.M. Costa, S. Lanceros-Mendez, Recent advances on materials for lithium-ion batteries, *Energies* 14 (2021), <https://doi.org/10.3390/en14113145>.
- [149] J.-M. Tarascon, M. Armand, Issues and challenges facing rechargeable lithium batteries, *Nature* 414 (2001) 359–367, <https://doi.org/10.1038/3510464e>.
- [150] M. Kotal, S. Jakhra, S. Roy, H.K. Sharma, Cathode materials for rechargeable lithium batteries: recent progress and future prospects, *J. Energy Storage* 47 (2022) 103534, <https://doi.org/10.1016/j.est.2021.103534>.
- [151] S. Mahmud, M. Rahman, M. Kamruzzaman, M.O. Ali, M.S.A. Emon, H. Khatun, M. R. Ali, Recent advances in lithium-ion battery materials for improved electrochemical performance: a review, *Results Eng.* 15 (2022) 100472, <https://doi.org/10.1016/j.rineng.2022.100472>.
- [152] N. Mohamed, N.K. Allam, Recent advances in the design of cathode materials for Li-ion batteries, *RSC Adv.* 10 (2020) 21662–21685, <https://doi.org/10.1039/D0RA03314F>.
- [153] J.W. Fergus, Recent developments in cathode materials for lithium ion batteries, *J. Power Sources* 195 (2010) 939–954, <https://doi.org/10.1016/j.jpowsour.2009.08.089>.
- [154] H.-J. Kim, T. Krishna, K. Zeb, V. Rajangam, C.V.V.M. Gopi, S. Sambasivam, K. V. Raghavendra, I.M. Obaidat, A comprehensive review of li-ion battery materials and their recycling techniques, *Electronics* 9 (2020), <https://doi.org/10.3390/electronics9071161>.
- [155] K. Zaghib, A. Mauger, C.M. Julien, Overview of olivines in lithium batteries for green transportation and energy storage, *J. Solid State Electrochem.* 16 (2012) 835–845, <https://doi.org/10.1007/s10008-011-1629-8>.
- [156] B. Pei, H. Yao, W. Zhang, Z. Yang, Hydrothermal synthesis of morphology-controlled LiFePO₄ cathode material for lithium-ion batteries, *J. Power Sources* 220 (2012) 317–323, <https://doi.org/10.1016/j.jpowsour.2012.07.128>.
- [157] B. Xu, D. Qian, Z. Wang, Y.S. Meng, Recent progress in cathode materials research for advanced lithium ion batteries, *Mater. Sci. Eng. R. Rep.* 73 (2012) 51–65, <https://doi.org/10.1016/j.mser.2012.05.003>.
- [158] D. Jugović, D. Uskoković, A review of recent developments in the synthesis procedures of lithium iron phosphate powders, *J. Power Sources* 190 (2009) 538–544, <https://doi.org/10.1016/j.jpowsour.2009.01.074>.
- [159] A. Paoletta, S. Turner, G. Berton, P. Hovington, R. Flacau, C. Boyer, Z. Feng, M. Colombo, S. Marras, M. Prato, L. Manna, A. Guerfi, G.P. Demopoulos, M. Armand, K. Zaghib, Accelerated removal of Fe-antisite defects while nanosizing hydrothermal LiFePO₄ with Ca²⁺, *Nano Lett.* 16 (2016) 2692–2697, <https://doi.org/10.1021/acs.nanolett.6b00334>.
- [160] J. Ludwig, C. Marino, D. Haering, C. Stinner, D. Nordlund, M.M. Doeff, H. A. Gasteiger, T. Nilges, Facile, ethylene glycol-promoted microwave-assisted solvothermal synthesis of high-performance LiCoPO₄ as a high-voltage cathode material for lithium-ion batteries, *RSC Adv.* 6 (2016) 82984–82994, <https://doi.org/10.1039/C6RA19767A>.
- [161] A. Sarmadi, S.M. Masoudpanah, S. Alamolhoda, L-Lysine-assisted solvothermal synthesis of hollow-like structure LiFePO₄/C powders as cathode materials for Li-

- ion batteries, *J. Mater. Res. Technol.* 15 (2021) 5405–5413, <https://doi.org/10.1016/j.jmrt.2021.11.002>.
- [162] H. Yang, J.-G. Duh, H.-Y. Chen, Y. Wang, Synthesis and in-situ investigation of olivine LiMnPO₄ composites substituted with tetravalent vanadium in high-rate Li-ion batteries, *ACS Appl. Energy Mater.* 1 (2018) 6208–6216, <https://doi.org/10.1021/acsaem.8b01253>.
- [163] V. Garipey, A. Guerfi, K. Hanai, P. Hovington, Sh Saito, T. Sawai, K. Urao, K. Zaghbi, Method of Producing Electrode Material for Lithium-ion Secondary Battery and Lithium-ion Battery Using Such Electrode Material, EP 2909879 A1, 2015. (<https://lens.org/010-588-578-658-128>).
- [164] C.M. Julien, A. Mauger, J. Trottier, K. Zaghbi, P. Hovington, H. Groult, Olivine-based blended compounds as positive electrodes for lithium batteries, *Inorganics* 4 (2016), <https://doi.org/10.3390/inorganics4020017>.
- [165] K. Kanamura, S. Koizumi, K. Dokko, Hydrothermal synthesis of LiFePO₄ as a cathode material for lithium batteries, *J. Mater. Sci.* 43 (2008) 2138–2142, <https://doi.org/10.1007/s10853-007-2011-1>.
- [166] D.V. Trinh, M.T.T. Nguyen, H.T.M. Dang, D.T. Dang, H.T.T. Le, H.T.N. Le, H. V. Tran, C.D. Huynh, Hydrothermally synthesized nanostructured LiMn_xFe_{1-x}PO₄ (x = 0–0.3) cathode materials with enhanced properties for lithium-ion batteries, *Sci. Rep.* 11 (2021) 12280, <https://doi.org/10.1038/s41598-021-91881-1>.
- [167] L.T.N. Huynh, P.P.N. Le, V.D. Trinh, H.H. Tran, V.M. Tran, M.L.P. Le, Structure and electrochemical behavior of minor Mn-doped olivine LiMn_xFe_{1-x}PO₄, *J. Chem.* 2019 (2019) 5638590, <https://doi.org/10.1155/2019/5638590>.
- [168] J.-G. Zheng, G.-Y. Ren, J. Shi, T. Yang, Y.-F. Tang, Y.-F. Chen, Heterogeneous synthesis and electrochemical performance of LiMnPO₄/C composites as cathode materials of lithium ion batteries, *RSC Adv.* 10 (2020) 39981–39987, <https://doi.org/10.1039/D0RA08274K>.
- [169] M. Zhang, N. Garcia-Araez, A.L. Hector, Understanding and development of olivine LiCoPO₄ cathode materials for lithium-ion batteries, *J. Mater. Chem. A* 6 (2018) 14483–14517, <https://doi.org/10.1039/C8TA04063J>.
- [170] J. Chen, S. Wang, M.S. Whittingham, Hydrothermal synthesis of cathode materials, 13th Int. Meet. Lithium Batter 174 (2007) 442–448, <https://doi.org/10.1016/j.jpowsour.2007.06.189>.
- [171] O. Xiuqin, P. Lin, G. Haichen, W. Yichen, L. Jianwei, Temperature-dependent crystallinity and morphology of LiFePO₄ prepared by hydrothermal synthesis, *J. Mater. Chem.* 22 (2012) 9064–9068, <https://doi.org/10.1039/C2JM30191A>.
- [172] P. Benedek, N. Wenzler, M. Yarema, V.C. Wood, Low temperature hydrothermal synthesis of battery grade lithium iron phosphate, *RSC Adv.* 7 (2017) 17763–17767, <https://doi.org/10.1039/C7RA00463J>.
- [173] C. Julien, A. Mauger, A.K. Vijh, K. Zaghbi, *Lithium Batteries: Science and Technology*, Springer, 2016.
- [174] B. Ramasubramanian, S. Sundarajan, V. Chellappan, M.V. Reddy, S. Ramakrishna, K. Zaghbi, Recent development in carbon-LiFePO₄ cathodes for lithium-ion batteries: a mini review, *Batteries* 8 (2022), <https://doi.org/10.3390/batteries8100133>.
- [175] Z. Chen, Q. Zhang, Q. Liang, Carbon-coatings improve performance of Li-ion battery, *Nanomaterials* 12 (2022), <https://doi.org/10.3390/nano12111936>.
- [176] C. Neef, H.-P. Meyer, R. Klingeler, Morphology-controlled two-step synthesis and electrochemical studies on hierarchically structured LiCoPO₄, *Solid State Sci.* 48 (2015) 270–277, <https://doi.org/10.1016/j.solidstatesciences.2015.08.021>.
- [177] A. Vadivel Murugan, T. Muraliganth, A. Manthiram, One-pot microwave-hydrothermal synthesis and characterization of carbon-coated LiMPO₄ (M = Mn, Fe, and Co) cathodes, *J. Electrochem. Soc.* 156 (2008) A79, <https://doi.org/10.1149/1.3028304>.
- [178] S. Liu, P. Yan, H. Li, X. Zhang, W. Sun, One-step microwave synthesis of micro/nanoscale LiFePO₄/graphene cathode with high performance for lithium-ion batteries, *Front. Chem.* 8 (2020) 104, <https://doi.org/10.3389/fchem.2020.00104>.
- [179] G. Yang, S.-J. Park, Conventional and microwave hydrothermal synthesis and application of functional materials: a review, *Materials* 12 (2019), <https://doi.org/10.3390/ma12071177>.
- [180] A.V. Murugan, T. Muraliganth, A. Manthiram, Comparison of microwave assisted solvothermal and hydrothermal syntheses of LiFePO₄/C nanocomposite cathodes for lithium ion batteries, *J. Phys. Chem. C* 112 (2008) 14665–14671, <https://doi.org/10.1021/jp8053058>.
- [181] J.V. Laveda, B. Johnston, G.W. Paterson, P.J. Baker, M.G. Tucker, H.Y. Playford, K.M.Ø. Jensen, S.J.L. Billinge, S.A. Corr, Structure–property insights into nanostructured electrodes for Li-ion batteries from local structural and diffusional probes, *J. Mater. Chem. A* 6 (2018) 127–137, <https://doi.org/10.1039/C7TA04400C>.
- [182] R. Liu, J. Chen, Z. Li, Q. Ding, X. An, Y. Pan, Z. Zheng, M. Yang, D. Fu, Preparation of LiFePO₄/C cathode materials via a green synthesis route for lithium-ion battery applications, *Materials* 11 (2018) 2251.
- [183] A Vision for a Sustainable Battery Value Chain in 2030, G. B. Alliance, 2019. (https://www.globalbattery.org/media/publications/WEF_A_Vision_for_a_Sustainable_Battery_Value_Chain_in_2030_Report.pdf).
- [184] N.P.W. Pieczonka, Z. Liu, A. Huq, J.-H. Kim, Comparative study of LiMnPO₄/C cathodes synthesized by polyol and solid-state reaction methods for Li-ion batteries, *J. Power Sources* 230 (2013) 122–129, <https://doi.org/10.1016/j.jpowsour.2012.12.027>.
- [185] A.M. Nolan, Y. Liu, Y. Mo, Solid-state chemistries stable with high-energy cathodes for lithium-ion batteries, *ACS Energy Lett.* 4 (2019) 2444–2451, <https://doi.org/10.1021/acsenergylett.9b01703>.
- [186] R. Shahid, S. Murugavel, Synthesis and characterization of olivine phosphate cathode material with different particle sizes for rechargeable lithium-ion batteries, *Mater. Chem. Phys.* 140 (2013) 659–664, <https://doi.org/10.1016/j.matchemphys.2013.04.020>.
- [187] W.M. Dose, C. Peebles, J. Blauwkamp, A.N. Jansen, C. Liao, C.S. Johnson, Synthesis of high-density olivine LiFePO₄ from paleozoic siderite FeCO₃ and its electrochemical performance in lithium batteries, *APL Mater.* 10 (2022) 041113, <https://doi.org/10.1063/5.0084105>.
- [188] D. Choi, D. Wang, I.-T. Bae, J. Xiao, Z. Nie, W. Wang, V.V. Viswanathan, Y.J. Lee, J.-G. Zhang, G.L. Graff, Z. Yang, J. Liu, LiMnPO₄ nanoplate grown via solid-state reaction in molten hydrocarbon for Li-ion battery cathode, *Nano Lett.* 10 (2010) 2799–2805, <https://doi.org/10.1021/nl1007085>.
- [189] P. Sauriol, D. Li, L. Hadidi, H. Villazon, L. Jin, B. Yari, M. Gauthier, M. Dollé, P. Chartrand, W. Kasprzak, G. Liang, G.S. Patience, Fe³⁺ reduction during melt-synthesis of LiFePO₄, *Can. J. Chem. Eng.* 97 (2019) 2196–2210, <https://doi.org/10.1002/cjce.23522>.
- [190] K. Zaghbi, P. Charest, M. Dontigny, A. Guerfi, M. Lagacé, A. Mauger, M. Kopec, C. M. Julien, LiFePO₄: From molten ingot to nanoparticles with high-rate performance in Li-ion batteries, *J. Power Sources* 195 (2010) 8280–8288, <https://doi.org/10.1016/j.jpowsour.2010.07.010>.
- [191] K. Zaghbi, P. Charest, M. Dontigny, A. Guerfi, J. Trottier, A. Mauger, C.M. Julien, Electrochemical features of LiFePO₄ nanoparticles obtained by grinding ingot synthesized in the molten state, *ECS Trans.* 35 (2011) 83, <https://doi.org/10.1149/1.3654204>.
- [192] H. Villazon, P. Sauriol, S. Rousselot, M. Talebi-Esfandarani, T. Bibienne, M. Gauthier, G. Liang, M. Dollé, P. Chartrand, Melt-synthesis of LiFePO₄ over a metallic bath, *Can. J. Chem. Eng.* 97 (2019) 2287–2298, <https://doi.org/10.1002/cjce.23406>.
- [193] B. Daheron, D.D. MacNeil, Study of LiFePO₄ synthesized using a molten method with varying stoichiometries, *J. Solid State Electrochem.* 15 (2011) 1217–1225, <https://doi.org/10.1007/s10008-010-1191-9>.
- [194] E.B. Fredj, S. Rousselot, L. Danis, T. Bibienne, M. Gauthier, G. Liang, M. Dollé, Synthesis and characterization of LiFe_{1-x}Mn_xPO₄ (x = 0.25, 0.50, 0.75) lithium ion battery cathode synthesized via a melting process, *J. Energy Storage* 27 (2020) 101116, <https://doi.org/10.1016/j.est.2019.101116>.
- [195] G.S. Patience, J. Chaouki, M. Latifi, M. Dollé, P. Chartrand, W. Kasprzak, X. Sun, T.-K. Sham, G. Liang, P. Sauriol, Piloting melt synthesis and manufacturing processes to produce c-lifepo4: preface, *Can. J. Chem. Eng.* 97 (2019) 2189–2195, <https://doi.org/10.1002/cjce.23479>.
- [196] S. Huang, X. Huang, Y. Huang, X. He, H. Zhuo, S. Chen, Rational design of effective binders for LiFePO₄ cathodes, *Polymers* 13 (2021), <https://doi.org/10.3390/polym13183146>.
- [197] X. Zhang, X. Ge, Z. Shen, H. Ma, J. Wang, S. Wang, L. Liu, B. Liu, L. Liu, Y. Zhao, Green water-based binders for LiFePO₄/C cathodes in Li-ion batteries: a comparative study, *N. J. Chem.* 45 (2021) 9846–9855, <https://doi.org/10.1039/D1NJ01208H>.
- [198] J. Li, J. Fleetwood, W.B. Hawley, W. Kays, From materials to cell: state-of-the-art and prospective technologies for lithium-ion battery electrode processing, *Chem. Rev.* 122 (2022) 903–956, <https://doi.org/10.1021/acs.chemrev.1c00565>.
- [199] Y. Zhang, S. Lu, F. Lou, Z. Yu, Solvent-free lithium iron phosphate cathode fabrication with fibrillation of polytetrafluoroethylene, *Electrochim. Acta* 456 (2023) 142469, <https://doi.org/10.1016/j.electacta.2023.142469>.
- [200] J. Weng, L. Peng, Improving the electrochemical performance of LiFePO₄ cathode with novel water-soluble binders, *Mater. Chem. Phys.* 290 (2022) 126530, <https://doi.org/10.1016/j.matchemphys.2022.126530>.
- [201] N. Aguiló-Aguayo, D. Hubmann, F.U. Khan, S. Arzbacher, T. Bechtold, Water-based slurries for high-energy LiFePO₄ batteries using embroidered current collectors, *Sci. Rep.* 10 (2020) 5565, <https://doi.org/10.1038/s41598-020-62553-3>.
- [202] L. Qiu, Z. Shao, D. Wang, W. Wang, F. Wang, J. Wang, Enhanced electrochemical properties of LiFePO₄ (LFP) cathode using the carboxymethyl cellulose lithium (CMC-Li) as novel binder in lithium-ion battery, *Carbohydr. Polym.* 111 (2014) 588–591, <https://doi.org/10.1016/j.carbpol.2014.05.027>.
- [203] S. Gao, Y. Su, L. Bao, N. Li, L. Chen, Y. Zheng, J. Tian, J. Li, S. Chen, F. Wu, High-performance LiFePO₄/C electrode with polytetrafluoroethylene as an aqueous-based binder, *J. Power Sources* 298 (2015) 292–298, <https://doi.org/10.1016/j.jpowsour.2015.08.074>.
- [204] J. Huang, J. Wang, H. Zhong, L. Zhang, N-cyanoethyl polyethylenimine as a water-soluble binder for LiFePO₄ cathode in lithium-ion batteries, *J. Mater. Sci.* 53 (2018) 9690–9700, <https://doi.org/10.1007/s10853-018-2247-y>.
- [205] S.N. Eliseeva, M.A. Kamenskii, E.G. Tolstopyatova, V.V. Kondratiev, Effect of combined conductive polymer binder on the electrochemical performance of electrode materials for lithium-ion batteries, *Energies* 13 (2020), <https://doi.org/10.3390/en13092163>.
- [206] M. Guo, Z. Cao, Y. Liu, Y. Ni, X. Chen, M. Terrones, Y. Wang, Preparation of tough, binder-free, and self-supporting LiFePO₄ cathode by using mono-dispersed ultra-long single-walled carbon nanotubes for high-rate performance Li-ion battery, *Adv. Sci.* 10 (2023) 2207355, <https://doi.org/10.1002/advs.202207355>.
- [207] M. Akhlaq, U. Mushtaq, S. Naz, M. Uroos, Carboxymethyl cellulose-based materials as an alternative source for sustainable electrochemical devices: a review, *RSC Adv.* 13 (2023) 5723–5743, <https://doi.org/10.1039/D2RA08244F>.
- [208] R. Gordon, M. Kassab, N. Willenbacher, Effect of polymeric binders on dispersion of active particles in aqueous LiFePO₄-based cathode slurries as well as on mechanical and electrical properties of corresponding dry layers, *ACS Omega* 5 (2020) 11455–11465, <https://doi.org/10.1021/acsomega.0c00477>.
- [209] V.A. Nguyen, C. Kuss, Review—Conducting polymer-based binders for lithium-ion batteries and beyond, *J. Electrochem. Soc.* 167 (2020) 065501, <https://doi.org/10.1149/1945-7111/ab856b>.

- [210] W. Dou, M. Zheng, W. Zhang, T. Liu, F. Wang, G. Wan, Y. Liu, X. Tao, Review on the binders for sustainable high-energy-density lithium ion batteries: status, solutions, and prospects, *Adv. Funct. Mater.* 33 (2023) 2305161, <https://doi.org/10.1002/adfm.202305161>.
- [211] B. Karaman, L.D. Couto, M. Kinnaert, N. Job, The effect of particle size and the material loading to the performance and stability of the LFP batteries, *ECS Meet. Abstr.* MA2023-01 (2023) 597, <https://doi.org/10.1149/MA2023-012597mtgabs>.
- [212] Y. Abe, S. Kumagai, Effect of negative/positive capacity ratio on the rate and cycling performances of LiFePO₄/graphite lithium-ion batteries, *J. Energy Storage* 19 (2018) 96–102, <https://doi.org/10.1016/j.est.2018.07.012>.
- [213] H. Zhang, H. Zhao, M.A. Khan, W. Zou, J. Xu, L. Zhang, J. Zhang, Recent progress in advanced electrode materials, separators and electrolytes for lithium batteries, *J. Mater. Chem. A* 6 (2018) 20564–20620, <https://doi.org/10.1039/C8TA05336G>.
- [214] J. Xing, S. Bliznakov, L. Bonville, M. Oljaca, R. Maric, A review of nonaqueous electrolytes, binders, and separators for lithium-ion batteries, *Electrochem. Energy Rev.* 5 (2022) 14, <https://doi.org/10.1007/s41918-022-00131-z>.
- [215] X.-T. Wang, Z.-Y. Gu, W.-H. Li, X.-X. Zhao, J.-Z. Guo, K.-D. Du, X.-X. Luo, X.-L. Wu, Regulation of cathode-electrolyte interphase via electrolyte additives in lithium ion batteries, *Chem. Asian J.* 15 (2020) 2803–2814, <https://doi.org/10.1002/asia.202000522>.
- [216] M.D. Bouguern, A.K. Madikere Raghunatha Reddy, X. Li, S. Deng, H. Laryea, K. Zaghib, Engineering dry electrode manufacturing for sustainable lithium-ion batteries, *Batteries* 10 (2024), <https://doi.org/10.3390/batteries10010039>.
- [217] W. Li, Review—An unpredictable hazard in lithium-ion batteries from transition metal ions: dissolution from cathodes, deposition on anodes and elimination strategies, *J. Electrochem. Soc.* 167 (2020) 090514, <https://doi.org/10.1149/1945-7111/ab847f>.
- [218] A. Mauger, C.M. Julien, A. Paoletta, M. Armand, K. Zaghib, A comprehensive review of lithium salts and beyond for rechargeable batteries: progress and perspectives, *Mater. Sci. Eng. R. Rep.* 134 (2018) 1–21, <https://doi.org/10.1016/j.mser.2018.07.001>.
- [219] H. Zhou, K. Xiao, J. Li, Lithium difluoro(oxalate)borate and LiBF₄ blend salts electrolyte for LiNi_{0.5}Mn_{1.5}O₄ cathode material, *J. Power Sources* 302 (2016) 274–282, <https://doi.org/10.1016/j.jpowsour.2015.10.073>.
- [220] X. Zuo, C. Fan, J. Liu, X. Xiao, J. Wu, J. Nan, Lithium Tetrafluoroborate as an electrolyte additive to improve the high voltage performance of lithium-ion battery, *J. Electrochem. Soc.* 160 (2013) A1199, <https://doi.org/10.1149/2.066308jes>.
- [221] X. Chen, Y. Gong, X. Li, F. Zhan, X. Liu, J. Ma, Perspective on low-temperature electrolytes for LiFePO₄-based lithium-ion batteries, *Int. J. Min. Met. Mater.* 30 (1) (2023), <https://doi.org/10.1007/s12613-022-2541-1>.
- [222] Q. Wu, W. Lu, M. Miranda, T.K. Honaker-Schroeder, K.Y. Laksassai, D. Dees, Effects of lithium difluoro(oxalate)borate on the performance of Li-rich composite cathode in Li-ion battery, *Electrochem. Commun.* 24 (2012) 78–81, <https://doi.org/10.1016/j.elecom.2012.08.016>.
- [223] S. Choudhury, L.A. Archer, Lithium fluoride additives for stable cycling of lithium batteries at high current densities, *Adv. Electron. Mater.* 2 (2016) 1500246, <https://doi.org/10.1002/aelm.201500246>.
- [224] L. Li, H. Dai, C. Wang, Electrolyte additives: adding the stability of lithium metal anodes, *Nano Sel.* 2 (2021) 16–36, <https://doi.org/10.1002/nano.202000164>.
- [225] J. Liu, S. He, S. Liu, S. Wang, J. Zhang, Advanced electrolyte systems with additives for high-cell-voltage and high-energy-density lithium batteries, *J. Mater. Chem. A* 10 (2022) 22929–22954, <https://doi.org/10.1039/D2TA07696A>.
- [226] T. Jaumann, J. Balach, U. Langklotz, V. Sauchuk, M. Fritsch, A. Michaelis, V. Teltevskej, D. Mikhailova, S. Oswald, M. Klose, G. Stephani, R. Hauser, J. Eckert, L. Giebeler, Lifetime vs. rate capability: understanding the role of FEC and VC in high-energy Li-ion batteries with nano-silicon anodes, *Energy Storage Mater.* 6 (2017) 26–35, <https://doi.org/10.1016/j.ensm.2016.08.002>.
- [227] S. Choudhury, Rational design of nanostructured polymer electrolytes and solid-liquid interphases for lithium batteries, Springer, Cham, 2019 file:///C:/Users/edr/Downloads/978-3-030-28943-0.pdf.
- [228] F. Dai, M. Cai, Best practices in lithium battery cell preparation and evaluation, *Commun. Mater.* 3 (2022) 64, <https://doi.org/10.1038/s43246-022-00286-8>.
- [229] D. Coffin, J. Horowitz, The supply chain for electric vehicle batteries, *J. Int. Commer. Econ.* (2018), https://www.usitc.gov/publications/332/journals/the_supply_chain_for_electric_vehicle_batteries.pdf.
- [230] The composition of EV batteries: Cells? Modules? Packs? Let's understand properly!, Samsung SDI, n.d. (<https://www.samsungsdi.com/column/all/detail/54344.html>).
- [231] T. Chen, Y. Jin, H. Lv, A. Yang, M. Liu, B. Chen, Y. Xie, Q. Chen, Applications of lithium-ion batteries in grid-scale energy storage systems, *Trans. Tianjin Univ.* 26 (2020) 208–217, <https://doi.org/10.1007/s12209-020-00236-w>.
- [232] Y. Peng, H. Wang, C. Jin, W. Huang, F. Zhang, B. Li, W. Ju, C. Xu, X. Feng, M. Ouyang, Thermal runaway induced gas hazard for cell-to-pack (CTP) lithium-ion battery pack, *J. Energy Storage* 72 (2023) 108324, <https://doi.org/10.1016/j.est.2023.108324>.
- [233] S. Song, S. Munk-Nielsen, V. Knap, C. Uhrenfeldt, Performance evaluation of lithium-ion batteries (LiFePO₄ cathode) from novel perspectives using a new figure of merit, temperature distribution analysis, and cell package analysis, *J. Energy Storage* 44 (2021) 103413, <https://doi.org/10.1016/j.est.2021.103413>.
- [234] G. Wang, W. Gao, X. He, R. Peng, Y. Zhang, X. Dai, P. Ping, D. Kong, Numerical investigation on thermal runaway propagation and prevention in cell-to-chassis lithium-ion battery system, *Appl. Therm. Eng.* 236 (2024) 121528, <https://doi.org/10.1016/j.applthermaleng.2023.121528>.
- [235] C. Jin, Y. Sun, J. Yao, X. Peng, X. Lai, K. Shen, H. Wang, X. Rui, C. Xu, Y. Zheng, L. Lu, H. Wang, M. Ouyang, No thermal runaway propagation optimization design of battery arrangement for cell-to-chassis technology, *eTransportation* 14 (2022) 100199, <https://doi.org/10.1016/j.etrans.2022.100199>.
- [236] H. Walvekar, H. Beltran, S. Sripad, M. Pecht, Implications of the electric vehicle manufacturers' decision to mass adopt lithium-iron phosphate batteries, *IEEE Access* 10 (2022) 63834–63843, <https://doi.org/10.1109/ACCESS.2022.3182726>.
- [237] M. Fichtner, Recent research and progress in batteries for electric vehicles, *Batter. Supercaps* 5 (2022) e202100224, <https://doi.org/10.1002/batt.202100224>.
- [238] A Kind of Battery, Battery Modules, Battery Pack and Electric Vehicle, CN110518174A, 2020. (<https://patents.google.com/patent/CN110518174A/en?q=CN110518174A>).
- [239] J.T. Frith, M.J. Lacey, U. Ulissi, A non-academic perspective on the future of lithium-based batteries, *Nat. Commun.* 14 (2023) 420, <https://doi.org/10.1038/s41467-023-35933-2>.
- [240] BYD's Revolutionary Blade Battery: All You Need to Know, BYD, 2023. (<https://www.byd.com/eu/blog/BYDs-revolutionary-Blade-Battery-all-you-need-to-know.html>).
- [241] Method of pROducing In-situ Carbon Coated Lithium Iron Phosphate Cathode Material for Lithium-ion Batteries and the Product Thereof, WO2022144917A1, 2022. (<https://patents.google.com/patent/WO2022144917A1/en>).
- [242] L. Kraft, A. Hoeffling, T. Zünd, A. Kunz, M. Steinhardt, J. Tübke, A. Jossen, Implications of the heat generation of LMR-NCM on the thermal behavior of large-format lithium-ion batteries, *J. Electrochem. Soc.* 168 (2021) 053505, <https://doi.org/10.1149/1945-7111/ac0669>.
- [243] M. Kane, See inside of the Tesla Model 3's LFP prismatic battery pack, *Insideevs* (2021). (<https://insideevs.com/news/542064/tesla-model3-lfp-battery-pack/>).
- [244] H. Jin, P. Lienert, Tesla to use iron-based batteries in semi electric trucks and affordable electric car, *Reuters*, 2023. (<https://www.reuters.com/business/autos-transportation/tesla-use-iron-based-batteries-semi-electric-trucks-affordable-electric-car-2023-04-06/>).
- [245] BYD (n.d.). (<https://www.byd.com>).
- [246] Tesla Master Plan Part 3—Sustainable Energy for All of Earth, Tesla, 2023. (https://www.tesla.com/ns_videos/Tesla-Master-Plan-Part-3.pdf).
- [247] Semi the Future of Trucking, Tesla (2023). (https://www.tesla.com/en_ca/semi).
- [248] Continuing our Investment in Nevada, Tesla (2023). (https://www.tesla.com/en_ca/blog/continuing-our-investment-nevada).
- [249] LFP Batteries to Expand Powertrain Choice for Mustang Mach-e as Ford Increases Battery Production Capacity, Ford (2023). (<https://media.ford.com/content/fordmedia/feu/en/news/2023/02/16/lfp-batteries-to-expand-powertrain-choice-for-mustang-mach-e-as.html>).
- [250] 2023 F-150® Lightning, Ford (2023). (<https://www.ford.ca/trucks/f150/f150-lightning/models/f150-platinum/>).
- [251] List of Newly Released Technologies, Toyota, 2023. (https://global.toyota/pages/news/images/2023/06/13/0500/electrified_technologies_batteries_en.pdf).
- [252] S. Lee, Hyundai Highly Likely to Launch EV With CATL's LFP Batteries This Year, *Elec Inc*, 2023. (<https://www.theelec.net/news/articleView.html?idxno=4438>).
- [253] Kia launches, The Kia Ray EV, KIA, 2023. (<https://www.kia.com/kr/discover-kia/news/detail?code=CONT0000000000114306&page=1&con=all>).
- [254] J. White, I. Wissenbach, Mercedes CEO: Efficiency Is the "New Currency" in the EV Market, *Reuters* (2023). (<https://www.reuters.com/business/autos-transportation/mercedes-ceo-efficiency-is-new-currency-ev-market-2023-09-01/>).
- [255] New Mach-E LFP battery specs revealed, *macheforum* (2023). (<https://www.macheforum.com/site/threads/new-mach-e-lfp-battery-specs-revealed.26099/>).
- [256] S. Nordlund, Tesla Model Y RWD with BYD Blade Battery Has Improved Charging Speeds over Former CATL pack, *Drive Tesla Can.* (2023). (<https://drivetelsacan.ca/news/tesla-model-y-rwd-with-byd-blade-battery-has-improved-charging-speeds-over-former-catl-pack/>).
- [257] F. Lambert, Tesla is Working on New ~110 kWh Battery Pack for More than 400 Miles of Range, *Electrek*, 2020. (<https://electrek.co/2020/02/19/tesla-110-kwh-battery-pack-400-miles-range/>).
- [258] Passenger EV Battery Chemistries: LFP for the Massive, NCM for the Majority, (2022). (<https://www.adamasintel.com/lfp-for-the-massive-ncm-for-the-majority/>).
- [259] L.A.-W. Ellingsen, B. Singh, A.H. Strømman, The size and range effect: lifecycle greenhouse gas emissions of electric vehicles, *Environ. Res. Lett.* 11 (2016) 054010, <https://doi.org/10.1088/1748-9326/11/5/054010>.
- [260] Z. Gao, Z. Lin, T.J. LaClair, C. Liu, J.-M. Li, A.K. Birkly, J. Ward, Battery capacity and recharging needs for electric buses in city transit service, *Energy* 122 (2017) 588–600, <https://doi.org/10.1016/j.energy.2017.01.101>.
- [261] P. Liu, C. Liu, K. Yang, M. Zhang, F. Gao, B. Mao, H. Li, Q. Duan, Q. Wang, Thermal runaway and fire behaviors of lithium iron phosphate battery induced by over heating, *J. Energy Storage* 31 (2020) 101714, <https://doi.org/10.1016/j.est.2020.101714>.
- [262] M. Tajik, A. Makui, B.M. Tosarkani, Sustainable cathode material selection in lithium-ion batteries using a novel hybrid multi-criteria decision-making, *J. Energy Storage* 66 (2023) 107089, <https://doi.org/10.1016/j.est.2023.107089>.
- [263] Fire Hazard Analysis for Various Lithium Batteries, the Us Department of Transportation, Federal Aviation Administration, 2017. (<https://www.fire.tc.faa.gov/pdf/TC-16-17.pdf>).
- [264] P. Qin, Z. Jia, J. Wu, K. Jin, Q. Duan, L. Jiang, J. Sun, J. Ding, C. Shi, Q. Wang, The thermal runaway analysis on LiFePO₄ electrical energy storage packs with

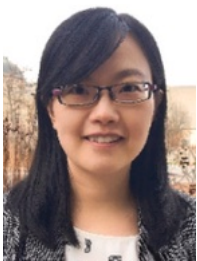
- different venting areas and void volumes, *Appl. Energy* 313 (2022) 118767, <https://doi.org/10.1016/j.apenergy.2022.118767>.
- [265] Accident Analysis of the Beijing Lithium Battery Explosion Which Killed Two Firefighters, CTIF International Association of Fire Services, 2021. (<https://ctif.org/news/accident-analysis-beijing-lithium-battery-explosion-which-killed-two-firefighters/>).
- [266] J. Jaguemont, F. Bardé, A critical review of lithium-ion battery safety testing and standards, *Appl. Therm. Eng.* 231 (2023) 121014, <https://doi.org/10.1016/j.applthermaleng.2023.121014>.
- [267] Lithium-Ion Battery Pack Prices Rise for First Time to an Average of \$151/kWh, (2022). (<https://about.bnef.com/blog/lithium-ion-battery-pack-prices-rise-for-first-time-to-an-average-of-151-kwh/>).
- [268] Electric Vehicle Battery Pack Costs in 2022 Are Nearly 90% Lower than in 2008, According to DOE Estimates, (2023). (<https://www.energy.gov/eere/vehicles/articles/fotw-1272-january-9-2023-electric-vehicle-battery-pack-costs-2022-are-nearly>).
- [269] D.R. Baker, 2022, (https://www.bloomberg.com/news/articles/2022-12-06/battery-prices-climb-for-first-time-just-as-more-evs-hit-market?in_source=embedded-checkout-banner), , EV Transit. Threat. Battery Prices. Rise First Time..
- [270] L. Mauler, F. Duffner, W.G. Zeier, J. Leker, Battery cost forecasting: a review of methods and results with an outlook to 2050, *Energy Environ. Sci.* 14 (2021) 4712–4739, <https://doi.org/10.1039/D1EE01530C>.
- [271] Price of Selected Battery Materials and Lithium-ion Batteries, 2015–2023, (2023). (<https://www.iea.org/data-and-statistics/charts/price-of-selected-battery-materials-and-lithium-ion-batteries-2015-2023>).
- [272] N. Muralidharan, E.C. Self, M. Dixit, Z. Du, R. Essehli, R. Amin, J. Nanda, I. Belharouak, Next-generation cobalt-free cathodes – a prospective solution to the battery industry’s cobalt problem, *Adv. Energy Mater.* 12 (2022) 2103050, <https://doi.org/10.1002/aenm.2021103050>.
- [273] Cobalt is the Most Expensive Material Used in Lithium-ion Battery Cathodes, (2022). (<https://www.energy.gov/eere/vehicles/articles/fotw-1228-march-7-2022-cobalt-most-expensive-material-used-lithium-ion#:~:text=Cobalt%20is%20an%20important%20ingredient,%249%20per%20pound%20in%202021>).
- [274] Battery Materials Market Set to Be Finely Balanced in 2023, (2023). (<https://www.fastmarkets.com/insights/battery-materials-market-set-to-be-finely-balanced>).
- [275] P. Desai, Explainer: Costs of Nickel and Cobalt Used in Electric Vehicle Batteries, Reuters, 2022. (<https://www.reuters.com/business/autos-transportation/costs-nickel-cobalt-used-electric-vehicle-batteries-2022-02-03/>).
- [276] N. Carey, P. Lienert, Insight: EV Battery Makers Race to Develop Cheaper Cell Materials, Skirting China, Reuters (2022). (<https://www.reuters.com/business/autos-transportation/ev-battery-makers-race-develop-cheaper-cell-materials-skirting-china-2022-11-15/>).
- [277] L. Mauler, X. Lou, F. Duffner, J. Leker, Technological innovation vs. tightening raw material markets: falling battery costs put at risk, *Energy Adv.* 1 (2022) 136–145, <https://doi.org/10.1039/D1YA00052G>.
- [278] X.-G. Yang, T. Liu, C.-Y. Wang, Thermally modulated lithium iron phosphate batteries for mass-market electric vehicles, *Nat. Energy* 6 (2021) 176–185, <https://doi.org/10.1038/s41560-020-00757-7>.
- [279] High Energy Density Technology Exceeding Limitations, CATL, 2023. (<https://www.catl.com/en/research/technology/>).
- [280] Volumetric Energy Density of Lithium-ion Batteries Increased by More than Eight Times Between 2008 and 2020, (2022). (<https://www.energy.gov/eere/vehicles/articles/fotw-1234-april-18-2022-volumetric-energy-density-lithium-ion-batteries>).
- [281] H. Zhang, L. Wang, H. Li, X. He, Criterion for identifying anodes for practically accessible high-energy-density lithium-ion batteries, *ACS Energy Lett.* 6 (2021) 3719–3724, <https://doi.org/10.1021/acsenenergylett.1c01713>.
- [282] J. Wu, X. Zhang, Z. Ju, L. Wang, Z. Hui, K. Mayilvahanan, K.J. Takeuchi, A. C. Marschilok, A.C. West, E.S. Takeuchi, G. Yu, From fundamental understanding to engineering design of high-performance thick electrodes for scalable energy-storage systems, *Adv. Mater.* 33 (2021) 2101275, <https://doi.org/10.1002/adma.202101275>.
- [283] Y. Lu, X. Rong, Y.-S. Hu, L. Chen, H. Li, Research and development of advanced battery materials in China, *Energy Storage Mater.* 23 (2019) 144–153, <https://doi.org/10.1016/j.ensm.2019.05.019>.
- [284] LuisD. Couto, M. Charkhgard, B. Karaman, N. Job, M. Kinnaert, Lithium-ion battery design optimization based on a dimensionless reduced-order electrochemical model, *Energy* 263 (2023) 125966, <https://doi.org/10.1016/j.energy.2022.125966>.
- [285] J.-S. Kim, D.-C. Lee, J.-J. Lee, C.-W. Kim, Optimization for maximum specific energy density of a lithium-ion battery using progressive quadratic response surface method and design of experiments, *Sci. Rep.* 10 (2020) 15586, <https://doi.org/10.1038/s41598-020-72442-4>.
- [286] S. Hasselwander, M. Meyer, I. Österle, Techno-economic analysis of different battery cell chemistries for the passenger vehicle market, *Batteries* 9 (2023), <https://doi.org/10.3390/batteries9070379>.
- [287] D. Bleakley, Tesla supplier CATL to produce M3P Batteries that will deliver big boost in range for EVs, Driven (2023). (<https://thedriven.io/2023/03/27/tesla-supplier-catl-to-produce-m3p-batteries-that-will-deliver-big-boost-in-range-for-evs/>).
- [288] N. Nitta, F. Wu, J.T. Lee, G. Yushin, Li-ion battery materials: present and future, *Mater. Today* 18 (2015) 252–264, <https://doi.org/10.1016/j.matod.2014.10.040>.
- [289] S. Ge, R.S. Longchamps, T. Liu, J. Liao, Y. Leng, C.-Y. Wang, High safety and cycling stability of ultrahigh energy lithium ion batteries, *Cell Rep. Phys. Sci.* 2 (2021) 100584, <https://doi.org/10.1016/j.xcrp.2021.100584>.
- [290] A. Masias, J. Marcicki, W.A. Paxton, Opportunities and challenges of lithium ion batteries in automotive applications, *ACS Energy Lett.* 6 (2021) 621–630, <https://doi.org/10.1021/acsenenergylett.0c02584>.
- [291] Z. Yang, H. Huang, F. Lin, Sustainable electric vehicle batteries for a sustainable world: perspectives on battery cathodes, environment, supply chain, manufacturing, life cycle, and policy, *Adv. Energy Mater.* 12 (2022) 2200383, <https://doi.org/10.1002/aenm.202200383>.
- [292] H. Hao, Z. Mu, S. Jiang, Z. Liu, F. Zhao, GHG emissions from the production of lithium-ion batteries for electric vehicles in China, *Sustainability* 9 (2017), <https://doi.org/10.3390/su9040504>.
- [293] M. Linder, T. Naucler, S. Nekovar, A. Pfeiffer, N. Vekic, the Race to Decarbonize Electric-vehicle Batteries, McKinsey Co, 2023. (<https://www.mckinsey.com/industries/automotive-and-assembly/our-insights/the-race-to-decarbonize-electric-vehicle-batteries/#/>).
- [294] Q. Chen, X. Lai, H. Gu, X. Tang, F. Gao, X. Han, Y. Zheng, Investigating carbon footprint and carbon reduction potential using a cradle-to-cradle LCA approach on lithium-ion batteries for electric vehicles in China, *J. Clean. Prod.* 369 (2022) 133342, <https://doi.org/10.1016/j.jclepro.2022.133342>.
- [295] IEA, Global CO2 Emissions by Sector, 2019, (2021). (<https://www.iea.org/data-and-statistics/charts/global-co2-emissions-by-sector-2019>).
- [296] IEA, Global CO2 Emissions from Transport by Sub-sector in the Net Zero Scenario, 2000–2030, (2023). (<https://www.iea.org/data-and-statistics/charts/global-co2-emissions-from-transport-by-sub-sector-in-the-net-zero-scenario-2000-2030-2>).
- [297] H. Hao, Y. Geng, J.E. Tate, F. Liu, K. Chen, X. Sun, Z. Liu, F. Zhao, Impact of transport electrification on critical metal sustainability with a focus on the heavy-duty segment, *Nat. Commun.* 10 (2019) 5398, <https://doi.org/10.1038/s41467-019-13400-1>.
- [298] X. Lai, Q. Chen, X. Tang, Y. Zhou, F. Gao, Y. Guo, R. Bhagat, Y. Zheng, Critical review of life cycle assessment of lithium-ion batteries for electric vehicles: a lifespan perspective, *eTransportation* 12 (2022) 100169, <https://doi.org/10.1016/j.etrans.2022.100169>.
- [299] C. Xu, B. Steubing, M. Hu, C. Harpprecht, M. van der Meide, A. Tukker, Future greenhouse gas emissions of automotive lithium-ion battery cell production, *Resour. Conserv. Recycl.* 187 (2022) 106606, <https://doi.org/10.1016/j.resconrec.2022.106606>.
- [300] J. Simaitis, S. Allen, C. Vagg, Are future recycling benefits misleading? Prospective life cycle assessment of lithium-ion batteries, *J. Ind. Ecol.* (2023), <https://doi.org/10.1111/jiec.13413>.
- [301] J. Fleischmann, P. Schaufuss, M. Linder, M. Hanicke, E. Horetsky, D. Ibrahim, S. Jautelat, L. Torscht, A. Rijt, Battery 2030: Resilient, Sustainable, and Circular, McKinsey Co, 2023. (<https://www.mckinsey.com/industries/automotive-and-assembly/our-insights/battery-2030-resilient-sustainable-and-circular>).



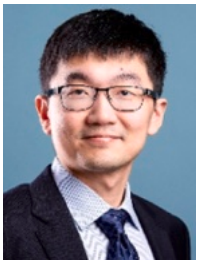
Dr. Atiyeh Nekahi received her Ph.D. in Materials Science and Engineering from Amirkabir University of Technology, where she worked on synthesizing and applying graphene hybrid nanomaterials. After that, she worked for several years in collaboration with universities and academic institutions on research and industrial projects. She is doing her second Ph.D. in Chemical and Materials Engineering, focusing on lithium-ion batteries.



Dr. Anil Kumar Madikere Raghunatha Reddy received his Ph.D. degree in Chemistry, his secure research experience of more than 12 years, He published 75 research papers in the reputed international peer reviewed Journals, published 6 books, 8 book chapters, published two Indian Patent, reviewer for Elsevier journals and he also the member of various committees for the inspection of new as well as old engineering institutions. He served as a Member, Board of Examiners, chemistry Composite Board & Board of Examiner and thesis evaluator. His research areas of interest Nano Science & Technology, Lithium-ion battery and beyond, Materials Science and photocatalysis.



Dr. Xia Li received her Ph.D. in Mechanical and Materials Engineering, Western University, Canada, she published more than 66 research papers in the reputed international peer reviewed Journals, her areas of interest on Safe and high energy all-solid-state batteries, Secondary Li-ion, Na-ion, Li-sulfur, and Na-sulfur batteries, Sustainable organic molecules-based batteries, Synchrotron radiation techniques for energy materials, Atomic and molecular layer thin film deposition techniques, Dr. Li's group is mainly focused on the development of advanced materials for clean energy, including well-controlled fabrication of nanomaterials for battery applications, materials structure and interface design, and mechanism investigation between structure and performance.



Dr. Sixu Deng is an Assistant Professor in the Department of Chemical and Materials Engineering at Concordia University. Before joining Concordia, Dr. Deng worked at McMaster University as an NSERC Postdoctoral Fellow in 2022. Dr. Deng received his B.Eng. and first Ph.D. at Beijing University of Technology in 2011 and 2018, respectively, and his second Ph. D. at Western University in 2022. Dr. Deng's research interests focus on the development of high-performance energy storage devices united with novel materials design and advanced characterizations. The research directions include solid-state batteries, ion-based batteries, supercapacitors, atomic/molecular layer deposition, synchrotron radiation, and in-situ/operando techniques.



Professor Karim Zaghib is a world-renowned scientist who specializes in electrochemistry, rechargeable batteries (lithium-ion and solid-state), carbon, energy transition and transportation electrification. He has been professor of chemical and materials engineering at Concordia University and director of the Collaboration Centers on Energy and its Transition, after a 28-year career at Hydro-Québec. As general director of research into the development of materials for lithium-ion batteries at Hydro-Québec, he helped make the company the first in the world to use lithium iron phosphate (LFP) in cathodes and to develop anodes in natural graphite and nanotitanate. These technologies are used by Tesla, Ford, Mercedes, BMW, CAT and BYD etc. Mr. Zaghib pioneered the first two-electrode photobattery and high-MWh capacity energy storage based on LFP/graphite, in a joint venture with Sony and Hydro-Québec. The team's latest advances, made in collaboration with universities, research centers and companies, pave the way for the next generation of electric vehicle batteries and energy storage solutions, an area in which the Quebec and Canada are well placed to play a leading role. He is co-author of 450 publications, 970 patents, 62 licenses. Its H index is 87 with 25896 citations.